TECHNISCHE UNIVERSITÄT MÜNCHEN
Fakultät für Elektrotechnik und Informationstechnik

Processing Approaches for Multistatic Large Along-Track Baseline SAR Constellations

Nida SAKAR

Vollständiger Abdruck der von der Fakultät für Elektrotechnik und Informationstechnik der Technischen Universität München zur Erlangung des akademischen Grades eines Doktorin der Ingenieurwissenschaften (Dr.-Ing.) genehmigten Dissertation.

Vorsitzender: Prof. Dr.-Ing. Eckehard Steinbach
Prüfer der Dissertation:
1. Prof. Dr.-Ing. Thomas Eibert
2. Prof. Dr.-Ing. Gerhard Krieger

Die Dissertation wurde am 14.06.2021 bei der Technischen Universität München eingereicht und durch die Fakultät für Elektrotechnik und Informationstechnik am 13.04.2022 angenommen.

Abstract

Nida SAKAR

Processing Approaches for Multistatic Large Along-Track Baseline SAR Constellations

Spaceborne Synthetic Aperture Radar (SAR) systems have become an irreplaceable source of information for the scientific community over the past three decades due to its wide range of practical applications. A thorough understanding of Earth's dynamic processes requires systematic high-resolution imaging with short temporal baselines. Conventional SAR systems fail to comply with the requirements on the resolution and temporal baseline simultaneously, and can only offer one at the expense of the other. Therefore, next-generation spaceborne SAR systems aim at fulfilling this demanding requirement via advanced imaging and signal processing techniques.

Multi-aperture SAR systems make use of several transmit and receive channels for boosting the performance of the system. Such a concept with one transmit and multiple receive units can be utilized for high-resolution wide-swath (HRWS) imaging with digital beamforming in azimuth. Compared to single-platform systems with multiple channels where the deployable maximum antenna length poses a limitation, multistatic SAR systems offer flexibility, cost-efficiency and sustainability. This work focuses on the investigation of advanced processing methods for multistatic SAR constellations with large along-track baselines in order to pave the way for the realization of highly flexible SAR concepts for HRWS imaging.

This thesis evaluates multi-aperture reconstruction algorithms with particular emphasis on their suitability and shortcomings for multistatic SAR constellations with large along-track baselines. It introduces an efficient methodology to assess the performance of reconstruction algorithms without going through the processing steps. A comprehensive analysis on the important aspects of an accurate reconstruction strategy leads to the development of several novel reconstruction approaches suitable for along-track multi-aperture systems ranging from single-platform (multichannel) to distributed constellations with large along-track baselines. These approaches are capable of accommodating both range-time and range-frequency dependent terms in the Doppler domain as well as in the time domain. Finally, orbit control requirements for multistatic SAR systems and the influence of the available technology on the accurate reconstruction are investigated, and then a realistic system concept is identified.

Contents

List of Figures

List of Tables

List of Abbreviations

1D	One-dimensional
2D	Two-dimensional
AASR	Azimuth Ambiguity-to-Signal Ratio
AC	Azimuth Compression
A/D	Analog-to-Digital (Converter)
ASI	Italian Space Agency
CSA	Canadian Space Agency
DBF	Digital BeamForming
DLR	Deutches Zentrum für Luft- und Raumfahrt (German Aerospace Center)
ERS-1/2	European Remote Sensing Satellite 1/2
ESA	European Space Agency
FFT	Fast Fourier Transform
FM	Frequency Modulation
GSO	Geosynchronous Orbits
JAXA	Japanese Aerospace Exploration Agency
JPL	NASA's Jet Propulsion Laboratory
HRWS	High Resolution Wide Swath
IFFT	Inverse Fast Fourier Transform
ISLR	Integrated Sidelobe Ratio
IR	Impulse Response
IRW	Impulse Response Width
ISRO	Indian Space Research Organisation
LEO	Low Earth Orbit
LOS	Line Of Sight
MMSE	Minimum Mean Squared Error
ML	Maximum-Likelihood
MIMO	Multiple Input Multiple Output
MVDR	Minimum Variance Distortionless Response (beamformer)
NASA	National Aeronautics and Space Administration
PRF	Pulse Repetition Frequency
PRI	Pulse Repetition Interval
PSLR	Peak-to-Sidelobe Ratio
PTAR	Peak-to-Ambiguity Ratio
RADAR	Radio Detection and Ranging
RC	Range Compression
RCMC	Range Cell Migration Correction
Rx	Receiver
SAR	Synthetic Aperture Radar
SCORE	ScanOn-Receive
SIMO	Single Input Multiple Output

SIR-A/B/C	Shuttle Imaging Radar missions A/B/C
SISO	Single Input Single Output
SLAR	Side-looking Aperture Radar
SNR	Signal-to-Noise Ratio
SRTM	Shuttle Radar Topography Mission
Tx	Transmitter
Tx/Rx	Transmit/Receive Module
TECU	Total Electron Content Units
TOPS	Terrain Observation by Progressive Scans
VTEC	Vertical Total Electron Content

List of Symbols

Lower case letters

b_i	m	along-track baseline
b_{xt}	m	across-track baseline
c_i		i-th coefficient of the quadratic range history deviation polynomial
d		range-compressed data
f_0	Hz	radar carrier frequency
f_{a}	Hz	azimuth frequency
$f_{a,i}$	Hz	instantaneous frequency of SAR survey
f_{DC}	Hz	Doppler centroid
f_D	Hz	instantaneous Doppler frequency
f_{r}	Hz	range frequency
h	m	antenna height above ground
$\mathbf{h}_{\mathrm{multi}}$		impulse response function of multistatic SAR constellation
k_{a}		resolution factor due to spectral weighting in azimuth
k_{r}		resolution factor due to spectral weighting in range
m		PRI variation margin
r_0	m	slant range of point target
$r(t_{\mathrm{a}}; r_0)$	m	range history of the target
$r_i(t_{\mathrm{a}}; r_0)$	m	bistatic range history of the receiver i
$t_{rcm}(f_{\mathrm{a}})$		range cell migration
t_{a}	s	slow time (azimuth time)
t_{r}	s	fast time (range time)
s_{Rx}		reflected echo of a single target
s_{Tx}		transmitted radar signal
v_g	m/s	speed of the radar beam on the ground
v_e	m/s	effective velocity
v_s	m/s	platform velocity
v_{Tx}	m/s	velocity of the transmit platform
v_{Rx}	m/s	velocity of the transmit platform
x	m	azimuth spatial axis
w_{a}		azimuth envelope
w_{ML}		reconstruction filter weights of Maximum Likelihood (ML) method
w_{MMSE}		reconstruction filter weights of Minimum Mean-squared Error (MMSE) method
w_{MVDR}		reconstruction filter weights of Minimum Variance Distortionless Response (MVDR)

		method
w_{r}		range envelope
w_{Tx}		envelope of the transmitted chirp
z	m	zenith path delay

Capital letters

B_{a}	Hz	Doppler bandwidth
B_{r}	Hz	bandwidth of the transmitted signal
C_i		i-th coefficient of the residual phase term
H	m	reference height
$H(f_{\mathrm{r}}, f_{\mathrm{a}}; r_0)$		SAR transfer function
$H_i(f_{\mathrm{r}}, f_{\mathrm{a}})$		SAR transfer function for receiver i
N_{rx}		number of the receive satellites in azimuth
K	Hz/s	chirp rate of transmitted signal
K_{a}	Hz/s	azimuth chirp rate
L_{a}	m	length of the radar antenna
L_{sa}	m	length of the synthetic aperture
$\boldsymbol{P(f_a)}$		matrix containing the reconstruction filter functions $P_{ij}(f_a)$
R_n		noise covariance matrix
R		covariance matrix of the signal and additive noise
$S_j(f_{\mathrm{r}}, f_{\mathrm{a}})$		reconstructed signal in the j-th sub-band
$S_{\mathrm{Tx}}(f_{\mathrm{r}})$		Fourier transform of the transmitted signal
T	s	integration time
W_{g}	m	swath width on the ground
$W(f_{\mathrm{r}}, f_{\mathrm{a}})$		amplitude factor in wavenumber domain

Greek letters

α		oversampling factor
β_{src}		secondary range compression term
β_{res}		resolution index
δh	m	maximum topographic gradient within the transmit footprint
δr	m	range resolution
δx	m	azimuth resolution
$\delta t_{\mathrm{atrack}}$	s	requirement on the control of the along-track position of the spacecraft
$\delta\Delta\Phi$	rad	error in the estimation of the residual phase term
$\Delta f_{DC,i}$	Hz	Doppler centroid deviation
$\Delta r_{atm}(t_a, r_0)$	m	total atmospheric delay
Δr_{ion}	m	ionospheric delay
Δr_{trop}	m	tropospheric delay
$\Delta r_i(t_{\mathrm{a}}, b_i; r_0)$	m	range history deviation of receiver i with

		respect to the reference receiver
Δt_{a}	s	azimuth time shift due to the along-track separation between transmitter and receiver
Δt_i	s	zero-Doppler time difference of the range histories
$\Delta\Phi_i$	rad	residual phase term caused by the geometrical difference
θ_{a}	rad	aperture angle
λ	m	carrier wavelength
τ	s	duration of the transmitted pulse
$\epsilon(f_{\mathrm{r}}, f_{\mathrm{a}})$		reconstruction error
ϵ_ϕ	rad	maximum phase error caused by the model mismatch
$\phi_{AC}(t_{\mathrm{a}}; r_0)$	rad	phase azimuth modulation term
$\phi(f_{\mathrm{r}}, f_{\mathrm{a}}; r_0)$	rad	phase of the SAR transfer function
ϕ_{AC}	rad	the phase azimuth modulation term
Φ_{ref}	rad	wavenumber phase of the reference transfer function
v		arbitrary complex constant
η_{ss}		system scaling
ζ		design factor (<1)

To my son, Levin Simón.

Chapter 1

Introduction

1.1 Synthetic Aperture Radar Remote Sensing

The concept of remote sensing refers to acquiring information about an object without being in its vicinity. Nowadays, the term is used mostly to define Earth observation with a sensor mounted either on a spacecraft or on an airplane. Remote sensing sensors are typically classified as a) active, providing the source of transmitted energy and b) passive, recording scattered signals of an external source. The remote sensing instrument considered in this thesis consists of both active radar (RAdio Detection And Ranging) sensors and passive radar receivers.

Radar measures the distance between the target and the sensor by measuring the time delay between the transmitted microwave or radio frequency signal and its echo scattered from the objects in its line of sight (LOS). The first radar called "Telemobiloscope" was invented by the German physicist, Christian Hülsmeyer, in 1904 to prevent ship collisions in fog (Hülsmeyer, 1905). It was mainly used for object detection, not being capable of measuring the distance to the object. The invention of radar technology is essentially based on the theoretical work of James C. Maxwell on electromagnetic fields (Maxwell, 1865) and on the experimental work of Heinrich H. Hertz on proving the existence of electromagnetic waves and their propagation properties through space and different types of materials in the late 19th century (Skolnik, 1980). Similar to many other technologies, the radar technique caught worldwide interest during World War II to be utilized for military applications and experienced a rapid development. After the war, the aviation industry benefited from these recent developments in radar.

Synthetic Aperture Radar (SAR) is a technique invented by Carl Wiley while working at Goodyear Aerospace in 1951 (Wiley, 1965; Wiley, 1985). The technique exploits the motion of the radar platform to improve the azimuth resolution of a side-looking aperture radar (SLAR) by transmitting pulses over a target region and coherently combining the received echoes. In the following two decades, comprehensive research activities made SAR an established technique (Cutrona et al., 1961; Sherwin, Ruina, and Rawcliffe, 1962; Brown, 1967), opening the door for the golden age of civilian and military SAR missions. In 1978, NASA/JPL launched the first civilian spaceborne SAR sensor for an experimental mission operated at L-band, the Seasat, whose objective was to collect information about oceans (*NASA Jet Propulsion Laboratory (August, 2020), "Seasat" [Online]* n.d.). Despite its short lifetime in orbit, it is considered to be the pioneer of Earth observation missions. After the success of the Seasat mission, a great number of SAR satellites have been launched for Earth observation by the European Space Agency (ESA), the Japanese Aerospace Exploration Agency (JAXA), the Canadian Space Agency (CSA), NASA's Jet Propulsion Laboratory (JPL), the Indian Space Research Organisation (ISRO) and the German Aerospace Center (DLR). Some early examples of the missions are NASA's Space

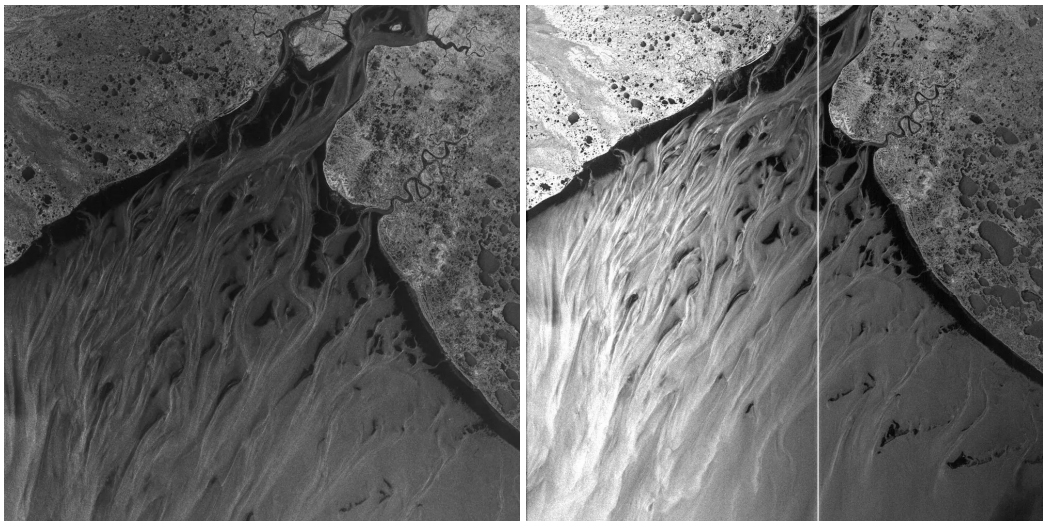

FIGURE 1.1: Seasat images with a geometric resolution of 25 m over Kuskokwim Delta, USA processed 26 years apart (*Seasat data 1978 (NASA). Processed by ASF DAAC 2013. Retrieved from ASF DAAC 11 July 2020.[Online]* n.d.). Left: processed in 1978, right: processed in 2013. The constant data processing and storage development in the last three decades allows for usage of more Seasat data for quantitative analysis. Note that the white line in the right is the calibration pulse.

Shuttle Imaging Radar (SIR) program with SIR-A (*NASA Jet Propulsion Laboratory (August, 2020) "Shuttle Imaging Radar-A" [Online]* n.d.) in 1981 and SIR-B (*NASA Jet Propulsion Laboratory (August, 2020) "Shuttle Imaging Radar-B" [Online]* n.d.) in 1984, ESA's ERS-1 (*ESA Earth Observation Portal, (August, 2020) "European Remote Sensing Satellite" [Online]* n.d.) (1991), the Soviet system ALMAZ-1 (*ESA Earth Observation Portal, (August, 2020) "Almaz-1 Mission" [Online]* n.d.) (1991) and JAXA's JERS-1 (*JAXA, (August, 2020), "Japanese Earth Resources Satellite "FUYO-1" (JERS-1)" [Online]* n.d.) (1992). Another historically significant mission is the first fully polarimetric multifrequency spaceborne SAR, SIR-C/X-SAR, launched in 1994 (Freeman et al., 2019) which was the result of a cooperation between NASA, the German Aerospace Center (DLR) and the Italian Space Agency (ASI). This mission opened a new door to interferometric applications and paved the way for delivering the first world-wide Digital Elevation Model (DEM) in 2000 together with the Shuttle Radar Topography Mission (SRTM) of NASA (*NASA Jet Propulsion Laboratory, (August, 2020) "Shuttle Radar Topography Mission" [Online]* n.d.).

Today, 117 years after the invention of the radar, SAR is a very popular remote sensing technique due to its fine resolution and its established applications including SAR interferometry (Rosen et al., 2000; Ferretti, Prati, and Rocca, 2001), polarimetric interferometry (Papathanassiou and Cloude, 2001), and SAR tomography (Reigber and Moreira, 2000), that provide information for disaster management, security, land and sea traffic observation, wide area surveillance, and environmental monitoring. Additionally, SAR owes its popularity to the fact that the electromagnetic waves of the radar are affected by neither weather nor light conditions. As shown in Figure 1.1, the advances in processing methods and data storage capacity only increase the appeal of SAR, leading a new path to the new spaceborne missions.

FIGURE 1.2: The oil slick in Mexico was imaged with a series of TerraSAR-X images acquired on July 9, 2010 (*DLR Portal, TanDEM-X - (August, 2020) "Oil slick in the Gulf of Mexico" [Online]* n.d.). An explosion caused a drilling rig to sink and disable the shut-off valves.

1.2 State-of-the-Art Spaceborne SAR Missions

The increasing interest for SAR technology in the last three decades has lead to numerous currently operational and planned spaceborne SAR missions, some of which are listed in Table 1.1. These missions are operated by national space agencies, such as ASI (Italy), CONAE (Argentina), DLR (Germany), European Space Agency (ESA), ISRO (India), JAXA (Japan), KARI (Korea), NASA (United States), NSOAS (China) and Roscosmos (Russia). Figures 1.2-1.5 illustrate TerraSAR-X high-resolution images demonstrating a few SAR applications. The images show oil spill detection in Mexico (environment monitoring), damage caused by tsunami in Sendai (disaster monitoring), digital elevation model over Las Vegas (topography), and traffic monitoring in Italy (Moving Target Indication).

Due to its high cost, SAR missions were realized mostly by national space agencies until recently. Today, the start-up companies such as Iceye, Capella Space and Umbra Lab have taken their place in the SAR imaging market (*Iceye from 11 July 2020 [Online]* n.d.; *Capella Space from 11 July 2020 [Online]* n.d.; *Umbra Lab from 11 July 2020 [Online]* n.d.). The main goal of these companies is to provide high-resolution SAR data with a constellation of small and less expensive satellites. Iceye has already launched five X-band satellites since 2019 and provides commercial high-resolution SAR images in Stripmap and Spotlight modes. Capella Space launched its first satellite in late 2020 and it is already operational. The future of the SAR imaging market will reveal itself based on the success of these start-ups and the demand for their products.

A typical SAR sensor employs a phased array antenna, which offers the possibility of beamsteering and beamforming, and hence, enables advanced imaging modes such as Spotlight, ScanSAR and TOPS (Carrara, Goodman, and Majewski,

TABLE 1.1: Overview of current and future SAR missions.

Mission	Agency	Launch	Band	Mode	Resolution	Swath Width
TerraSAR-X	DLR	2007	X	Stripmap Spotlight ScanSAR	3 m 1 m/2 m 16 m	30 km 5 km/10 km 100 km
Cosmo-Skymed	ASI	2007-2010	X	Stripmap Spotlight ScanSAR	3 m 1 m 16 m/30 m	40 km 10 km 100 km/200 km
Radarsat-2	CSA	2007	C	Stripmap Spotlight ScanSAR	9 m 3 m 28 m/50 m	50 km 20 km 100 km/300 km
Kompsat-5	KARI	2013	X	Stripmap Spotlight ScanSAR	3 m 1 m 20 m	30 km 5 km 100 km
Sentinel-1	ESA	2014	C	Stripmap ScanSAR	5 m 20 m	80 km 250 km
ALOS-2	JAXA	2014	L	Stripmap Spotlight ScanSAR	3 m 1 m 100 km	50 km 25 km 350 km
Cosmo-Skymed 2nd Gen	ASI	Approved	X	Stripmap Spotlight ScanSAR	3 m 0.8 m 4 m/6 m	40 km 10 km 100 km/200 km
NiSAR	NASA/ISRO	Approved	L,S	Stripmap	7 m	240 km
HRWS DBF SAR	DLR	Proposed	X	Stripmap Spotlight ScanSAR	3 m 0.8 m 4 m/6 m	40 km 10 km 100 km/200 km
WSAR	NSOAS	Proposed	X	Stripmap Spotlight ScanSAR	5 m 1 m 10 m	80 km 40 km 150 km

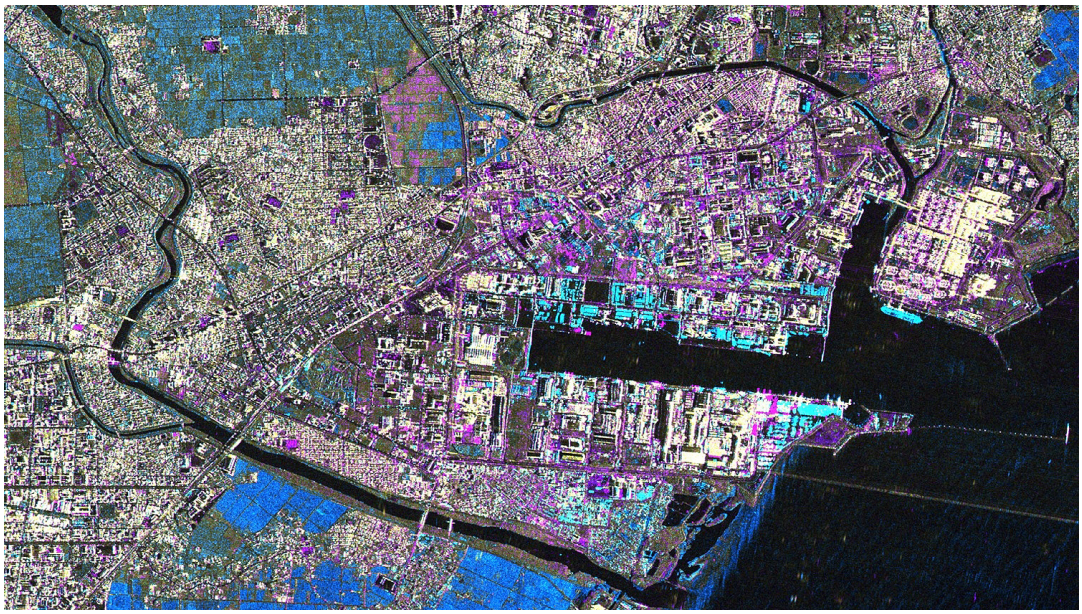

FIGURE 1.3: The TerraSAR-X image acquired on March 12, 2011 shows the impact of the tsunami on the port of Sendai, Japan (*DLR Portal, TanDEM-X - (August, 2020)"The port of Sendai after the tsunami" [Online]* n.d.). The blue colour indicates the flooded areas and the magenta colour highlights the damaged areas in the form of boulders.

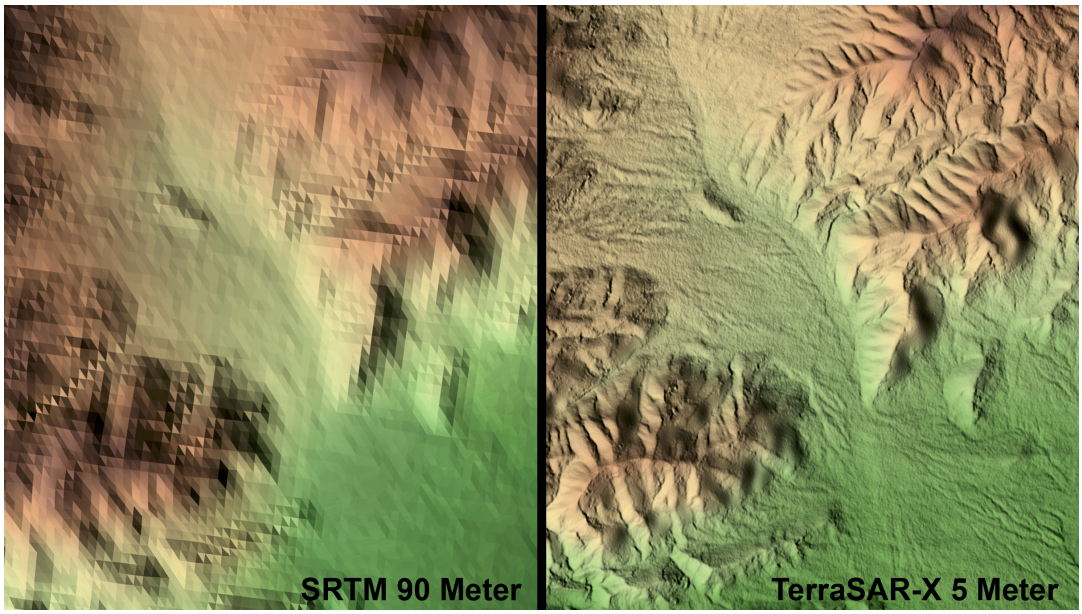

FIGURE 1.4: Comparison of the elevation model acquired by (left) the Shuttle Radar Topography Mission (SRTM) and (right) TerraSAR-X on a section of Las Vegas, USA (*DLR Portal, TanDEM-X - (August, 2020) "Las Vegas, USA – First TerraSAR-X Digital Elevation Model" [Online]* n.d.). The comparison between both missions with a great resolution difference stresses the importance of high-resolution imaging to fully understand the complex dynamic changes of the Earth.

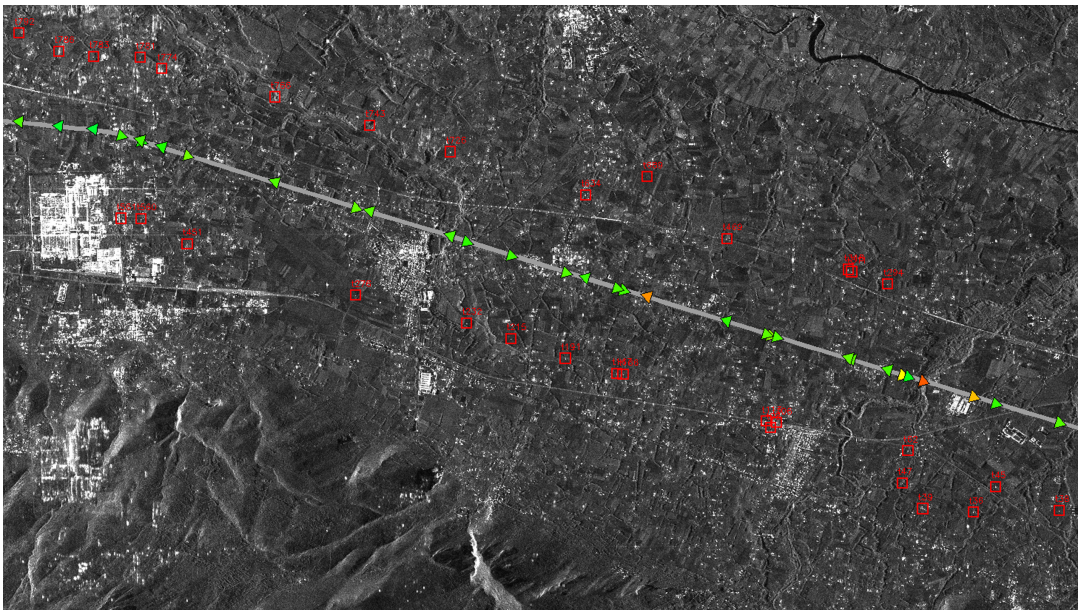

FIGURE 1.5: Traffic monitoring in Italy with Moving Target Indication (MTI) technique which makes use of Doppler differences between moving and stationary targets (*DLR Portal, TanDEM-X - (August, 2020)" Italy – Automatic speed control of moving objects using the Doppler effect " [Online]* n.d.). MTI is also used to measure the velocities of ocean surface currents and moving vehicles.

1995; Moore, Claassen, and Lin, 1981; De Zan and Monti Guarnieri, 2006). In conventional SAR systems, the beamsteering and beamforming are done by applying an analog real-time weight on transmit and receive and, only the weighted raw data are stored. As shown in Table 1.1, all sensors in orbit provide either high-resolution images with a narrow swath (low temporal resolution) or low-resolution images with a large swath (high temporal resolution). This compromise between resolution and swath describes the inherent limitation of single-aperture SAR systems (Curlander and McDonough, 1991). As an example to this limitation, the TerraSAR-X and TanDEM-X satellites operating in their standard mode (stripmap with 30 km swath width and 3 m resolution) provide global mapping in a year. More recent missions try to overcome this limitation by flying a constellation to provide high-resolution imaging with a short revisit time, such as Cosmo-Skymed (4 satellites) without pushing for an advanced technological improvement since the increase in the number of satellites linearly scales the capabilities of a single satellite mission (*ASI Cosmo-Skymed from 11 July 2020 [Online]* n.d.). However, this approach also linearly scales the cost of the mission. As some SAR applications require high-resolution imaging of the Earth with high temporal frequency (i.e., short revisit time over the same area) to understand the global dynamic changes (Moreira et al., 2013), new SAR concepts (Griffiths and Mancini, 1991; Currie and Brown, 1992; Callaghan and Longstaff, 1999; Goodman, Rajakrishna, and Stiles, 1999) and associated processing techniques (Krieger, Gebert, and Moreira, 2004b; Gebert, Krieger, and Moreira, 2009; Cerutti-Maori et al., 2014a; Cerutti-Maori et al., 2014b; Sikaneta, Gierull, and Cerutti-Maori, 2014; Li et al., 2005), all essentially based on a multi-aperture concept, are the present-day center of interest.

1.3 Motivation, Scope and Structure of the Thesis

As noted in the previous section, despite being a well-proven powerful technique, conventional SAR systems with a single transmit/receive unit fall behind current needs of the remote sensing society willing to study the Earth system. A rather direct and expensive way to overcome the inherent limitation between the resolution and the swath width is to launch a constellation composed of several single-aperture SARs, an approach adopted in the past decade for Cosmo-Skymed and Sentinel-1 missions. However, an innovative way to linearly scale the conventional SAR performance is through new concepts and processing strategies enabling multi-aperture reception. The additional receive units can be obtained by splitting the transmit antenna in azimuth and/or in elevation when receiving, i.e., multi-channel systems, or by deploying multiple receivers on different platforms, i.e., multistatic constellations. Starting from early 2000, the processing methods for multi-aperture data were addressed in (Aguttes, 2005; Younis, Fischer, and Wiesbeck, 2003) for along-track configurations, (Suess and Wiesbeck, 2002a; Kare, 2001; Suess, Grafmueller, and Zahn, 2001; Wiesbeck, 2001; Heer et al., 2003; Fischer et al., 2006) for across-track configurations and in (Goodman, Rajakrishna, and Stiles, 1999; Stiles, Goodman, and SiChung Lin, 2000; Goodman et al., 2002) for a combination of along-track/across-track configurations. All these methods consider single-platform realizations. Multistatic SAR constellations, on the other hand, offer the potential of flexible observation geometries and enhanced performance with reduced sensor complexity and costs (Krieger et al., 2003; Krieger et al., 2018).

A processing approach for single-platform high-resolution wide-swath (HRWS) mode SAR in azimuth is proposed in (Krieger, Gebert, and Moreira, 2004a; Krieger, Gebert, and Moreira, 2004b) and extensively analysed in (Gebert, Krieger, and Moreira, 2005a; Gebert, Krieger, and Moreira, 2006; Gebert, Krieger, and Moreira, 2005b; Gebert, Krieger, and Moreira, 2006; Gebert, 2009). However, the deployable antenna size of a spaceborne SAR poses a limitation for single platform configurations (Younis, 2004). The thesis in hand considers multistatic SAR constellations in azimuth with one active sensor and multiple low-cost passive sensors, naturally circumventing the antenna size problem. A multistatic SAR system enabling high-resolution imaging may be operated with a pulse repetition frequency (PRF) under the Nyquist rate of the single platform, allowing the imaging of large swaths. In such a system, since the echoes of the individual receivers appear aliased, the recovery of the unambiguous Doppler spectrum via azimuth reconstruction is required before SAR image formation occurs (Krieger, Gebert, and Moreira, 2004b). Numerous methods for multi-channel/multistatic azimuth reconstruction exist in the literature (Krieger, Gebert, and Moreira, 2004b; Gebert, Krieger, and Moreira, 2009; Cerutti-Maori et al., 2014a; Sikaneta, Gierull, and Cerutti-Maori, 2014; Li et al., 2005; Cerutti-Maori et al., 2014b). Depending on the optimization methodology, the shape of the reconstruction filter weights varies. The approaches in (Cerutti-Maori et al., 2014a; Sikaneta, Gierull, and Cerutti-Maori, 2014; Li et al., 2005), however, essentially resemble to the method in (Krieger, Gebert, and Moreira, 2004b), which is based on the generalized sampling theory (Papoulis, 1977). All other methods in the literature aim at mitigating inversion instabilities of the approach proposed in (Krieger, Gebert, and Moreira, 2004b) arising from noise scaling and sub-optimal sampling schemes. The validity of this family of algorithms is limited to the system concepts that meet the following assumptions: a) azimuth invariance, b) common scene spectrum observed by all receivers, acceptable whenever the shift in the Doppler centroid of the channels remains a fraction of the total azimuth bandwidth of the acquisition, and c) the

range histories observed by the different channels are roughly the same. As a direct consequence, the applicability of the existing approaches is confined to small along-track separations of the phase centers, which practically limits their appropriateness to single-platform multi-channel systems. In distributed systems with along-track baselines of a few km, the changes in the range history introduce strong polychromatic (coupling between Doppler and range frequencies) variations which are ignored in the available literature. In particular, a residual range-variant polychromatic quadratic component propagates into the reconstruction algorithm causing defocusing and a significant raise of ambiguities.

The present work focuses on the development of efficient and robust processing algorithms for multistatic SAR constellations, which overcome the aforementioned limitations and are thus valid over large swaths, for large along-track baselines and very high resolution. The geometrical aspects of the azimuth reconstruction that are explicitly incorporated in the presented solution are: i) the range history deviation between receiving channels is modeled as a quadratic polynomial, ii) the range-variance and the polychromatic character of the reconstruction filters are accommodated in a very accurate manner, including the fit of the reconstruction filters to the range cell migration of the data.

This dissertation is organized as follows. Chapter 2 summarizes the basic principles of Synthetic Aperture Radar theory, the most common SAR processing approaches and constraints of conventional SAR systems, which leads to the introduction of bistatic and multistatic SAR concepts discussed in the second part of the chapter. Chapter 3 starts with introducing multistatic SAR operated in HRWS mode and existing reconstruction algorithms in detail. An exact multistatic SAR signal model is derived and, consequently, an analytical model to assess the validity of the state-of-the-art reconstruction algorithms without having to go through the reconstruction is presented. An error analysis on the algorithms available in literature is then followed by a detailed section on the identification of all important aspects for an exact multistatic reconstruction algorithm for HRWS imaging. Due to the complex imaging geometry, multistatic SAR reconstruction poses a challenge that requires to solve an analytical system addressing many aspects, such as exact modelling, orbit control, and topography. Chapter 3 lays the foundation for a profound understanding of accurate reconstruction approaches. Next, Chapter 4 presents the theory and principles of polychromatic azimuth reconstruction algorithms in both Doppler domain and time domain (with constant and varying PRI). In Chapter 5, orbit control requirements for high-resolution SAR systems are analysed and the impact of a varying pulse repetition interval (PRI) on the system requirements in terms of oversampling is investigated. Considering all the information provided in the previous chapters in terms of reconstruction and system constraints, the focus is then turned to identifying realistic system parameters for a multistatic SAR constellation in HRWS mode. Chapter 6 summarizes the objectives and achievements of this thesis and, provides an outlook for further research.

1.4 Main Contributions

The main contributions of this work include (see Appendix A.1 for the list of the publications):

- Novel interpretation and analytical modelling of multistatic SAR data with constant and varying PRI configurations, allowing for very accurate phase deviation compensation with azimuth reconstruction.

- Derivation of an analytical model to assess the performance of any reconstruction strategy with different filter weights without going through the reconstruction steps.
- Identification of all important aspects of accurate azimuth reconstruction for multistatic SAR data in HRWS mode.
- Development of accurate polychromatic reconstruction algorithms in both Doppler domain and time domain for constant or varying PRI configurations.
- Assessment of the current state of orbit control technology and its impact on the implementability of the multistatic SAR concept. Analysis on the use of varying PRI in terms of developing a realistic system concept.
- Exemplification of the techniques with different system designs and estimation of their performance through simulations.

Considering the contributions listed above, the present work serves as a comprehensive source on innovative polychromatic reconstruction techniques for future Single Input Multiple Output (SIMO) SAR constellations and represents an important asset for the realization of future HRWS imaging SAR systems including Multiple Input Multiple Output (MIMO) SAR constellations.

Chapter 2

Fundamentals and Constraints of Conventional SAR Systems

This chapter introduces the fundamentals of Synthetic Aperture Radar. In the first part of the chapter, the SAR acquisition geometry and basic principles are explained, the signal model of a conventional monostatic system is derived, SAR processing methods are briefly introduced and, finally, the relationship between ambiguity free SAR imaging and the achievable swath width is discussed. The trade-off between azimuth resolution and wide swath represents the system-inherent limitation of conventional SAR systems. The second part of the chapter briefly introduces bistatic and multistatic SAR systems to establish a transition to the next chapters.

2.1 Monostatic SAR

Spaceborne radar is a widely used active remote sensing instrument for Earth and planetary observation, capable of delivering complex images reflecting geometrical and electrical properties of the observed scenes with the additional advantage, when compared to optical systems, of all-day and all-weather operation (Elachi, 1988). Figure 2.1 left shows the geometry of a real aperture radar. Radar images are acquired in a local time-based coordinate system. The spaceborne radar coordinates are called range and azimuth, which roughly correspond to the fast and slow time measurements performed by the radar scaled with the velocity of the electromagnetic wave propagation and the velocity of the spacecraft, respectively. In radar, pulse compression techniques are typically used to optimise the sensitivity-resolution trade-off, and the resolution in range can be straightforwardly expressed as (Skolnik, 1980)

$$\delta r = k_{\mathrm{r}} \frac{\mathrm{c}}{2B_{\mathrm{r}}}, \tag{2.1}$$

where c is the velocity of propagation of the transmitted wave in the considered medium, B_{r} is the bandwidth of the transmitted signal, the factor 2 accounts for the two-way propagation of the radar signal, and k_{r} is a constant close to unity which depends on various factors such as the envelope of the transmitted signal or the weighting used at processing stages. For the sake of compactness, we will assume in the following $k_{\mathrm{r}} = 1$. Moderate range resolutions of radars are better than 100λ where λ is the wavelength; high resolutions approach values of about 10λ, which typically result in metric to decimetric scales. As shown in the right plot of Figure 2.1, the azimuth resolution of a real-aperture radar is proportional to the distance from the radar to the scene, called slant range, and the sensor aperture in azimuth

$$\delta x = k_{\mathrm{a}} r_0 \theta_{\mathrm{a}}, \tag{2.2}$$

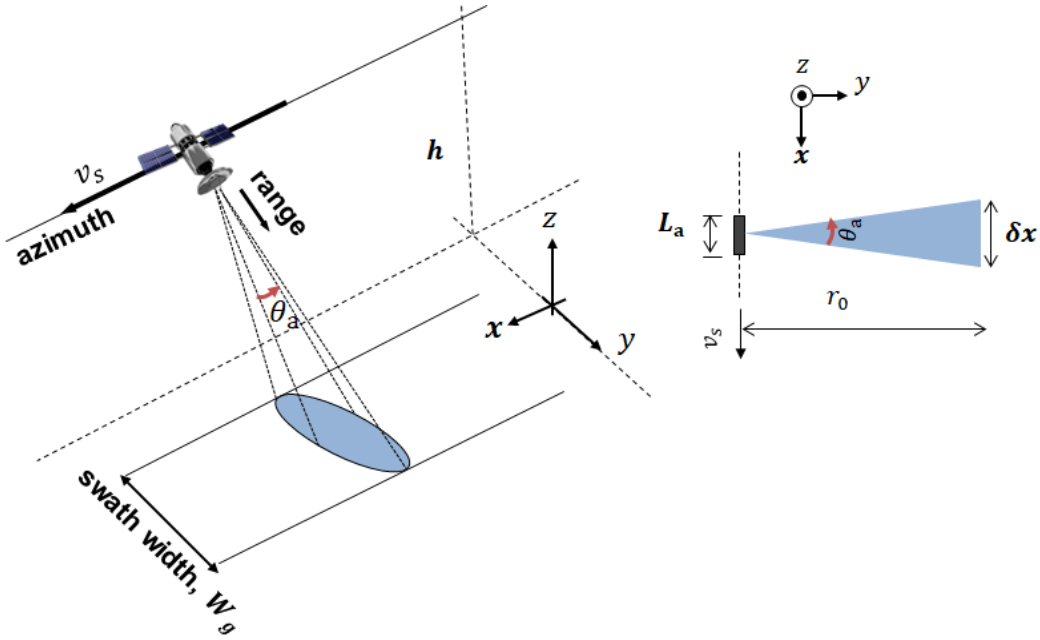

FIGURE 2.1: Side-looking real aperture radar (RAR) geometry (left) and illustration of the azimuth resolution (right).

where r_0 is the slant range, θ_a is the azimuth beamwidth of the radar antenna and k_a is an analogous constant to k_r and can be likewise set to unity. The azimuth aperture angle (beamwidth) is equal to the half-power beamwidth (HPBW) of the antenna. As illustrated in Figure 2.2, this angle is typically half of the angle between the first nulls around the maximum antenna gain. The nulls occur when the emitted waves are out of phase from each other by one-half of a wavelength (Balanis, 1997). Therefore, the azimuth aperture angle can be directly linked to the wavelength of the carrier and the physical length of the antenna as $\theta_a = \lambda / L_a$. By incorporating the azimuth beamwidth definition into Eq. (2.2), the azimuth resolution can be rewritten as

$$\delta x = k_a r_0 \theta_a \approx k_a r_0 \frac{\lambda}{L_a}. \tag{2.3}$$

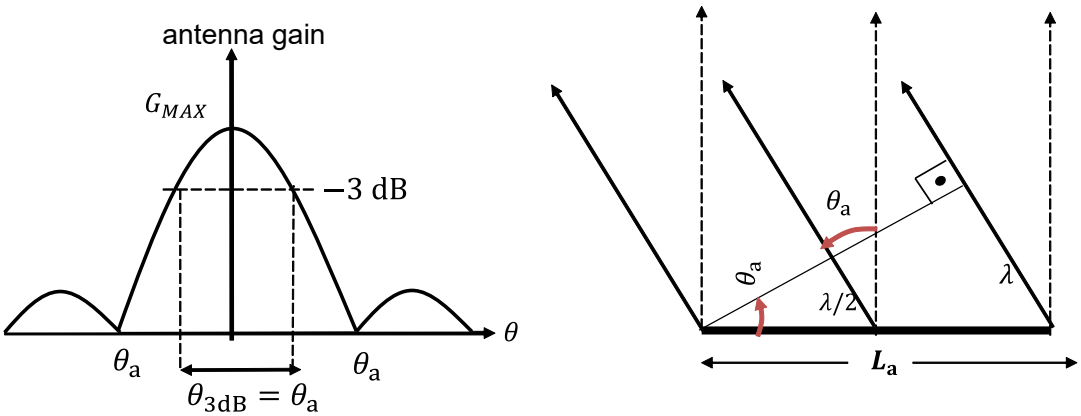

FIGURE 2.2: Relationship of the antenna beamwidth with the wavelength and antenna length.

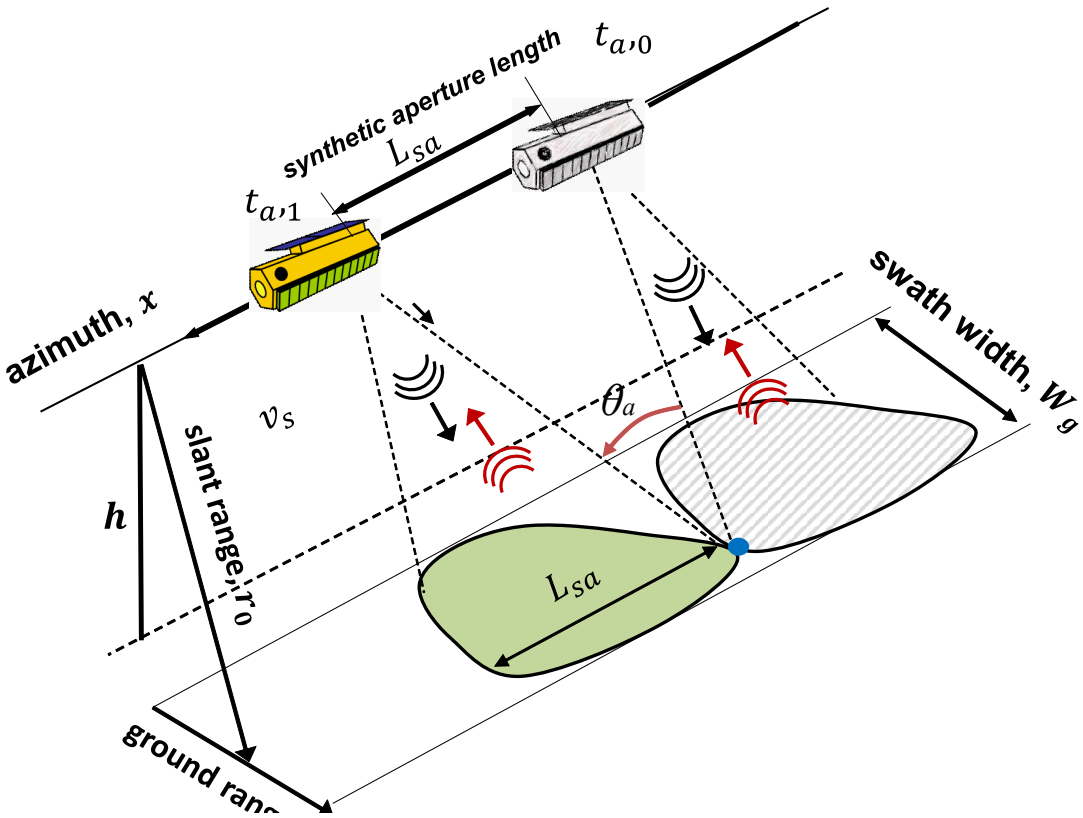

FIGURE 2.3: Sketch of the monostatic SAR geometry. A side-looking radar moves in azimuth with sensor velocity of v_s and transmits pulses in a direction perpendicular to azimuth. The antenna illuminates a swath width of W_g and a synthetic aperture length of L_{sa}.

In Earth observation, typical slant ranges of spaceborne radars vary between hundreds of km and tens of thousands of km from low Earth orbits (LEO) to geosynchronous orbits (GSO). Hence, metric or even decametric azimuth resolutions would require unacceptably large antennas. As a consequence, real aperture radars can only be used to observe physical phenomena in kilometric scales (e.g., oceans).

2.1.1 SAR Geometry

The natural way to overcome the limitations imposed by poor geometric resolutions of a real aperture radar is to coherently integrate the subsequent echoes during processing, hence effectively increasing the effective length of the physical antenna and improving the azimuth resolution of the system. The observation geometry of synthetic aperture radar (SAR) is depicted in Figure 2.3. SAR consists in mounting a radar onto a moving platform at altitude h, so that the radar transmits pulses with a certain Pulse Repetition Frequency (PRF) and records the backscattered echoes. The antenna footprint covers a swath width W_g on the ground and a length of synthetic aperture L_{sa} in azimuth. SARs achieve azimuth resolutions comparable (and usually better) than the ones in range, regardless of the distance to the imaged scene. The length of the effective synthetic antenna is proportional to its footprint on ground, i.e.,

$$L_{sa} \approx r_0 \theta_a = r_0 \frac{\lambda}{L_a}, \tag{2.4}$$

Substituting the antenna length with the length of the synthetic antenna in Eq. (2.2), the azimuth resolution becomes independent of the range to the target and depends

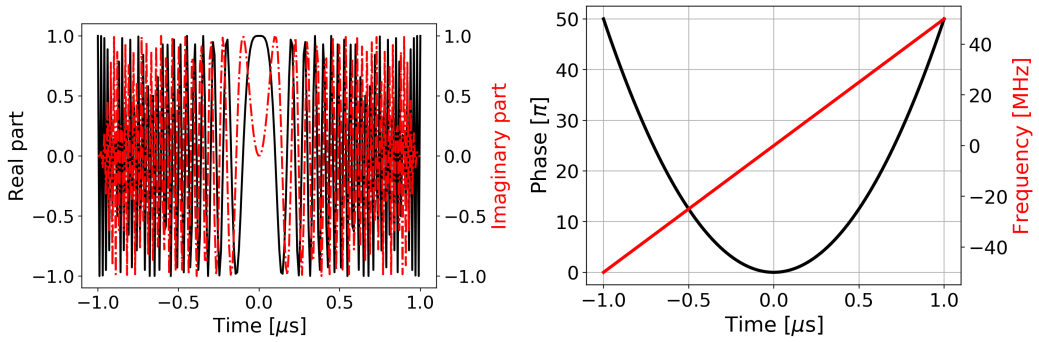

FIGURE 2.4: Amplitude and phase of a baseband linear frequency modulated (FM) pulse (chirp). Left: Chirp amplitude, real (black line) and imaginary (red dotted line) parts. Right: Signal phase (black line) and instantaneous frequency (red line) of the chirp.

only on the physical antenna length as

$$\delta x \approx k_{\mathrm{a}} r_0 \frac{\lambda}{L_{\mathrm{sa}}} = k_{\mathrm{a}} \frac{L_{\mathrm{a}}}{2}, \tag{2.5}$$

where the factor 2 is due to the two-way travel of the radar signal forth and back to the scene. Hence, SARs achieve high range and azimuth resolutions (comparable and even better than optical systems), which coupled with the intrinsic properties of radar (e.g., all-light-and-weather operation, sensitivity to the electromagnetic and geometric properties of the scene), make it a very attractive remote sensing instrument. Moreover, the recording of the phase of the received signals opens a world of potential applications involving very accurate ranging capabilities, such as the measurement of Earth's topography with meter or even sub-meter accuracies, or the estimation of the ground deformation in the mm range.

2.1.2 SAR Signal Model

Typical SAR systems use a baseband linear frequency modulated (FM) signal s_{Tx}, i.e., a so-called *chirp*,

$$s_{\mathrm{Tx,b}}(t_{\mathrm{r}}) = w_{\mathrm{Tx}}(t_{\mathrm{r}}) \exp\left(\mathrm{j}\pi K t_{\mathrm{r}}^2\right) \tag{2.6}$$

where t_{r} is fast time (range time), K is the chirp rate, w_{Tx} is the envelope of the transmitted chirp, expressed as

$$w_{\mathrm{Tx}}(t_{\mathrm{r}}) = \mathrm{rect}\left(\frac{t_{\mathrm{r}}}{\tau}\right) \tag{2.7}$$

and the width of the FM signal is given by τ. Figure 2.4 shows the real and imaginary parts of the chirp signal on the left, and the phase and instantaneous frequency on the right.

The baseband chirp signal is transmitted with a carrier defined by the wavelength as

$$s_{\mathrm{Tx}}(t_{\mathrm{r}}) = s_{\mathrm{Tx,b}}(t_{\mathrm{r}}) \exp\left(\mathrm{j}2\pi \frac{\mathrm{c}}{\lambda} t_{\mathrm{r}}\right). \tag{2.8}$$

The SAR signal propagates towards the ground, where it is scattered by a point target at a closest distance of r_0 from the transmitter. The scattered echo is then collected by the receive antenna. After down-conversion and sampling, the radar

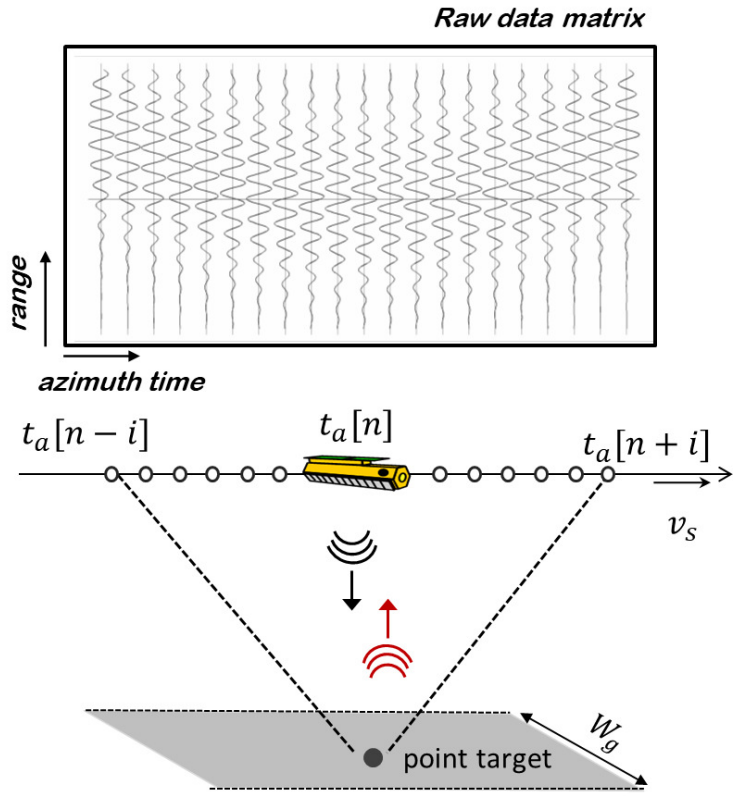

FIGURE 2.5: Sketch of SAR data acquisition. The echoes of the same target acquired within the synthetic aperture are stored in the so-called raw data matrix for a coherent combination during SAR processing. This combination of multiple Doppler-shifted echoes improves the along-track resolution.

return of a single point target is expressed as (Cumming and Wong, 2005)

$$\begin{aligned} s_{\mathrm{Rx}}(t_\mathrm{r}, t_\mathrm{a}; r_0) =& v w_\mathrm{a}(t_\mathrm{a}) s_{\mathrm{Tx,b}}\left(t_\mathrm{r} - \frac{2r(t_\mathrm{a}; r_0)}{\mathrm{c}}\right) \exp\left[-\mathrm{j}\frac{4\pi}{\lambda} r(t_\mathrm{a}; r_0)\right] \\ =& v w_\mathrm{a}(t_\mathrm{a}) w_{\mathrm{Tx}}\left(t_\mathrm{r} - \frac{2r(t_\mathrm{a}; r_0)}{\mathrm{c}}\right) \exp\left[-\mathrm{j}\frac{4\pi}{\lambda} r(t_\mathrm{a}; r_0)\right] \\ & \exp\left[\mathrm{j}\pi K\left(t_\mathrm{r} - \frac{2r(t_\mathrm{a}; r_0)}{\mathrm{c}}\right)^2\right], \end{aligned} \tag{2.9}$$

where v is an arbitrary complex constant that accounts for the reflectivity, propagation attenuation, chain gains and further losses, t_a is the slow time (azimuth time), w_a is the azimuth envelope given by the square of the antenna pattern, and $r(t_\mathrm{a}; r_0)$ is the range history of the target. Note that the range history depends on the range r_0 and the radar positions along the aperture x, which has an impact on the processing strategies of the SAR data. SAR echoes are composed by the space-variant convolution of the scene reflectivity and the impulse response of the system. Figure 2.5 depicts the two-dimensional coherent raw SAR data formation of a point target. Depending on the system, the raw data can either be downlinked for processing or be processed on board. After the processing, a high-resolution two-dimensional reflectivity map of the observed scene is obtained.

The first exponential term of (2.9) corresponds to the modulation of the radar carrier introduced by the motion of the platform in the azimuth direction, usually

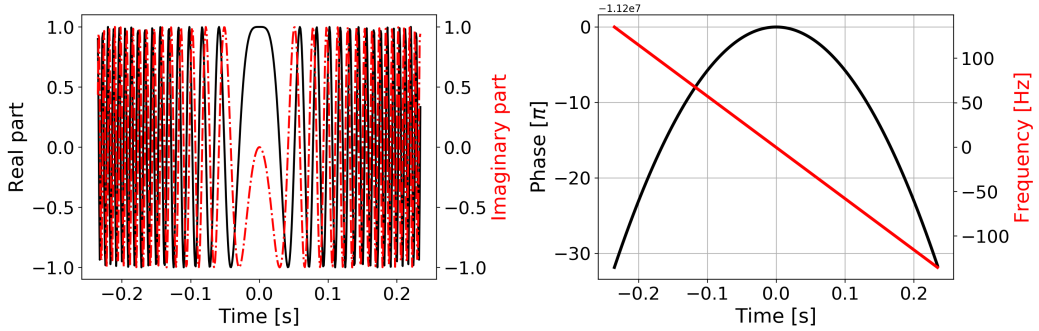

FIGURE 2.6: Amplitude and phase of the modulation along the azimuth direction. The azimuth modulation, i.e., azimuth chirp, is a function of the slant range, platform velocity and slow time [see Eq. (2.11)]. Left: Amplitude of the azimuth modulation, real (black line) and imaginary (red dotted line) parts. Right: Phase (black line) and instantaneous frequency (red line) of the azimuth modulation. Note the similarity to the amplitude and phase of the transmitted chirp in Figure 2.4.

known as Doppler, whereas the second exponential term is the delayed transmitted FM signal. Figure 2.6 shows the real and imaginary parts of the azimuth modulation on the left, and the phase and instantaneous frequency on the right. In the simplified case of a linear-track geometry, the range history can be expressed as

$$r(t_a; r_0) = \sqrt{r_0^2 + v_s^2 t_a^2}, \tag{2.10}$$

where v_s is the platform velocity. Applying a second-order Taylor expansion to the range history allows for defining the azimuth modulation phase in terms of a constant and a quadratic part (FM signal, azimuth chirp), namely,

$$\phi_{AC}(t_a; r_0) = -\frac{4\pi}{\lambda} r(t_a; r_0) \approx -\frac{4\pi}{\lambda}\left(r_0 + \frac{v_s^2 t_a^2}{2r_0}\right). \tag{2.11}$$

The instantaneous Doppler frequency, f_D, is expressed as the derivative of ϕ_{AC}

$$f_D = \frac{1}{2\pi}\frac{\partial \phi_{AC}(t_a; r_0)}{\partial t_a} = -\frac{2v_s^2 t_a}{\lambda r_0} \tag{2.12}$$

which is confined within

$$\begin{aligned} f_{DC} - \frac{B_a}{2} \leq f_D \leq f_{DC} + \frac{B_a}{2}, \\ B_a \approx \frac{2v_s}{L_a} \end{aligned} \tag{2.13}$$

where f_{DC} is the Doppler centroid and B_a is the azimuth bandwidth of the signal.

The footprint velocity, v_g, of an airborne SAR system operating in stripmap mode is equal to the platform velocity v_s. Considering the satellite orbit, the Earth's curvature and rotation, the geometry of the satellite SAR data is more complicated. As shown in (Cumming and Wong, 2005), the range history of a target in spaceborne SAR case, as well as the Eqs. (2.9)-(2.13), can be computed with an effective velocity, v_e, given by

$$v_e = \sqrt{v_s v_g}. \tag{2.14}$$

The effective velocity varies slowly both in the range and azimuth dimensions due

to the curved orbit and Earth's rotation, and it also depends on the topography (Rodriguez-Cassola et al., 2014). Typically, the effective radar velocity of each point target within the illumination time is assumed to be constant (Wong, Ngee Leng Tan, and Tat Soon Yeo, 2000).

2.1.3 SAR Signal Processing

The task of the SAR processing algorithm is to deconvolve the SAR echoes to retrieve the scene reflectivity. This scene reflectivity depends on the imaged scene and can be, in general, assumed to be a circular Gaussian white random process. The consequences of the latter are relevant: in most cases, the bandwidth of the SAR data is full at any instant since the spectrum of the white noise contains all of the spectral components, which prevents the generalized superresolution approaches to be systematically used in SAR processing. This, linked to the typical low SNR of radar echoes, supports the idea of SAR processing being done via matched filtering.

The SAR transfer function of a target at the range bin r_0 can be computed analytically for a linear-track geometry using an asymptotic approximation, known as the principle of stationary phase (Papoulis, 1965), and takes the form

$$H(f_\mathrm{r}, f_\mathrm{a}; r_0) = S_\mathrm{Tx}(f_\mathrm{r}) \exp\left[-\mathrm{j}\frac{4\pi}{\lambda} r_0 \sqrt{\left(1+\frac{f_\mathrm{r}}{f_0}\right)^2 - \left(\frac{\lambda f_\mathrm{a}}{2v_s}\right)^2}\right], \tag{2.15}$$

where $S_\mathrm{Tx}(f_\mathrm{r})$ is the Fourier transform of the transmitted signal, f_0 is the carrier frequency which is related to the wavelength as $\lambda = \mathrm{c}/f_0$, f_r is the baseband range frequency confined within the range bandwidth, B_r, as $-B_\mathrm{r}/2 \leq f_\mathrm{r} \leq B_\mathrm{r}/2$ and f_a is the azimuth frequency. The frequency variables refer to the range and azimuth times in (2.9), respectively. Typical SAR signals, chirps, show a constant amplitude in both time and frequency domains. The matched filter of the SAR impulse response approximates its inverse filter, which supports the idea of the bandwidth being used efficiently. As a consequence, matched filtering the SAR echoes delivers focused radar images.

SAR processing consists of the efficient implementation of the range-variant filter of Eq. (2.15), which can be done both in time and frequency domains. Time-domain algorithms, known as backprojection, perform the convolution in the time domain and are arbitrarily exact even when dealing with strongly non-linear surveys (Bauck and Jenkins, 1989). The expression of the backprojection algorithm is

$$i = \int_T \mathrm{d}t_\mathrm{a} d\left(\frac{r(t_\mathrm{a})}{\mathrm{c}}, t_\mathrm{a}\right) \exp\left\{\mathrm{j}\frac{4\pi}{\lambda}[r(t_\mathrm{a}) - r_0]\right\}, \tag{2.16}$$

where i is the image value at range-time coordinates (t_a, r_0) as illustrated in Figure 2.5, T is the integration time, and d is the range-compressed data. In this approach, the integration is done in azimuth time following the migration of the radar echoes in fast time. The canonical implementation of Eq. (2.16), though exact (up to negligible interpolation errors), suffers from severe inefficiency, which grows linearly with increasing swaths and quadratically with increasing acquisition times or resolution. Efficient implementations of (2.16), called fast backprojection, are based on the divide-and-conquer paradigm (Yegulalp, 1999; Ulander, Hellsten, and Stenström, 2003).

Frequency-domain algorithms, on the other hand, benefit from the fast convolution property of the Fourier transform, and can be divided into monochromatic and

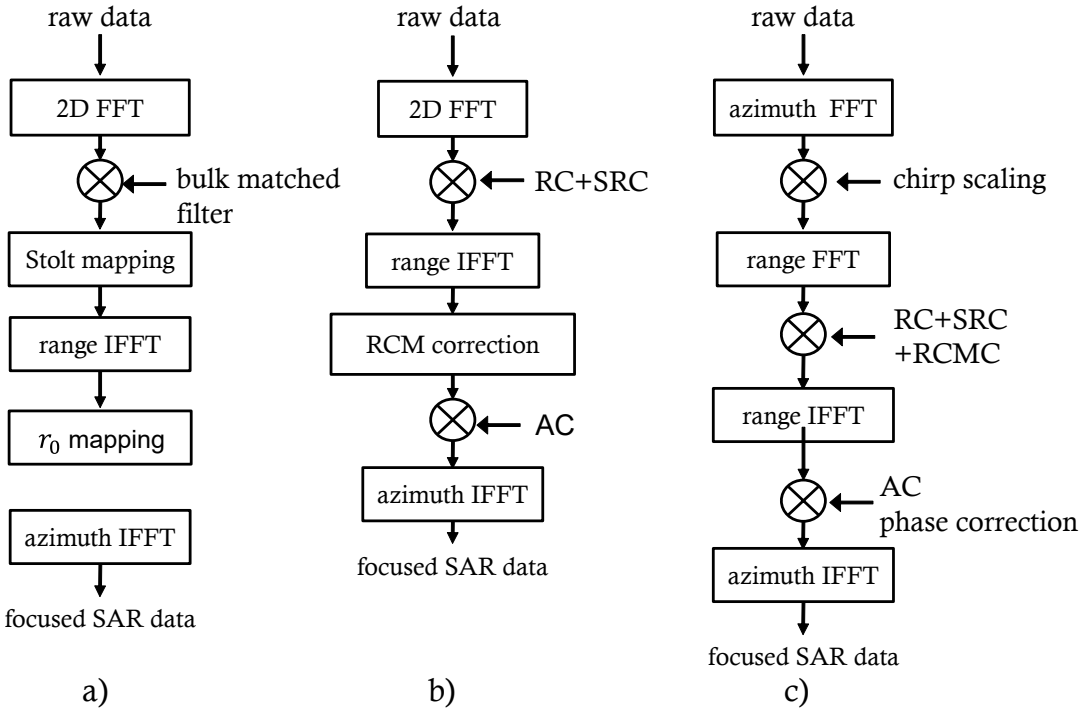

FIGURE 2.7: Block diagrams of frequency domain processing algorithms a) $\Omega\kappa$, b) range-Doppler c) chirp scaling. As a first step, raw data in 2D time domain are brought to either 2D frequency domain (wavenumber domain) or range-time and Doppler-frequency domain. The abbreviations in the block diagrams stand for RC: range compression, SRC: secondary range compression, RCMC: range cell migration correction and AC: azimuth compression.

polychromatic. The block diagrams of well known frequency-domain algorithms are shown in Figure 2.7. The first step of polychromatic kernels, known as $\Omega\kappa$ algorithm, is bringing the data to the wavenumber domain and then applying bulk matched filtering, which focuses a target at the reference range perfectly and the other targets become only partially focused. The differential focusing is based on an interpolation in the 2D frequency domain following the law

$$\sqrt{\left(1+\frac{f_\mathrm{r}}{f_0}\right)^2-\left(\frac{\lambda f_\mathrm{a}}{2v_s}\right)^2}\rightarrow\frac{f'_\mathrm{r}}{f_0}+1. \tag{2.17}$$

This operation replaces the 2D frequency dependent terms of the remaining phase with the shifted and scaled range frequency variable, $\frac{f'_\mathrm{r}}{f_0}+1$. After the inverse Fourier transform in range, the data is resampled in the fast-time domain to ensure a well focused image. The interpolation, known as Stolt mapping (Stolt, 1978), is sensitive and has to be performed very accurately. The advantage is that polychromatic kernels accommodate the range-variance along the whole bandwidth in typical cases. The requirements on the interpolation accuracy can be relaxed if monochromatic kernels are used, which give the latter a small edge in efficiency.

In monochromatic approaches, the phase of Eq. (2.15) is approximated by a Taylor expansion in f_r, i.e.,

$$\begin{aligned}\phi(f_r, f_a; r_0) \cong & -\frac{4\pi}{\lambda} r_0 \sqrt{1-\left(\frac{\lambda f_a}{2v_s}\right)^2} - \frac{4\pi}{c} \frac{r_0}{\sqrt{1-\left(\frac{\lambda f_a}{2v_s}\right)^2}} f_r + \\ & \pi \left[\frac{1}{K} + \frac{\lambda^3 r_{0_a}^2}{2c^2 v_s^2 \left(1-\left(\frac{\lambda f_a}{2v_s}\right)^2\right)^{\frac{3}{2}}}\right] f_r^2 \\ & = \phi_{AC} - 2\pi t_{rcm}(f_a) f_r + \pi \left(\frac{1}{K} + \frac{1}{\beta_{src}}\right) f_r^2,\end{aligned} \tag{2.18}$$

where ϕ_{AC} is the phase azimuth modulation term, $t_{rcm}(f_a)$ is the range cell migration (RCM) curvature of the signal in the range-Doppler domain. The RCM correction, due to its space-variant nature, is considered as the most challenging step of SAR processing. The third term is composed of the chirp phase and the quadratic terms of the coupling between range and azimuth dimensions.

The first monochromatic approach, range-Doppler algorithm, starts with the range compression (RC), the convolution of the data with the complex conjugate of the transmitted signal, and the secondary range compression (SRC) in the wavenumber domain. Figure 2.8 shows the steps of the range-Doppler processing algorithm.[1] As shown in the top-right plot of Figure 2.8, range compressed data cross several range bins and form a hyperbolic curve, a concept called range cell migration (RCM). The range-dependent RCM takes its shape from $r(t_a; r_0)$ and, should be corrected by a non-stationary two-dimensional reference function. After RCMC correction, the energy of the point targets is aligned in a single range bin (bottom-left plot of Figure 2.8). Similar to the range dimension, a matched filter in the azimuth direction is applied to compress the energy as a final step, called azimuth compression (AC). Figure 2.9 shows a zoomed focused impulse response of the middle target in 2D and 1D (both in azimuth and range). Focusing the raw SAR data by matched filtering produces an impulse response with a two-dimensional *sinus cardinalis* (sinc) response.

The second monochromatic approach, the chirp scaling algorithm, aims at circumventing the interpolation step required for RCMC by modifying the chirp rate of the received raw data at the expense of a slightly worse performance. After an azimuth Fourier transform, the chirp scaling (differential RCMC) is applied to equalize the RCM of all targets. The second step that includes RC, SRC and RCMC for the reference target is applied in the wavenumber domain. The last step deals with the azimuth compression and phase correction due to the chirp scaling term.

The approximation in (2.18) is typically good for moderate swath widths and resolutions (e.g., TerraSAR-X and TanDEM-X (Krieger et al., 2007)), but breaks down for increasing swath widths, larger transmitted bandwidths or larger integration times.

[1] A real SAR scene response corresponds to densely located distributed and point targets. In that case, each azimuth and range bin of the raw data matrix accommodates the superposition of the received energy from multiple targets. The targets at the same range cell share the RCM curvature with a shift according to their zero-Doppler time. After the matched filtering, the received energy of each target is compressed to the corresponding resolution cell in the data matrix.

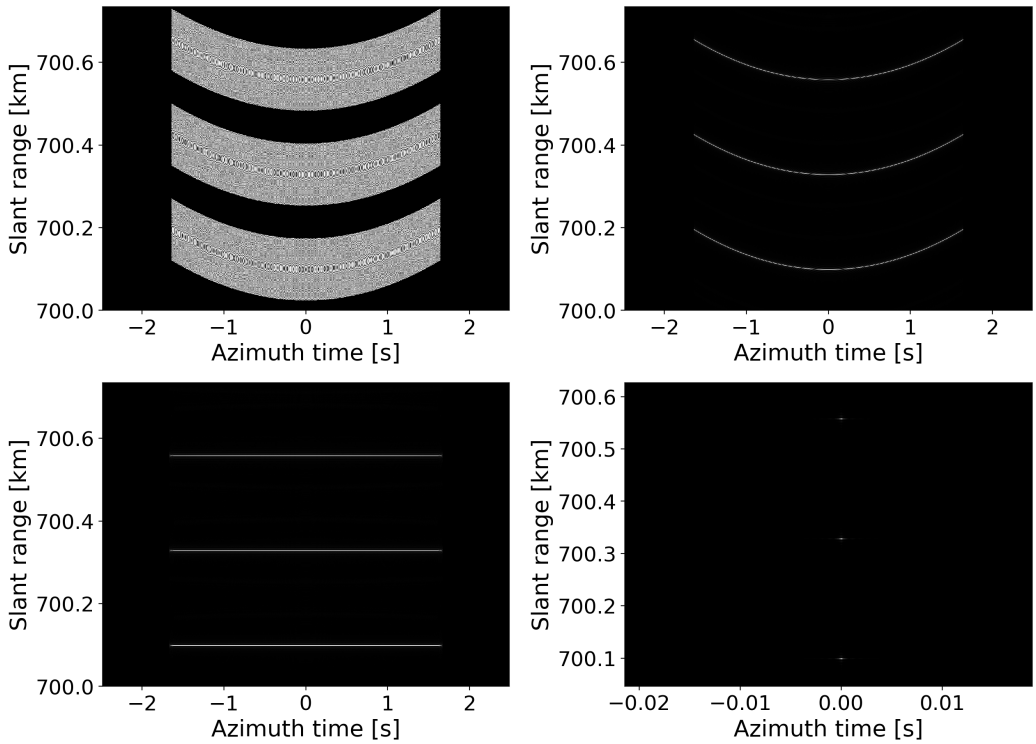

FIGURE 2.8: SAR processing steps of an image with three targets with the range-Doppler algorithm shown in Figure 2.7 b. (Top-left) Real part of the raw data, (top-right) amplitude of range-compressed data, (bottom-left) amplitude of range-compressed data after RCMC, (bottom-right) amplitude of the final compressed image.

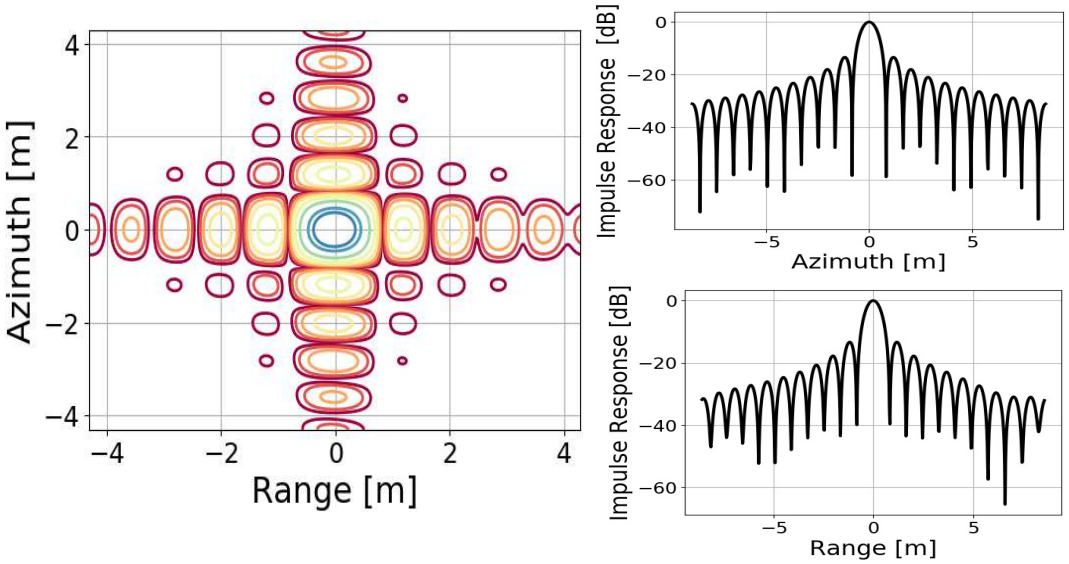

FIGURE 2.9: Zoomed impulse response function (IRF) of a focused point target. (Left) Amplitude of the 2D IRF, (right) intensity of the 1D IRF in azimuth (top) and range (bottom).

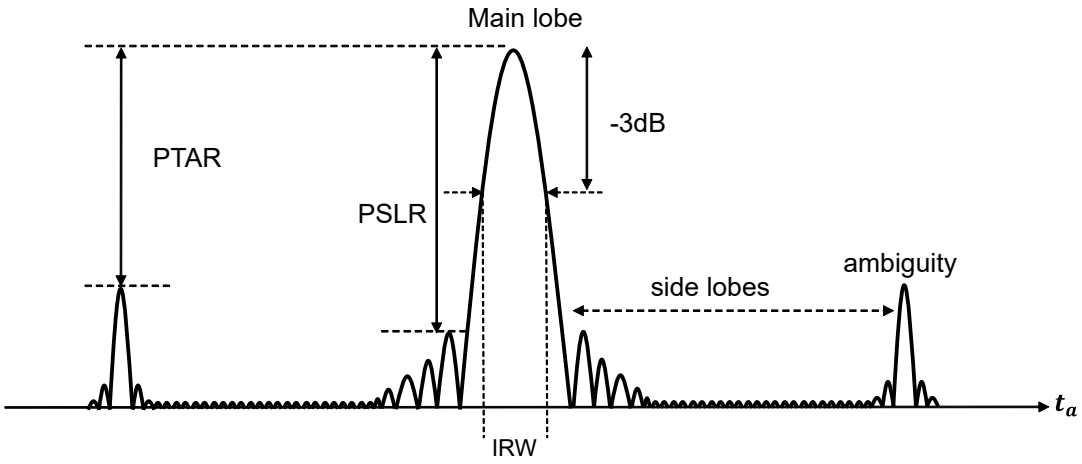

FIGURE 2.10: Impulse response function of a SAR point target and illustration of quality parameters.

The advantage of such a processing approach is that interpolation-free implementations can be done, which increases the efficiency of the algorithms (Moreira, Mittermayer, and Scheiber, 1996). As already stated, polychromatic SAR processing in the Fourier domain requires usually a sensitive interpolation in the wavenumber domain, but can handle the range-variance and the wideband character of the transmitted signal much more accurately. Note that (2.16) stays valid for any kind of SAR range histories, whereas (2.15) is specifically valid for linear (monostatic) SAR surveys.

2.1.4 System Performance

It is informative to examine a two-dimensional point target response in time domain to evaluate the system performance. This section presents the quality metrics used in this thesis that are obtained from an impulse response. Figure 2.10 illustrates a typical 1D impulse response and quality metrics (valid for both azimuth and range dimensions).

- Impulse Response Width (IRW) is the value referred to as SAR image resolution. It is the width of the mainlobe of the impulse response function 3 dB below the peak value. The units can be either pixels or meters.
- Peak-to-Sidelobe Ratio (PSLR) is the ratio, in dB, between the highest sidelobe intensity and the mainlobe intensity. High sidelobes may lead to false targets or suppression of the weak targets. The nominal PSLR for a sinc-like response is -13.6 dB.
- Integrated Sidelobe Ratio (ISLR) is the ratio, in dB, between the energy of the mainlobe and the energy of the sidelobes on both sides of the mainlobe. Typically 10 to 20 sidelobes from both sides of the mainlobe are included in the computation and, for a sinc, it is around -10 dB.
- Peak-to-Ambiguity Ratio (PTAR) is the ratio, in dB, between the mainlobe and ambiguities. The next section will present in a more detailed way why ambiguities occur in SAR. As in PSLR, high ambiguities may lead to false targets or suppression of the weak targets.

TABLE 2.1: List of weighting functions. Broadening (k_a/k_r in Eqs. (2.1) and (2.2)) is the factor that multiplies the resolution (IRW).

Window	PSLR (dB)	ISLR (dB)	k_a/k_r (-3 dB)
Rectangular	-13.6	-10	0.89
Triangle	-27	-19	1.28
Hanning	-32	-21	1.44
Hamming	-43	-20	1.30
Blackman ($\alpha = 0.16$)	-58	-19	1.68
Gaussian 3.5	-69	-17	1.79

Due to the low nominal performance parameters of the sinc-like SAR impulse response, it is common to use weighting functions at the cost of geometric resolution loss. Typical weighting functions are Hamming, Hanning, Blackman and Gaussian. Their main properties can be found in Table 2.1 (Harris, 1978).

2.1.5 Constraints

As mentioned in the previous section, the radar transmits pulses with a pulse duration τ, and with a pulse repetition frequency, PRF, and receives the corresponding echoes with a time delay. The total transmit/receive operation is repeated every pulse repetition interval (PRI), hence, PRF determines the sampling frequency of the SAR raw data in azimuth. According to the Nyquist-Shannon sampling theorem, a continuous-time signal should be sampled with a frequency greater or equal to the Doppler bandwidth B_a to capture all the information. Assuming band-limitation, a sampling frequency lower than the Doppler bandwidth causes back-folding of the Doppler spectrum, i.e., aliasing, and consequently, raises ambiguities in the focused SAR image.

Figure 2.11 shows two sampling scenarios, namely, properly sampled and undersampled data, and its implications in terms of SAR imaging. The top row shows the amplitude of the antenna pattern in the Doppler spectrum, the middle row shows the time-bandwith diagrams (TBD) and finally the bottom row shows the impulse responses in both sampling scenarios. On the left, $PRF > B_a$ is illustrated where the sampling ratio ensures the complete recovery of the information, and consequently, no ambiguities. On the right, the undersampling scenario is sketched, where the Doppler spectrum experiences aliasing, hence, certain parts of the azimuth bandwidth cannot be recovered and ambiguities occur. The amplitude of the ambiguities is determined by the energy in the aliased Doppler spectrum. Revisiting the azimuth resolution equation in (2.5),

$$\delta x = \frac{L_a}{2} = \frac{v_g}{B_a} \geq \frac{v_s}{PRF} \tag{2.19}$$

requires the agreement between desired azimuth resolution and minimum PRF to avoid ambiguities.

As any other radar system, SAR also has to cope with range ambiguities. The range ambiguities occur when echoes from targets illuminated by the sidelobes of the antenna pattern in range arrive at the receiver at the same time despite their different flight time. Figure 2.12 illustrates the occurrence of range ambiguities, the corresponding SAR transmit/receive timing diagram and the ambiguity-free ideal timing diagram for a constant PRI scenario. The return of pulse n from the swath

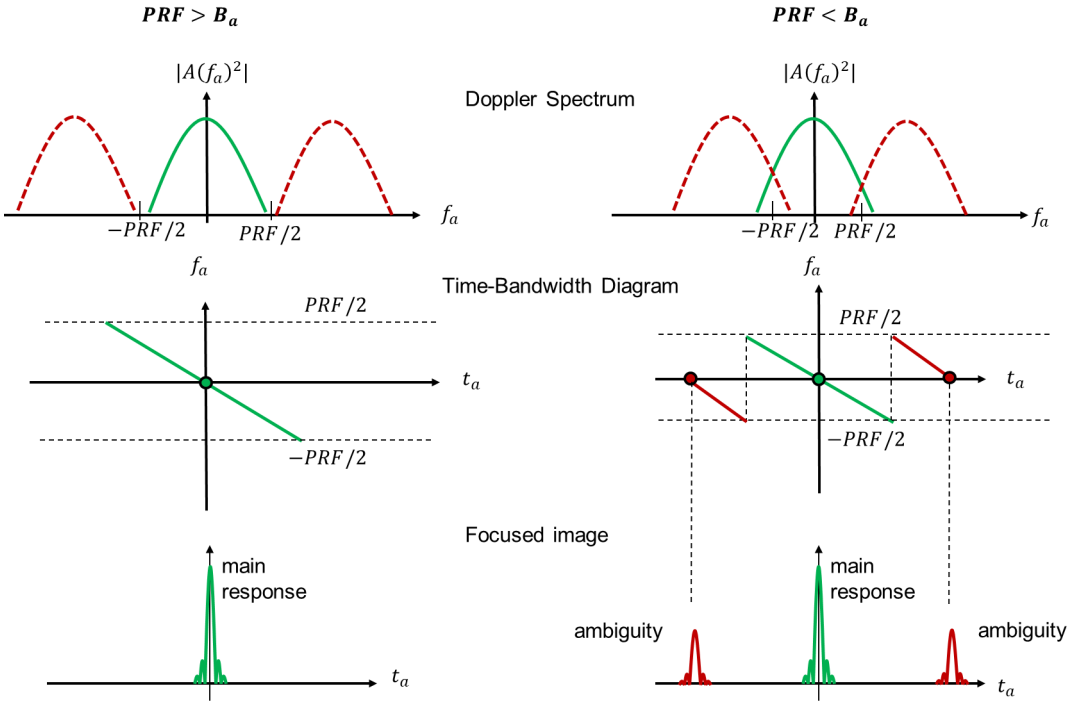

FIGURE 2.11: Doppler spectrum of azimuth antenna pattern (top), corresponding Doppler frequency characteristic of a point target after sampling (middle), and impulse response after focusing (bottom). Left: The sampling frequency is large enough to comply with Nyquist sampling theory and ambiguities are avoided. Right: The Doppler spectrum experiences back-folding because of undersampling and consequently, ambiguities arise.

width $[r_{min}, r_{max}]$ and the return of pulse $n+i$ from $r_0 - \frac{c}{2}PRI$ arrive at the receiver simultaneously. It is therefore clear that the swath width (W_g) is constrained by the antenna height and the PRF. An upper limit of the footprint for a given PRF in terms of ground range coverage can be expressed as

$$r_{max} - r_{min} = \frac{c}{2}PRI \longleftrightarrow W_g = \frac{\mathrm{c}}{2\sin(\theta_i)PRF}, \tag{2.20}$$

where θ_i is the incidence angle. This equation suggests that a lower PRF, i.e., a coarser azimuth resolution, results in a longer receive window, hence, enabling wide swath.

Combining the requisites of ambiguity free SAR survey defined by (2.20) and (2.19), the relation

$$\frac{W_g}{\delta_{az}} < \frac{\mathrm{c}}{2\sin(\theta_i)v_s} \tag{2.21}$$

represents the limitation of a conventional SAR system, namely, the trade-off between azimuth resolution and swath width. A high-resolution SAR system can be realized only at the expense of swath width, or, similarly, a wide swath mode SAR is only possible at the expense of a low azimuth resolution.

2.2 Bistatic and Multistatic SAR

A monostatic radar uses the same antenna for transmission and reception. A bistatic radar, on the other hand, has separate antennas for transmission and reception. In the case of spaceborne radars, this separation of the antennas usually becomes a

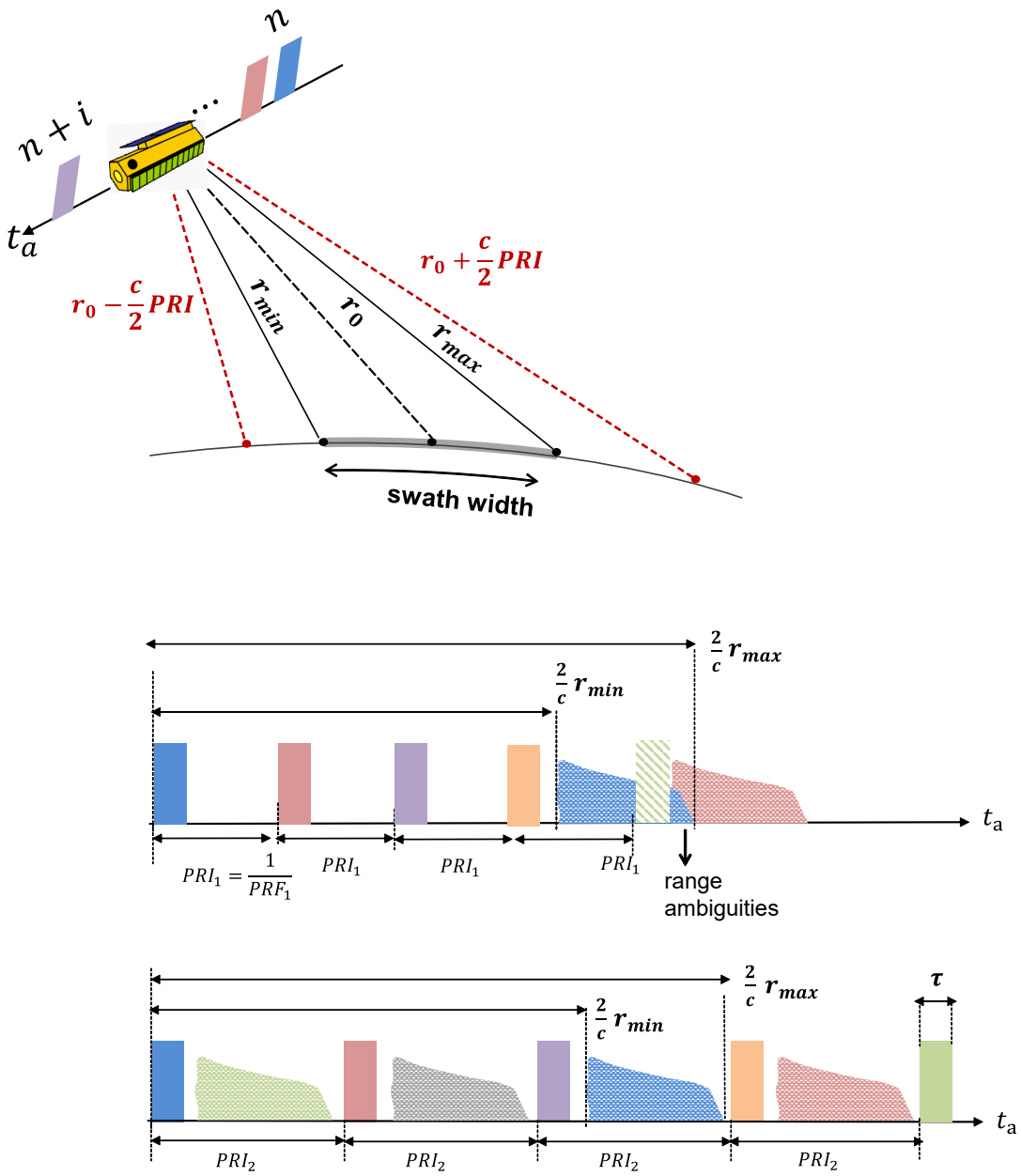

FIGURE 2.12: Illustration of the relationship between range ambiguities and transmit-and-receive timing diagram. The radar first operates in transmit mode and emits bursts of pulses for pulse duration τ, then switches to receive mode and starts collecting the echoes of previous pulses. This cycle is repeated every pulse repetition interval. The range ambiguities arise when the radar receives echoes of pulses coming from areas illuminated by the sidelobes of the range antenna pattern, i.e., outside the swath. They occur if the range difference of the respective ambiguous targets with respect to the slant ranges of the swath is $k\frac{c}{2}PRI, k \in \mathbb{Z}$. The bottom diagram shows the ambiguity-free transmit/receive time diagram at the expense of a higher PRI ($PRI_2 > PRI_1$, lower azimuth resolution).

separation of instruments and spacecrafts, with two basic implications (Rodriguez-Cassola, 2012): a) the geometry becomes more intricate and Eq. (2.10), (2.15) and (2.17) do not hold anymore, and b) low-frequent time and phase drifts of the radar instruments do not cancel out after mixing. This poses a series of challenges in the operation of the bistatic radar which can be basically summarized in two: a) SAR image formation becomes more elaborate (D'Aria, Guarnieri, and Rocca, 2004; Cantalloube et al., 2004; Bamler, Meyer, and Liebhart, 2006; Rodriguez-Cassola et al., 2011), and b) the time and phase drifts of the instruments need to be calibrated (i.e., synchronized), otherwise accurate SAR processing is not possible (Cantalloube et al., 2004; Lopez-Dekker et al., 2008). Bistatic SAR offers many advantages with respect to monostatic SAR, among which the following can be listed: a) silent operation, b) flexibility in the observation geometry, c) improved performance, and d) possibility to operate the system in single-pass interferometric mode, which allows for ranging accuracies in the order of the carrier wavelength (e.g., *à la* TanDEM-X) (Krieger and Moreira, 2003).

Bistatic SAR processing, when compared to monostatic SAR, presents basically two major differences: a) range histories are non-hyperbolical, which prevents from deriving accurate analytical expressions for the SAR transfer functions, and b) the bistatic SAR survey is not only range-variant, but also azimuth-variant. Therefore, the matched filter becomes 2D-variant, which poses a major challenge for efficient implementations (Rodriguez-Cassola, 2012).

2.2.1 Bistatic SAR Processing

From the signal processing point of view, Eq. (2.15) is still valid for bistatic cases, only r represents one half of the two-way range transmitter-target-receiver and cannot be approximated by (2.10). A common approach in the literature is splitting the bistatic range history in two linear-track contributions from transmitter and receiver, i.e.,

$$r(t_a) \approx \frac{\sqrt{r_{0,\mathrm{Tx}}^2 + v_{\mathrm{Tx}}^2 t_a^2} + \sqrt{r_{0,\mathrm{Rx}}^2 + v_{\mathrm{Rx}}^2 (t_a - \Delta t_a)^2}}{2}, \tag{2.22}$$

where the term Δt_a accounts for the along-track separation between transmitter and receiver. The advantages of using (2.22) in bistatic SAR are, however, not so clear as using (2.10) in monostatic SAR. Note that the linear-track model is only an approximation to the true orbital geometries. Nevertheless, it is a beneficial approximation in the monostatic case since it allows to express SAR image formation algorithms analytically. In the bistatic case, however, the linear-track model does not allow for a compact analytical description of the algorithms; not even in the simplified tandem case with $v_{\mathrm{Tx}} = v_{\mathrm{Rx}}$ and $r_{0,\mathrm{Tx}} = r_{0,\mathrm{Rx}}$ can the bistatic SAR transfer function be expressed in a compact manner, and the compact expressions in the literature often suffer from severe lack of accuracy. Using the true geometry of the bistatic SAR, the SAR transfer function can be approximated using the principle of stationary phase (Papoulis, 1965) as

$$H(f_r, f_a; r_0) = S_{\mathrm{Tx}}(f_r) \exp\left\{-\mathrm{j}2\pi \left[2\frac{f_r + f_0}{c} r(t_a^\star) + f_a t_a^\star\right]\right\}, \tag{2.23}$$

where the $t_a^\star$ is the time of stationary phase of the Fourier transform, which depends on both range and azimuth frequencies and can be computed solving the equation

(Carrara, Goodman, and Majewski, 1995; Cumming and Wong, 2005)

$$\left.\frac{\mathrm{d}r(t_\mathrm{a})}{\mathrm{d}t_\mathrm{a}}\right|_{t_\mathrm{a}=t_\mathrm{a}^\star} = -\frac{\mathrm{c}f_\mathrm{a}}{f_\mathrm{r}+f_0}. \tag{2.24}$$

Note that this equivalence is valid for both monostatic SAR with (2.10) and bistatic SAR with (2.22), however, Eq. (2.24) employs the bistatic range history.

The same paradigms as in the monostatic SAR case hold for bistatic SAR, and processing approaches can be effected both in time and frequency domains (Rodriguez-Cassola, 2012). Efficient time-domain approaches, however, are in principle better suited to handle the intrinsic azimuth variance of bistatic SAR surveys (Rodriguez-Cassola et al., 2011). Monochromatic and polychromatic Fourier-based approaches require an azimuth-invariant kernel followed by azimuth-variant residual corrections, unless both transmitter and receiver have a common orbit height.

2.2.2 Multistatic SAR

Multistatic SAR is a constellation of monostatic and bistatic SARs which can benefit from the availability of more transmit and receive channels for boosting the performance of the system. In particular, multistatic constellations may have improved revisit times, access, image throughput, swath width, resolution, and imaging capabilities. Depending on whether one or several transmitters are available and on the application (the processing of the data depends strongly on the intended application), the multistatic constellation can be classified as a Single Input Multiple Output (SIMO) or Multiple Input Multiple Output (MIMO) system. The multistatic SAR constellation can be at any instant fully described by the family of impulse response cubes

$$\mathbf{h}_\mathrm{multi} = \{h(r_i(\mathbf{b}_i))\}, \tag{2.25}$$

where r_i is the range history corresponding to the i-th bistatic subset in the constellation and $\mathbf{b}_i$ are the baseline vectors. The processing on $\mathbf{h}_\mathrm{multi}$ will depend on the intended applications of the multistatic SAR constellation. However, from a SAR processing point of view one can aim at separating these into two main groups:

- The data of any bistatic unit of the multistatic constellation are sampled according to the Nyquist criterion. Classical bistatic SAR image formation techniques can be applied on the data, and the combination of the focused data shall take place at image level. Resolution enhancement techniques (Prati and Rocca, 1992; Massonnet and Souyris, 2008; Prats et al., 2011) for general homogeneous scenes happen typically in a dense signal space. Other applications like layover solving and urban tomography are rather on a sparse signal space paradigm (Gini, Lombardini, and Montanari, 2002; Zhu and Bamler, 2010; Fornaro and Serafino, 2006).

- The data of the bistatic units of the multistatic constellation are sampled below Nyquist. Figure 2.13 shows the transmit/receive timing diagram of a multistatic constellation. A reconstruction of the signal received from different units (i.e., channels or receivers) needs to be performed before SAR image formation occurs. The reconstruction of general homogeneous scenes has to assume a dense signal space (Aguttes, 2003; Krieger, Gebert, and Moreira, 2004b; Gebert,

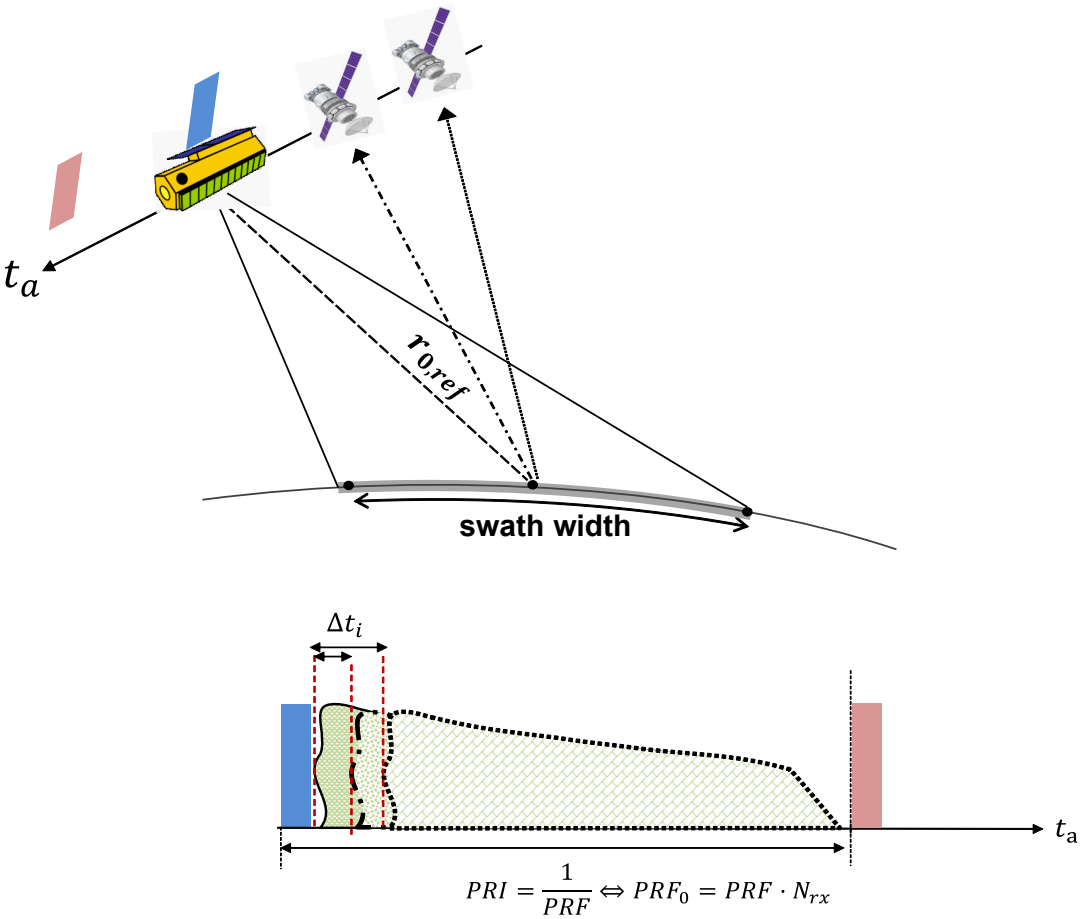

FIGURE 2.13: Transmit-and-receive timing diagram of a multistatic SAR constellation in along-track. The echoes of each transmitted pulse are received by several receivers and, optionally, by the transmitter. This allows for a reduction of the PRF to reduce range ambiguities, while the sampling frequency in azimuth is increased by multi-reception. PRF_0 is the Nyquist frequency of a conventional monostatic SAR sensor, and Δt_i represents the time delay between the receivers due to the bistatic geometry (see Subsection 3.1.1).

Krieger, and Moreira, 2009; Pinheiro et al., 2015a). The reconstruction of heterogeneous areas and point-like and extended targets under Nyquist may happen in a sparse signal space (Salzman et al., 2002; Larsson, Stoica, and Li, 2002; Tello-Alonso, Lopez-Dekker, and Mallorqui, 2010; Pinheiro et al., 2015a).

This thesis sets the focus on the latter class. The improvement of the radar performance by sampling below Nyquist is based on the idea of twisting the well-known time-frequency trade-off of SISO radars (Skolnik, 1980). In particular, a SIMO SAR system opens up an opportunity to set the operational PRF lower than what the unambiguous system dictates and, yet, to keep the effective PRF over Nyquist for higher azimuth resolution. This concept breaks the intrinsic trade-off of conventional SAR.

Chapter 3

Multistatic SAR in Azimuth

A multistatic airborne/spaceborne SAR constellation consists of a set of monostatic and bistatic SARs. Many advantages derive from the bi-/multi-aperture reception, e.g., the potential of flexible observation geometries and multiple coherent parallel acquisition channels. In particular, multistatic constellations offer the opportunity to improve revisit times, access range, image throughput, swath width, or resolution, making it suitable to overcome the challenges of next generation radar remote sensing. Naturally, these advantages come at a cost, namely, an increase in the operational complexity of the system and a more intricate image processing scheme.

One of the most attractive and profitable aspects of employing multiple distinct apertures on receive is to gather redundant information that enables enhanced geometrical resolution in azimuth with an enlarged swath. The early strategies of high-resolution wide-swath (HRWS) imaging, however, appeared mostly in system concepts with a single platform. Griffiths and Mancini proposed to split the receive antenna in across-track and adaptively steer nulls in the antenna pattern (Griffiths and Mancini, 1991). A year later in 1992, Currie and Brown proposed to split the receive antenna in along-track instead with a strict baseline requirement, enabling either azimuth resolution enhancement or a wider swath (Currie and Brown, 1992). Thereafter, Callagan and Longstaff suggested to split the receive antenna in both directions (Callaghan and Longstaff, 1999) as a combination of the first two. After a decade, this simple and direct way of increasing the available information and overcoming the resolution and swath width dilemma, has taken another route towards processing strategies, mainly based on digital beam forming (DBF). The Scan-On-Receive (SCORE) technique first proposed in (Suess and Wiesbeck, 2002b; Suess, Grafmueller, and Zahn, 2001) suggests the splitting of the receive antenna into multiple panels in elevation, i.e. digital beamforming on receive in elevation. An analogous concept for reflector based systems, SweepSAR, was later investigated in (Freeman et al., 2009). Multiple elevation panels make it possible to form a narrow beam that follows the radar echo on the ground. This method ensures continuous maximum antenna gain by pairing the timing of the receiver beam with the reflected pulse along the ground, although it still suffers from blind ranges due to the impossibility of receiving and transmitting simultaneously. In addition, multiple azimuth channels can be used to improve the azimuth resolution and/or to increase the swath width without increasing the PRF (Gebert, 2009). The Staggered SAR concept, where the pulse transmission interval is constantly varied, offers a solution to blind ranges by changing the position of the missing pulses in each transmit/receive cycle (Grafmüller and Schaefer, 2005; Villano, Krieger, and Moreira, 2014). The missing raw data are then recovered via interpolation. Another advanced concept denoted as Virtual Beam Synthesis (Almeida et al., 2018) takes a step further combining the SCORE concept with the varying PRI and multi-channel concept to

improve the azimuth resolution while exploiting ambiguity-free large swath imaging. The staggered SAR concept, however, requires a high azimuth oversampling factor (roughly a factor 2) in order to properly perform the interpolation to recover the missing pulses.

This thesis is built on the HRWS technique proposed in (Krieger, Gebert, and Moreira, 2004b). This may be a more cost-effective and flexible option to overcome the fundamental limitation on joint maximum resolution and swath width typical of conventional SAR (Currie and Brown, 1992; Krieger, Gebert, and Moreira, 2004b). This technique operates the radar with a pulse repetition frequency (PRF) below the Nyquist rate of the single platform, allowing the imaging of large swaths with high resolution. In such a system, since the echoes of the individual receivers appear aliased, the recovery of the unambiguous Doppler spectrum via azimuth reconstruction is required before SAR image formation occurs (Krieger, Gebert, and Moreira, 2004b). The goal of this chapter is to form an adequate background on the geometry and processing of multistatic SAR constellations to evaluate the drawbacks of state-of-the-art reconstruction methods and define the key aspects of a better suited algorithm.

The chapter is divided as follows. Section 3.1 presents the basic concept of multi-aperture reception and the corresponding data model, and introduces state-of-the-art reconstruction methods. Section 3.2 investigates the validity of the reconstruction methods in the literature for along-track multistatic SAR constellations with large baselines. Section 3.3 identifies all essential geometrical aspects for multistatic SAR azimuth reconstruction. Section 3.4 closes the chapter with a short discussion on multistatic SAR, its applications and challenges. The material presented in this Chapter is partially reported in (Sakar et al., 2018; Sakar and Rodriguez-Cassola, 2018; Sakar et al., 2019; Sakar et al., 2020a).

3.1 Overview of High-Resolution Wide-Swath Mode Imaging in Azimuth

3.1.1 Multistatic Along-track Configurations and Signal Model

An along-track multi-aperture SAR (SIMO) system consists of one transmitter and N_{rx} receive antennas. These transmit/receive units are either on a single platform or on separate platforms flying on the same orbit each with an along-track baseline of b_i. As a rule of thumb, all of these receive and transmit units should illuminate the same area on the ground. The additional receive units of single-platform systems can be obtained by splitting the transmit antenna (physically or electronically) in azimuth when receiving. In the multi-platform case, the receive units are equipped with passive radar antennas. Figure 3.1 illustrates these two possible realizations of a multi-aperture SAR concept. [1]

The technique keeps the operational PRF below the Nyquist criterion by a factor called system scaling η_{ss},

$$PRF \geq \frac{B_a}{\eta_{ss}}, \tag{3.1}$$

aiming at relaxing the constraint on the non-ambiguous swath width. The available sampling and the effective sampling of the system are increased by the number of

[1] Note that the use of different orbit heights in the model introduces azimuth-variance, spectral decorrelation, and topography-dependent phase modulations which requires a more elaborate analysis and processing methodology, as discussed in (Rodriguez-Cassola et al., 2013; Pinheiro et al., 2015b).

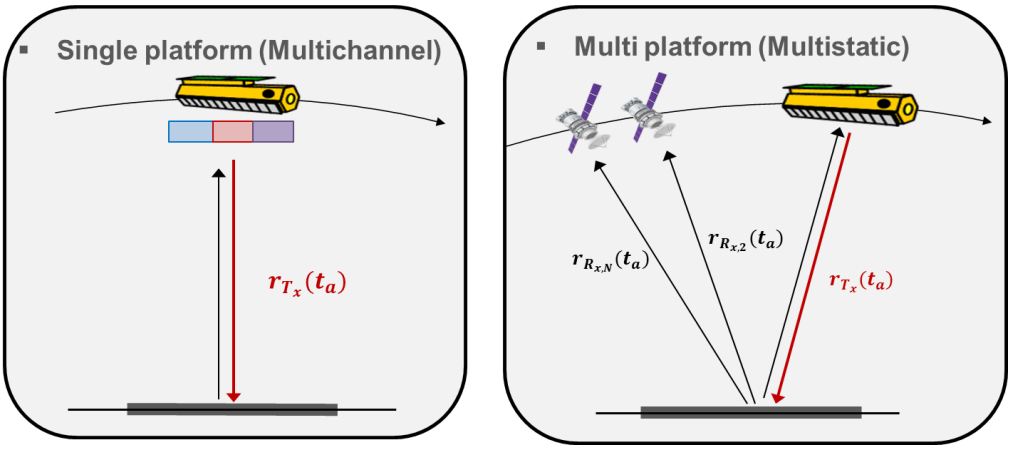

FIGURE 3.1: Multi-aperture SAR system in azimuth: (left) single platform and (right) multi platform.

available satellites $PRF \cdot N_{rx}$ and of the system scaling $PRF \cdot \eta_{ss}$, respectively, where $N_{rx} \geq \eta_{ss}$. Note that depending on the mission concept, the active sensor can be operated in transmit-and-receive mode or solely in transmit mode. Figure 3.2 shows the multi-aperture SAR system block diagram and effective sampling in azimuth for $N_{rx} = \eta_{ss}$. The input data of each receiver are first mixed, digitalized and stored. Depending on the system concept, the data can further be processed either on board or on the ground. In such a system, since the echoes of the individual receivers appear strongly aliased, the recovery of the Doppler spectrum via reconstruction is required to increase the effective sampling before the SAR image formation occurs. Numerous methods for multi-channel/multistatic azimuth reconstruction exist in the literature. In the following sections, some of these methods will be explained and their validity will be evaluated for multistatic constellations with along-track baselines. To establish the necessary background for the rest of this chapter and the thesis, the signal model of multi-aperture systems is derived below.

The azimuth response of the receiver i for a point-like target at azimuth position $t_a = 0$ can be defined as

$$h_i(t_a, b_i; r_0) = w \exp\left[-j\frac{4\pi}{\lambda} r_i(t_a; r_0)\right] \tag{3.2}$$

where w is an amplitude factor including the antenna pattern and the spectral shape of the radar waveform. The range history of each receiver can be expressed as the sum of a reference range history and its deviation from the reference as

$$r_i(t_a, b_i; r_0) = r_{\text{ref}}(t_a - \Delta t_i; r_0) + \Delta r_i(t_a, b_i; r_0), \tag{3.3}$$

where t_a is the azimuth time, Δt_i is the zero-Doppler time difference of the range histories, r_0 is the beam center range, and $r_{\text{ref}}(t_a)$ can be thought of as the common range history of all receivers after signal reconstruction. The polynomial expansion of the reference range can be defined by

$$r_{\text{ref}}(t_a - \Delta t_i) \approx \sum_{n=0}^{N} k_n (t_a - \Delta t_i)^n. \tag{3.4}$$

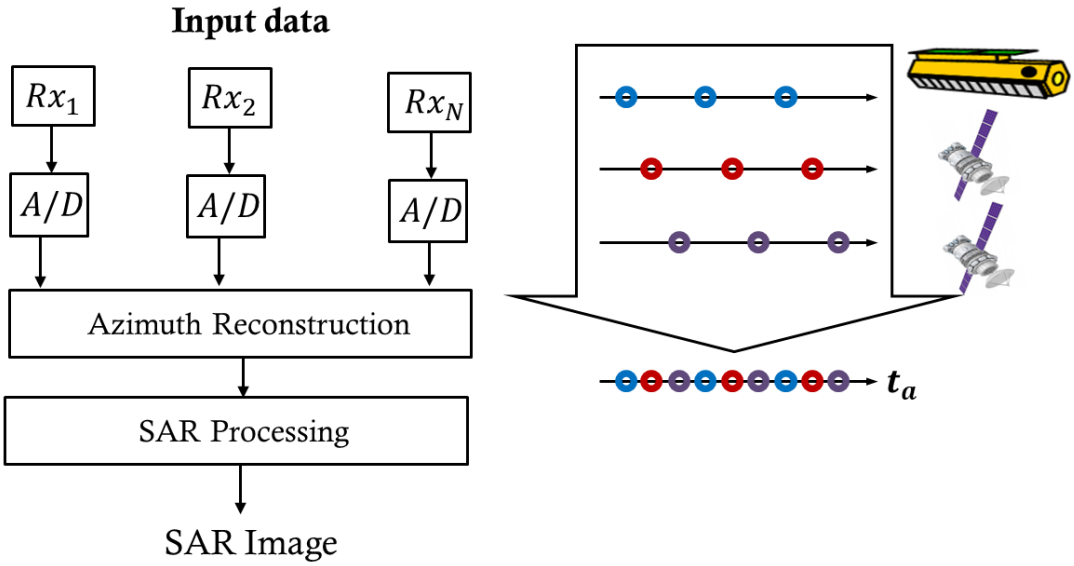

FIGURE 3.2: Multi-aperture SAR system block diagram (left) and effective sampling (right). Note that the effective sampling is determined by the antenna phase centers and operational PRF.

For the purpose of the analysis, the range deviation can be accurately approximated as a quadratic polynomial, i.e.,

$$\Delta r_i(t_a, b_i; r_0) \approx c_0(b_i) + c_1(b_i)t_a + c_2(b_i)t_a^2. \tag{3.5}$$

The estimation error introduced by (3.5) in a typical two-satellite X-band constellation separated by 10 km results in phase deviations well below 1 degree, which validates its accuracy. The performance of this model relies on the fact that the range history equation employs the real orbital geometry and the coefficients are computed numerically. Further analysis on this topic is reported in Subsection 3.3.1. The c_i coefficients show a dependence with the baseline – as explicitly indicated –, but also with r_0 and t_a.

By taking the Fourier transform of the impulse response, the SAR transfer function for receiver i can be approximated as

$$H_i(f_r, f_a) \approx W(f_r, f_a) \exp\left\{-j\left[\Phi_{ref} + \Delta\Phi_i(f_r, f_a)\right]\right\}, \tag{3.6}$$

where f_r and f_a are the range and azimuth frequencies, respectively, $W(f_r, f_a)$ is the Fourier transform of the amplitude factor, Φ_{ref} is the phase of the reference transfer function in the wavenumber domain defined in (2.15) – which will be used after reconstruction – and $\Delta\Phi_i$ is the residual phase term caused by the geometrical difference. This residual phase can be approximated with the series reversion method (Neo, Wong, and Cumming, 2007) and the principle of stationary phase (POSP) as shown below. Inserting Eqs. (3.4) and (3.5) into (3.3), the bistatic range history can be rewritten as

$$r_i(t_a, b_i) = \sum_{n=0}^{N} k_n (t_a - \Delta t_i)^n + \sum_{m=0}^{2} c_m t_a^m. \tag{3.7}$$

By solving Eq. (2.24),

$$-\frac{\mathrm{c}f_{\mathrm{a}}}{f_{\mathrm{r}}+f_0}=\left.\frac{\mathrm{d}r_i(t_{\mathrm{a}})}{\mathrm{d}t_{\mathrm{a}}}\right|_{t_{\mathrm{a}}=t_{\mathrm{a}}^{\star}} =2(k_2+c_2)t_{\mathrm{a}}+3k_3t_{\mathrm{a}}^2, \tag{3.8}$$

the time of stationary phase is obtained as

$$t_{\mathrm{a}}(f_{\mathrm{a}})=\frac{1}{2(k_2+c_2)}-\frac{\mathrm{c}f_{\mathrm{a}}}{f_{\mathrm{r}}+f_0}. \tag{3.9}$$

After inserting $t_{\mathrm{a}}(f_{\mathrm{a}})$ into Eq. (3.2), the phase deviation of the receiver i can be expressed as

$$\begin{aligned}\Delta\Phi_i(f_{\mathrm{r}},f_{\mathrm{a}})\approx -2\pi\Bigg[&\frac{f_0+f_{\mathrm{r}}}{\mathrm{c}}\left(c_0+\frac{k_1^2}{4k_2}-\frac{(k_1+c_1)^2}{4(k_2+c_2)}\right)\\&+\left(\frac{k_2c_1-k_1c_2}{2k_2(k_2+c_2)}\right)f_{\mathrm{a}}-\frac{\mathrm{c}}{f_0+f_{\mathrm{r}}}\left(\frac{c_2}{4k_2(k_2+c_2)}\right)f_{\mathrm{a}}^2\Bigg].\end{aligned} \tag{3.10}$$

For the sake of the simplicity, the set of coefficients in the large parentheses are referred to as C_0, C_1, C_2, respectively. The residual phase can be rewritten as

$$\Delta\Phi_i\approx 2\pi\left(\frac{f_0+f_{\mathrm{r}}}{\mathrm{c}}C_0+C_1f_{\mathrm{a}}+\frac{\mathrm{c}C_2}{f_0+f_{\mathrm{r}}}f_{\mathrm{a}}^2\right). \tag{3.11}$$

By replacing the polynomial coefficients k_i with Doppler parameters ($k_1=\lambda f_{\mathrm{DC}}$ and $k_2=\lambda\beta_{\mathrm{a}}/2$), the coefficients C_i can be expressed by

$$C_0\approx c_0+\frac{\lambda f_{\mathrm{DC}}^2}{2\beta_{\mathrm{a}}}+\frac{(\lambda f_{\mathrm{DC}}+c_1)^2}{2(\lambda\beta_{\mathrm{a}}+2c_2)}, \tag{3.12}$$

$$C_1\approx\frac{\beta_{\mathrm{a}}c_1-2f_{\mathrm{DC}}c_2}{\beta_{\mathrm{a}}(\lambda\beta_{\mathrm{a}}+2c_2)}+\Delta t_i, \tag{3.13}$$

$$C_2\approx\frac{c_2}{\lambda\beta_{\mathrm{a}}(\lambda\beta_{\mathrm{a}}+2c_2)}, \tag{3.14}$$

where f_{DC} and β_{a} are the Doppler centroid and Doppler rate of the reference observation geometry, respectively, and λ is the carrier wavelength. The approximation error of (3.11)-(3.14) is kept well below 1 degree for a two-receiver X-band constellation separated by 10 km and 15λ resolution.

3.1.2 State-of-the-art Reconstruction Methods

Since accurate data processing plays a very crucial role in the success of a multistatic SAR mission, the suitability and validity of the chosen azimuth reconstruction algorithm are critical. Starting in the early 2000s, many multi-channel/cross-platform azimuth reconstruction methods were proposed (Krieger, Gebert, and Moreira, 2004b; Gebert, Krieger, and Moreira, 2009; Cerutti-Maori et al., 2014a; Cerutti-Maori et al., 2014b; Sikaneta, Gierull, and Cerutti-Maori, 2014; Li et al., 2005; Callaghan and Longstaff, 1999; Goodman et al., 2002; Almeida et al., 2018). Two characteristics distinguish these methods: 1) the reconstruction filter computation approach (type

of beamformer), and 2) the domain at which they are applied. Most of the existing literature listed above can be interpreted as weighted variations from the general solution in (Krieger, Gebert, and Moreira, 2004b), if not the same. Note, in addition, that the same beamformer is often referred to by different names in the literature. The filters can be applied either in time or Doppler domain, and they provide similar results in well-conditioned sampling scenarios. However, the Doppler domain reconstruction stands out for regular sampling schemes due to its computational efficiency (multiplication operation), while the time domain reconstruction approach is better suited for irregular sampling schemes despite being computationally more taxing (convolution operation). This section summarizes the reconstruction filter computation methods of the existing literature in the frame of the Doppler domain reconstruction, and $N_{rx} = \eta_{ss}$ is considered, unless stated otherwise. Time domain reconstruction as well as more elaborated Doppler domain reconstruction approaches are discussed in Chapter 4.

As mentioned above, the Displaced Phase Center Approximation (DPCA) reported in (Currie and Brown, 1992) splits the sensor in along-track direction in receive mode and simply interleaves the samples gathered by different sections of the antenna. The system is obliged to move $1/N_{rx}$-th of the antenna length (for N_{rx} channels) between two subsequent transmitted pulses to uniformly sample the received data. This condition imposes a rigid condition on the PRF based on the speed of the platform and the antenna length as

$$PRF = \frac{2v_s}{L_a}, \tag{3.15}$$

which limits the flexibility of the radar system to optimise acquisition and performance. Moreover, in real spaceborne SAR cases, the DPCA is never exactly fulfilled due to the range-variance of both the ground velocity and the bistatic range approximation. As a way to overcome the rigidity of (Currie and Brown, 1992), Krieger *et al.* suggested a reconstruction algorithm in (Krieger, Gebert, and Moreira, 2004b) based on the generalized sampling theory (Papoulis, 1977). The approach can be interpreted as a reconstruction of the non-aliased spectrum (assuming band limitation) by a linear combination of the aliased spectra of the N_{rx} received channels, and corresponds to the Least Mean Square (LMS) estimator of the reconstructed signal under the zero noise assumption (Brown, 1981). The goal of the method is to define and remove the influence of the multistatic system (H_i) from the monostatic SAR impulse response (H_{ref}). The filter function representation that covers the entire signal spectrum ($N_{rx} \cdot PRF$) by shifting the filter functions of each channel by integer multiples of the PRF is

$$H(f_a) = \begin{bmatrix} H_1(f_a) & \dots & H_N(f_a) \\ H_1(f_a + PRF) & \dots & H_N(f_a + PRF) \\ \vdots & \vdots & \vdots \\ H_1(f_a + (N-1)PRF) & \dots & H_N(f_a + (N-1)PRF) \end{bmatrix}. \tag{3.16}$$

For the sake of the compactness, the number of the received channels N_{rx} is replaced by N in Eqs. (3.16) and (3.19). The impulse response function of each receiver H_i is defined as (3.6), where the phase deviation in (Krieger, Gebert, and Moreira, 2004b) can be expressed in the notation of Eq. (3.11) as

$$\widetilde{\Delta\Phi_i} = 2\pi \left[\frac{f_0}{c} C_0(r_0) + C_1(r_0) f_a \right]. \tag{3.17}$$

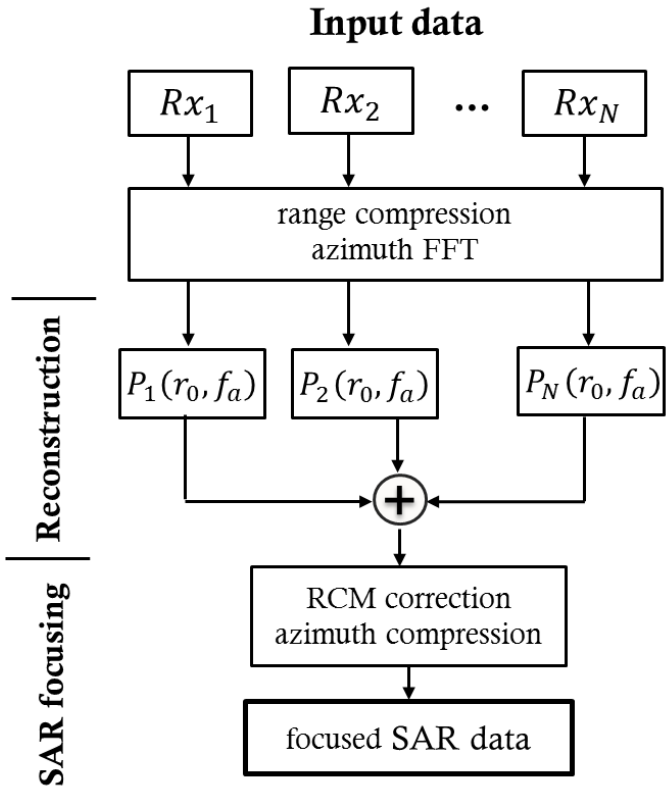

FIGURE 3.3: Block diagram of conventional Doppler-domain reconstruction available in the literature.

The inverse of the filter function is then used to recover the Doppler spectrum:

$$H(f_a)P(f_a) = I_N, \tag{3.18}$$

where I_N is the $N \times N$ identity matrix and the transfer function of the reconstruction filters $P(f_a)$ is

$$P(f_a) = NH^{-1}(f_a) = \begin{bmatrix} P_{11}(f_a) & P_{12}(f_a + PRF) & \dots & P_{1N}(f_a + (N-1)PRF) \\ P_{21}(f_a) & P_{22}(f_a + PRF) & \dots & P_{2N}(f_a + (N-1)PRF) \\ \vdots & \vdots & \vdots & \vdots \\ P_{N1}(f_a) & P_{N2}(f_a + PRF) & \dots & P_{NN}(f_a + (N-1)PRF) \end{bmatrix}. \tag{3.19}$$

It is evident that the direct matrix inversion requires a square-shaped input, however, in case of $N_{rx} \geq \eta_{ss}$, the Doppler bandwidth can be retrieved by Gram-Schmitt orthogonal projection or equivalently using the Moore-Penrose pseudoinverse with

$$P(f_a) = H^{\dagger}(f_a). \tag{3.20}$$

Note that this method is referred to as Multichannel Reconstruction Algorithm in (Gebert, Krieger, and Moreira, 2009), Matrix Inversion Method in (Cerutti-Maori et al., 2014a) and Projection Method in (Sikaneta, Gierull, and Cerutti-Maori, 2014). Figure 3.3 shows the block diagram of the Doppler-based reconstruction algorithms in the literature. The range compressed data from each channel are filtered in the range-Doppler domain with the P_i filters and summed up to suppress azimuth ambiguities in the sub-band. After reconstruction, the data undergo conventional SAR

processing. The main drawback of this method is that the filter matrix may not be invertible for some PRFs due to singularities (when the samples are very close together or coinciding) and the noise-free model includes all of the input data regardless of their ambiguity level, a fact that might reduce the final SNR.

Goodman *et al.* evaluated and compared three beamformers in (Goodman et al., 2002) for sparse spaceborne sensors scattered in both along-track and across-track without specifying the system concept, consequently being a formation type independent beamforming. The first approach called Correlation Filter is simply the weighted conjugate of its measurement vector. This direct method resembles the Multi-channel Phase Correction in Azimuth in (Younis, Venot, and Wiesbeck, 2003) and Maximum Signal Method in (Cerutti-Maori et al., 2014a). It compensates the geometry related phase difference and interleaves the samples, guaranteeing a coherent summation of the signal. However, it does not cancel the ambiguities. In case of a square transfer matrix, then the filter function is equal to (3.18).

The second approach is the Maximum-Likelihood (ML) estimator. The estimator finds the weights that maximize the likelihood function under the assumption of a known conditional probability density function of the input signal with additive Gaussian white noise. The ML weights are computed as

$$w_{ML} = \left[H^H(f_a)R_n^{-1}H^H(f_a)\right]^{-1} H^H(f_a)R_n^{-1} \tag{3.21}$$

where R_n is the noise covariance matrix, defined as $E[nn^H]$. Assuming the noise samples are uncorrelated between channels, the ML estimator becomes again Eq. (3.18).

The third approach, the Minimum Mean-squared Error (MMSE) estimator, computes the filters subject to minimizing the squared estimation error by using the statistical properties of the signals and noise. The filter weights are

$$w_{MMSE} = H^H(f_a)\left[H^H(f_a)H(f_a) + R_n^{-1}(f_a)\right]^{-1} = H^H(f_a)R^{-1}(f_a) \tag{3.22}$$

where R is the covariance matrix of the signal and additive noise. Again the noise-free signal modelling falls back to Eq. (3.18). In (Sikaneta, Gierull, and Cerutti-Maori, 2014), the authors modified the MMSE with a parameter that provides a degree of freedom to choose between optimum ambiguity suppression and optimum noise cancellation. The MMSE then becomes

$$w_{MMSE} = H^H(f_a)\left[H^H(f_a)H(f_a) + \frac{1-q}{q}R_n^{-1}\right]^{-1} \tag{3.23}$$

where $0 \leq q \leq 1$ is a design parameter that represents a compromise between the optimal ambiguity suppression and the noise rejection.

Li *et al.* in (Li et al., 2005) uses a similar approach to the MMSE estimator and computes the weights by using the signal statistical properties with a Minimum Variance Distortionless Response (MVDR), i.e., Capon, beamformer

$$w_{MVDR} = R^{-1}(f_a)H(f_a). \tag{3.24}$$

The beamformer solves the optimization problem with the inverse of the covariance matrix of the signal and additive noise, R, and the filter function. The weights suppress azimuth ambiguities subject to optimizing the SNR with respect to white noise. However, similar as the other beamformers above, the direct matrix inversion method represents a special case of MVDR under the $R_n = 0$ assumption.

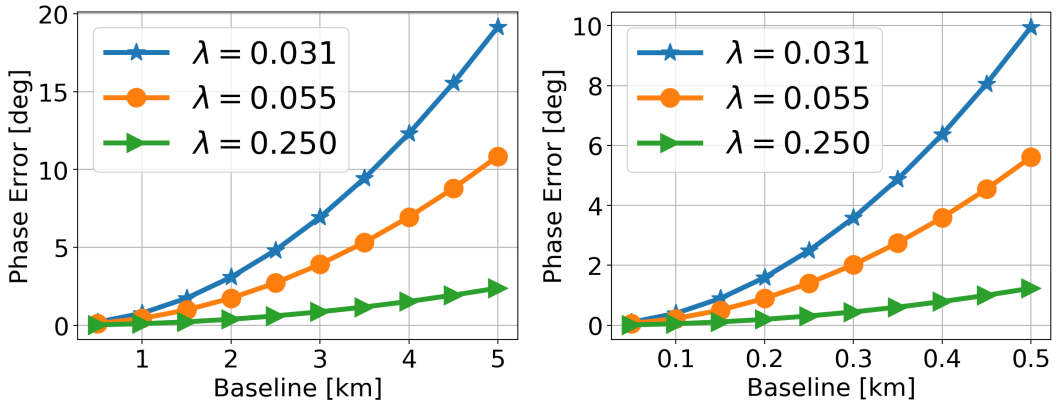

FIGURE 3.4: Contribution to the residual phase error [i.e., (3.11)] due to the change in the Doppler rate (i.e., $c_2 \neq 0$) (left) and to the monochromatic approximation (right) for different along-track baselines and carrier frequencies assuming a resolution of 15λ.

The reconstruction filter estimation (beamformer weight estimation) methods in the literature have been summarized above. It has been shown that the matrix inversion method in (Krieger, Gebert, and Moreira, 2004b) represents a general solution. All other methods in the literature aim at mitigating inversion instabilities in (Krieger, Gebert, and Moreira, 2004b) that arise from noise scaling and sub-optimal sampling schemes. The validity of this family of algorithms is limited to the system concepts meeting the following assumptions: a) azimuth invariance, b) the spectrum of the scene observed by all the channels/platforms is the same, acceptable whenever the shift in the Doppler centroid of the channels remains a fraction of the total azimuth bandwidth of the acquisition, and c) the range histories observed by the different channels are roughly the same. As a direct consequence, the applicability of the existing approaches is confined to small along-track separations of the phase centers, which practically limits their appropriateness to single-platform multi-channel systems.

In distributed systems with along-track baselines of a few kilometers, the changes in the range history introduce strong polychromatic variations which are ignored in the literature listed above. In particular, a residual range-variant polychromatic quadratic component propagates into the reconstruction algorithm causing defocusing and a significant rise of ambiguities. The transfer function and reconstruction approaches reported above consider the range variance but neglect the polychromatic nature of the radar echoes and the change of the Doppler rate for increasing along-track baselines [see Eq. 3.17]. The importance of polychromatic azimuth reconstruction is addressed in (Cerutti-Maori et al., 2014b), where the authors expressed the polychromatic transfer function analogous to the Eqs. (3.11) and (3.17) as

$$\widetilde{\Delta\Phi_i} = 2\pi \left(\frac{f_0 + f_\mathrm{r}}{\mathrm{c}} C_0(r_{0,\mathrm{ref}}) + C_1(r_{0,\mathrm{ref}}) f_\mathrm{a} \right) , \tag{3.25}$$

which accommodates the range bandwidth but ignores the range variance and the change in the Doppler rate for increasing baselines. Figure 3.4 shows the contribution to the phase error due to the change in the Doppler rate (left) and due to the monochromatic approximation (right) as a function of the baseline for X-, C- and L-band systems with a geometric resolution equal to 15λ. They both become relevant for along-track baselines in the order of kilometers. The system parameters used

TABLE 3.1: System parameters used in the different simulations

Wavelength [m]	0.031 / 0.055 / 0.25
PRF [kHz]	8.8 / 4.9 / 1.1
Transmitted BW [MHz]	370 / 209 / 46
Number of Rx	2
Slant range [km]	700
Velocity [m/s]	7100
Oversampling [%]	15

in the simulations are listed in Table 3.1. Note that the generated data have been slightly oversampled to facilitate the interpretation of the results. The next subsection investigates the impact of such approximations, which limit the validity of the existing algorithms to along-track baselines smaller than a few hundred meters and to geometrical resolutions coarser than 15λ.

3.2 Error Analysis

In this section, an expression of the 2D error of the reconstructed signal due to the different imaging geometry of each receiver is presented. This expression is derived for a two-receiver constellation, clearly a best case scenario. The addition of more receivers, besides complicating the math and the intelligibility of the results, will in general only make the system more sensitive to approximations. In particular, an increased number of phase jumps in the reconstructed spectrum appear, hence degrading the performance of the ambiguity suppression.

The spectrum of the scene is modeled as the band-limited signal $S(f_\mathrm{r}, f_\mathrm{a})$, and common for all channels, a standard assumption of all signal reconstruction methods (Currie and Brown, 1992; Krieger, Gebert, and Moreira, 2004b; Cerutti-Maori et al., 2014a; Sikaneta, Gierull, and Cerutti-Maori, 2014).[2] Following the notation in (Krieger, Gebert, and Moreira, 2004b), the different channels are modeled using a linear filter with the transfer function H_i after which the signals are sampled at a rate (PRF) about N_{rx} times below the Nyquist frequency of the single platform. The reconstruction of the signal is achieved by summation of the filtered aliased echoes of the individual receivers. In the j-th sub-band, the reconstructed signal is expressed as

$$S_j(f_\mathrm{r}, f_\mathrm{a}) = \sum_{i=1}^{N} P_{ij}(f_\mathrm{r}, f_\mathrm{a}; b_i) S_{i,\mathrm{a}}(f_\mathrm{r}, f_\mathrm{a}), \tag{3.26}$$

where $P_{ij}(f_\mathrm{r}, f_\mathrm{a})$ is the transfer function of the reconstruction filter for receiver i and $S_{i,\mathrm{a}}(f_\mathrm{r}, f_\mathrm{a})$ is the spectrum of the aliased received signal. Depending on the optimization methodology (type of the beamformer), the shape of the reconstruction filters P_{ij} varies.

In order to isolate the impact of the geometric approximations, a two-receiver constellation with approximate uniform sampling, i.e., beam-center positions equidistant in space is chosen. Note that this is only a methodological assumption to improve the intelligibility of the analysis and not a requirement imposed on the

[2] Depending on the extent of the baseline, the bistatic observation geometry introduces an instantaneous Doppler shift between the channels, which may result in a non-common Doppler support (see Subsection 3.3.5).

multistatic constellation. This scenario, a transmit/receive satellite followed by a receive-only satellite at a distance b_2, not only represents – as already hinted – a best case, but also helps us to separate the purely geometrical errors from the noise scaling introduced by sampling non-uniformity (Krieger, Gebert, and Moreira, 2004b). The data from the first receiver roughly contain one half of the samples of the monostatic Nyquist-sampled signal, whereas the data from the second receiver contain the remaining interleaving half which incorporates a residual migration due to the different observation geometry. Following the methodology in (Krieger, Gebert, and Moreira, 2004b), the reconstructed data in both sub-bands are

$$\widetilde{S}_1 = \frac{1}{2}\{S^+\left[1-\exp(-\mathrm{j}\delta\Delta\Phi_2^+)\right] + S\left[1+\exp(-\mathrm{j}\delta\Delta\Phi_2)\right]\}, \tag{3.27}$$

$$\widetilde{S}_2 = \frac{1}{2}\{S^-\left[1-\exp(-\mathrm{j}\delta\Delta\Phi_2^-)\right] + S\left[1+\exp(-\mathrm{j}\delta\Delta\Phi_2)\right]\}, \tag{3.28}$$

where $\delta\Delta\Phi_2$ is the difference between the true phase deviation defined in (3.11) and the one used in the reconstruction, $\delta\Delta\Phi_2^{\pm} = \delta\Delta\Phi_2(f_\mathrm{r}, f_\mathrm{a} \pm \mathrm{PRF})$, and $S^{\pm} = S(f_\mathrm{r}, f_\mathrm{a} \pm \mathrm{PRF})$.

The error between two different reconstruction algorithms can be expressed as

$$\epsilon(f_\mathrm{r}, f_\mathrm{a}) = S(f_\mathrm{r}, f_\mathrm{a}) - \widetilde{S}(f_\mathrm{r}, f_\mathrm{a}). \tag{3.29}$$

Inserting (3.27) and (3.28) into (3.29), the error in the reconstructed sub-bands becomes

$$\epsilon_1 = S^+\mathrm{j}\sin\left(\frac{\delta\Delta\Phi_2^+}{2}\right)\exp\left(-\mathrm{j}\frac{\delta\Delta\Phi_2^+}{2}\right) - S\mathrm{j}\sin\left(\frac{\delta\Delta\Phi_2}{2}\right)\exp\left(-\mathrm{j}\frac{\delta\Delta\Phi_2}{2}\right), \tag{3.30}$$

$$\epsilon_2 = S^-\mathrm{j}\sin\left(\frac{\delta\Delta\Phi_2^-}{2}\right)\exp\left(-\mathrm{j}\frac{\delta\Delta\Phi_2^-}{2}\right) - S\mathrm{j}\sin\left(\frac{\delta\Delta\Phi_2}{2}\right)\exp\left(-\mathrm{j}\frac{\delta\Delta\Phi_2}{2}\right). \tag{3.31}$$

In the next subsections, the impact of the different Doppler rates and the monochromatic approximation used in state-of-the-art reconstruction algorithms are analysed.

3.2.1 Uncompensated Doppler Rate Error

The error caused by an uncompensated Doppler rate change is proportional to the quadratic component of (3.11), i.e.,

$$\delta\Delta\Phi \approx 2\pi\lambda C_2(r_0) f_\mathrm{a}^2. \tag{3.32}$$

Figure 3.5 shows the impact of (3.32) on the reconstruction of a point target in the reference X-band scenario of Table 3.1 for 15λ resolution and $b_2 = 7$ km. The two top plots show the phase error (in degree) after reconstruction in the 2D wavenumber domain (left) and the zero frequency cut (right), showing a jumping quadratic behaviour. The corresponding impulse response is shown in the bottom left plot. As expected, the quadratic component introduces visible defocusing while the jumps degrade the ambiguity suppression (not shown in Figure 3.5). The bottom-right plot of Figure 3.5 shows the expected phase error introduced by the mismatch in the reconstruction as a function of the along-track baseline for the X-, C-, and L-band cases. Setting a quality threshold at 15 degrees, the maximum along-track baseline separation is limited to about 5 km for the X-band case.

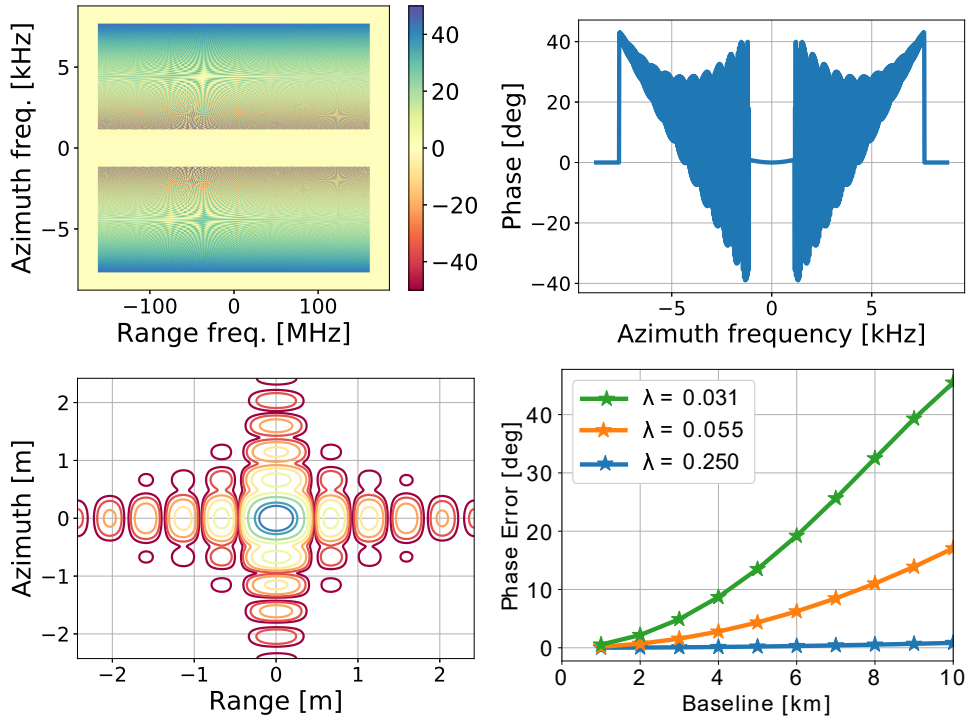

FIGURE 3.5: Reconstruction errors caused by uncompensated residual Doppler rate. (Top left) Phase error (in degree) in the wavenumber domain, (top right) azimuth cut at the center of the band, (bottom left) impulse response, all for an X-band, 15λ resolution system with $b_2 = 7$ km. The bottom right plot shows the phase error as a function of the along-track baseline for the scenarios listed in Table 3.1.

As discussed earlier, an increase in the number of receivers increases the number of phase jumps between sub-bands and thus degrades the reconstruction performance even further. Figure 3.6 compares the performance of two and six-receiver constellations in terms of phase error (top), ambiguities (bottom left) and defocusing (bottom right). The conditions of the simulation are analogous to those of Figure 3.5, X-band with 15λ resolution and $b_i = 7 + i\Delta b$ km, with Δb roughly about 1 m. As argued above, the increased number of phase jumps within the band, noticeable in the top right figure, generates additional ambiguities and results in a slight defocusing.

3.2.2 Monochromatic Reconstruction Error

The error caused by the monochromatic reconstruction in the range-Doppler domain is proportional to (Sakar et al., 2018)

$$\delta\Delta\Phi \approx 2\pi f_r \left[\frac{C_0(r_0)}{c} + \frac{cC_2(r_0)}{f_0^2} f_a^2\right]. \tag{3.33}$$

This error description is valid for (Krieger, Gebert, and Moreira, 2004b) assuming small along-track baselines. Figure 3.7 shows the impact of a monochromatic reconstruction on a two receiver X-band constellation separated by 800 m and with 15λ resolution, with analogous distribution as in Figure 3.5. No defocusing in azimuth is visible, a shift in range of the impulse response is evident (top right, bottom left), and the reconstruction errors (bottom right) are noticeable for baselines shorter than 1 km.

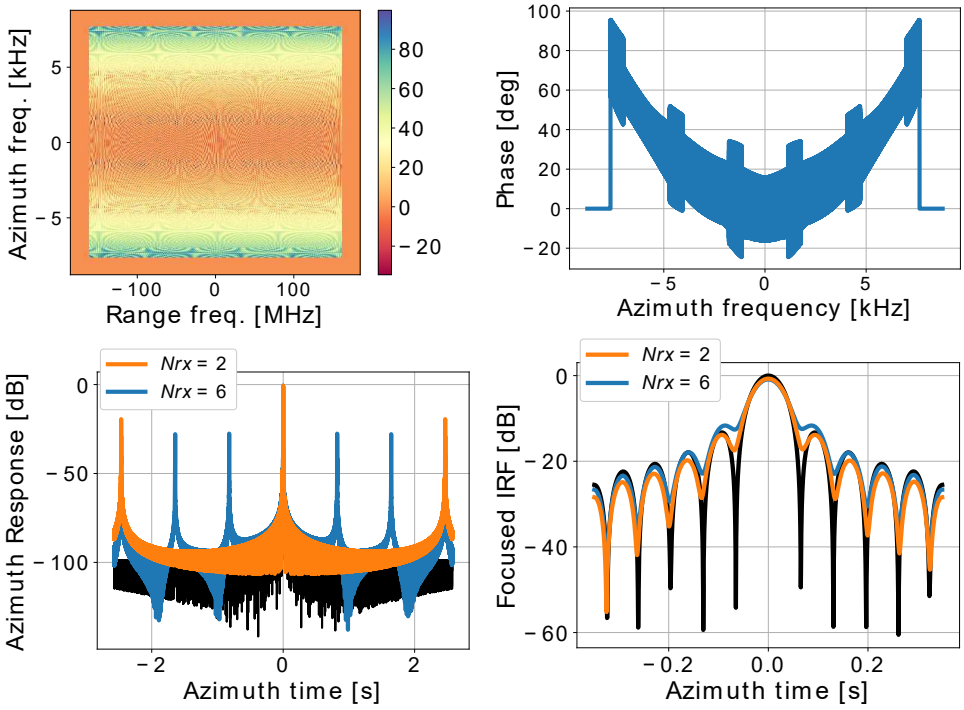

FIGURE 3.6: Comparison of reconstruction errors for two and six receiver X-band constellations, with baselines of about 7 km between the transmitter and the receive channels and resolution of 15λ. (Top left) Phase error (in degree) in the wavenumber domain, (top right) phase error at the center of the band. (Bottom left) Azimuth ambiguities and (bottom right) azimuth impulse response. The black curves on the bottom plots represent reference monostatic impulse response functions.

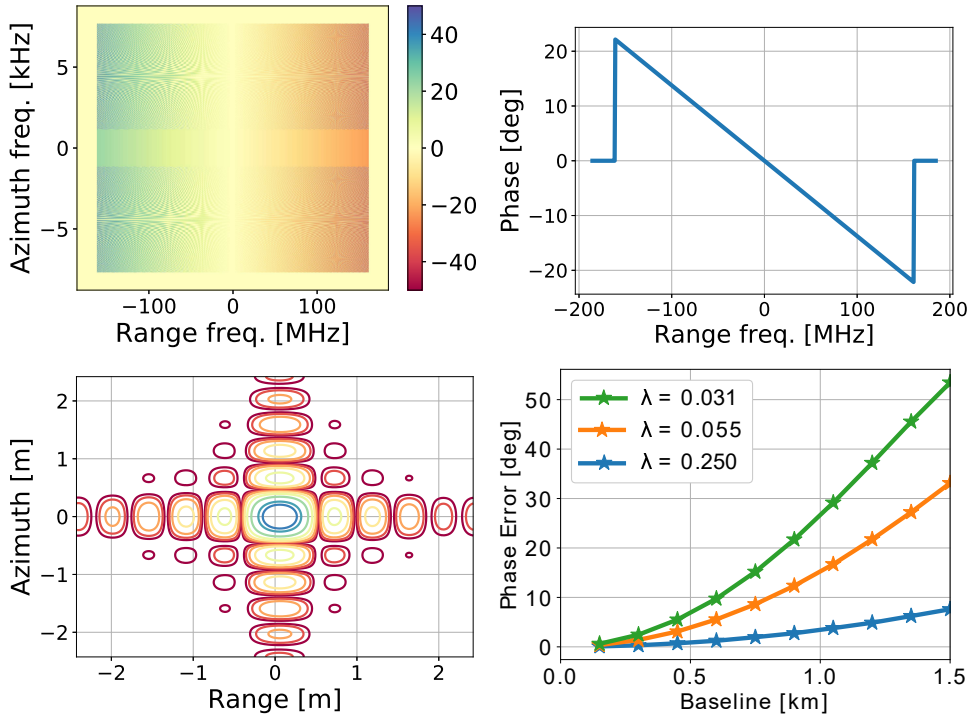

FIGURE 3.7: Errors caused by a monochromatic reconstruction. (Top left) Phase error (in degree) in the wavenumber domain, (top right) range cut at the center of the band, (bottom left) impulse response, all for an X-band, 15λ resolution system with $b_2 = 800$ m. The bottom right plot shows the phase error as a function of the along-track baseline for the scenarios listed in Table 3.1.

3.2.3 Range-Invariant Polychromatic Reconstruction Error

The proposed approach in (Cerutti-Maori et al., 2014b) describes a polychromatic reconstruction algorithm which neglects the changes in the Doppler rate and the range variance. Under these conditions, the phase error is proportional to (Sakar et al., 2018)

$$\delta\Delta\Phi \approx 2\pi \left(\frac{f_0 + f_\mathrm{r}}{\mathrm{c}} \delta C_0 + \delta C_1 f_\mathrm{a} + \frac{\mathrm{c}\delta C_2}{f_0 + f_\mathrm{r}} f_\mathrm{a}^2 \right), \tag{3.34}$$

where the $\delta C_i = C_i(r_0) - C_i(r_{0,\mathrm{ref}})$. Figure 3.8 shows the error of the polychromatic range-invariant reconstruction on the simulation case of Figure 3.7, for a target placed 20 km away from the reference range used in the reconstruction, i.e., $\Delta r_\mathrm{g} = 20$ km.

Most of the residual shift of Figure 3.7 is corrected, but significant phase errors (bottom right) within 10 km swaths already appear for baselines of about 1 km.

3.3 Key Geometrical Aspects of Azimuth Reconstruction

Section 3.2 established the necessary framework to investigate the validity of state-of-the-art reconstruction algorithms for multistatic SAR constellations with along-track baselines in a simplified scenario under the linear orbit assumption. The reconstruction error expressions derived in (Sakar et al., 2018) allow for the analytical computation of the error without having to simulate the actual reconstruction.

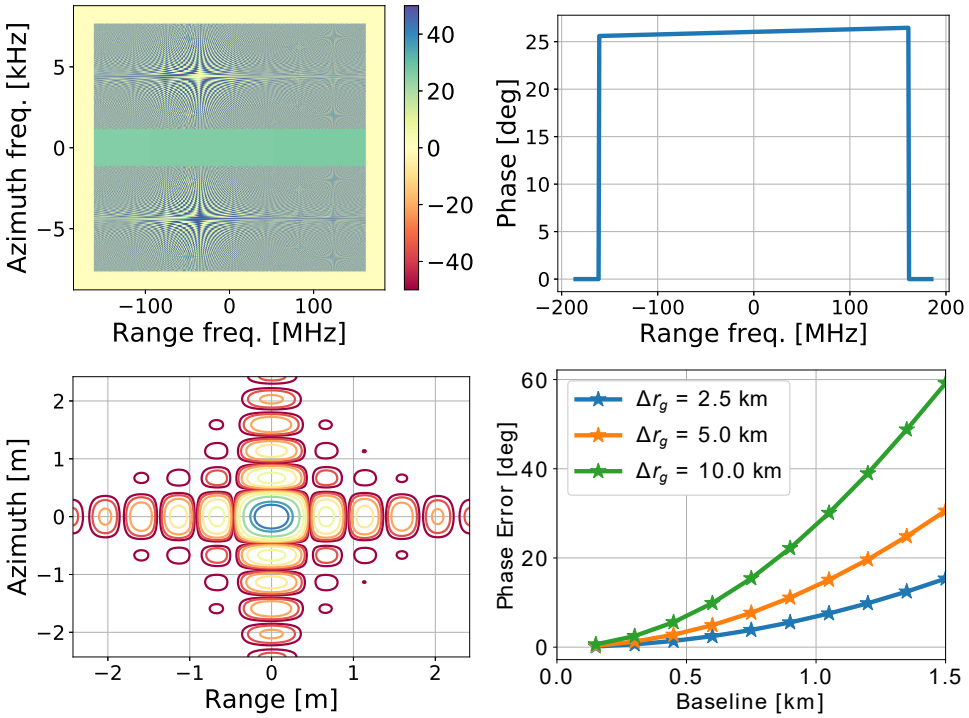

FIGURE 3.8: Errors caused by a range-invariant polychromatic reconstruction. (Top left) Phase error (in degree) in the wavenumber domain, (top right) range cut at the center of the band, (bottom left) impulse response, all for an X-band, 15λ resolution system with $b_2 = 800$ m. The target is placed 20 km away from the reference used for the polychromatic reconstruction. The bottom right plot shows the phase error as a function of the along-track baseline for targets located at different distances Δr_g of the reference.

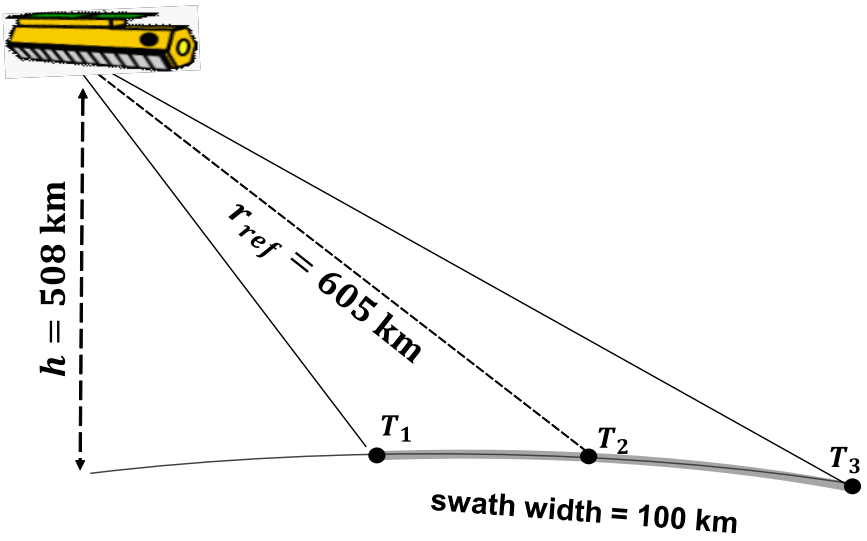

FIGURE 3.9: The reference orbit and observation geometry, with a reference swath of 100 km and a mean incidence angle of about 33°, used for the simulations.

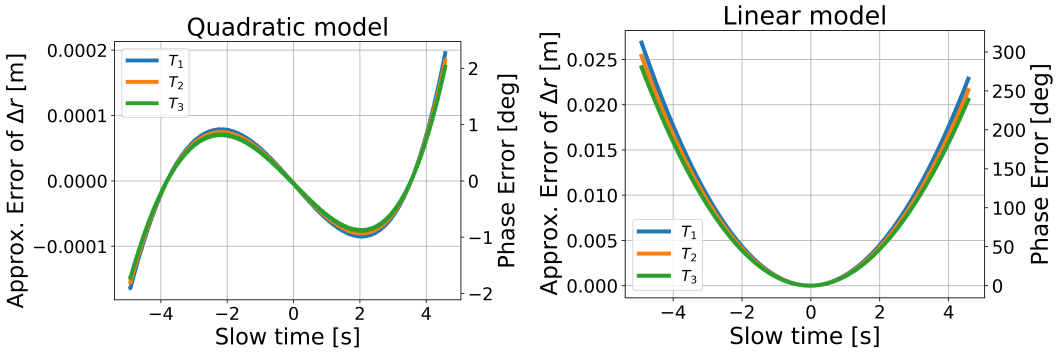

FIGURE 3.10: Error in the approximation of the deviation of the range history (and corresponding phase error in degrees) for (top) the quadratic model in (3.5) and (bottom) the linear model typically used in the literature for a two-receiver X-band constellation with 15λ azimuth resolution and 5 km along-track separation. The three curves correspond to targets in near, mid, and far ranges as shown in Figure 3.9. Note the different scales of the error in the two models.

Building on the outcomes of the error analysis reported above, this section identifies all geometric aspects that need to be considered for multistatic SAR constellations, especially with large along-track baselines and very high resolutions. To obtain simulation results as close as possible to real mission scenarios, the orbit and observation geometry shown in Figure 3.9 are used for the simulations of this section, which are based on the TerraSAR-X case.

3.3.1 Range History Deviation

As discussed in Subsection 3.1.1, the range history deviation of each receiver from the reference range history can be approximated numerically by a quadratic polynomial. As a demonstration of the accuracy of (3.5), Figure 3.10 (left) shows the error in the approximation (in range and in phase) for an X-band two-receiver constellation with an along-track baseline of 5 km. In this example, an integration time of 10 s and an orbital geometry have been considered. The error in the approximation of (3.5) results in phase deviations smaller than 2°. The right plot shows the error of

the approximation using a linear polynomial, which reaches values in the order of the wavelength, and corroborates the pertinence of the quadratic model.

3.3.2 Polychromatic Transfer Function

The modelling of the transfer function of any receiver of a multistatic constellation can be expressed in terms of the transfer function of a reference sensor of the constellation and a residual phase term $\Delta\Phi_i$ which accounts for the differential range histories between the reference and receiver i, i.e., Δr_i. As already mentioned, $\Delta\Phi_i$ can be well approximated by a quadratic polynomial.

In order to illustrate the errors introduced by the monochromatic and the range-invariant approximations, Figure 3.11 shows the dependence of $\Delta\Phi_i$ with slant range (left) and range frequency (right) for a two-spacecraft X-band constellation with 15λ resolution and an along-track baseline of one kilometer.

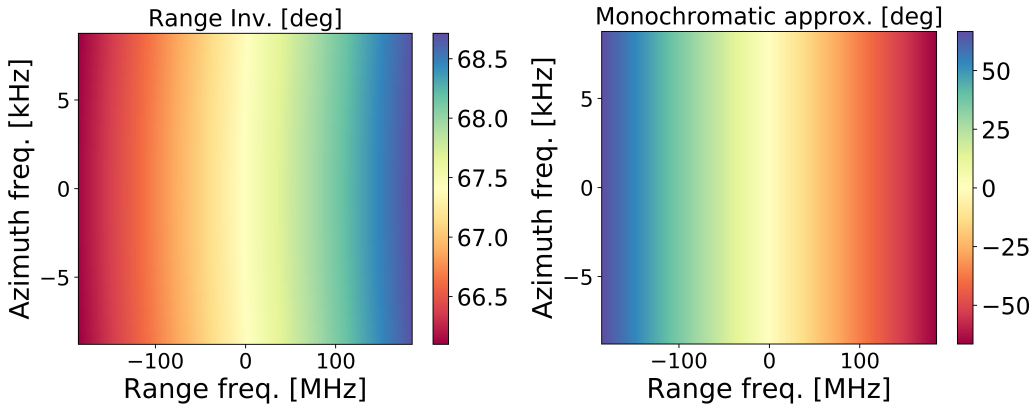

FIGURE 3.11: The left figure shows the difference in $\Delta\Phi_i$ between two targets located at near and mid range (T_1 and T_2 in Figure 3.9). The plot is computed as $\Delta\Phi_i\left[f_r, f_a; r_0(T_1), b_i\right] - \Delta\Phi_i\left[f_r, f_a; r_0(T_2), b_i\right]$ and used to illustrate the contributions of the range variance in the modelling of the distributed sampling. The right figure shows the difference in $\Delta\Phi_i$ due to the monochromatic approximation for the target located at the center of the swath (i.e., T_2) and is computed as $\Delta\Phi_i\left[f_r, f_a; r_0(T_2), b_i\right] - \Delta\Phi_i\left[0, f_a; r_0(T_2), b_i\right]$. The plots have been generated for a two-receiver X-band constellation with an along-track baseline of one kilometer and 15λ azimuth and range resolution.

Even with these moderate figures, variations in $\Delta\Phi_i$ reach values around 60° at the edges of the band within a 100 kilometer swath and about 130° due to the polychromatic contributions. It is therefore important to stress that the reconstruction algorithms available in the literature fail to accommodate both the range variance and the polychromatic nature simultaneously.

3.3.3 Range Cell Migration

In order to avoid large errors caused by aliasing, range cell migration correction occurs after azimuth reconstruction. Consequently, the reconstruction filters P_i (applied in the range-Doppler domain) need to match the range cell migration of the data, which poses a problem of both accuracy and efficiency. The top of Figure 3.12 shows the distribution of the range cell migration of one target in the aliased data. The bottom of Figure 3.12 shows the resulting deformation of the reconstruction filters matching the range cell migration of the data. Note it is not possible to match the full range cell migration of the data within an output sub-band, which results in a residual phase error intrinsic to reconstruction schemes in the Fourier domain.

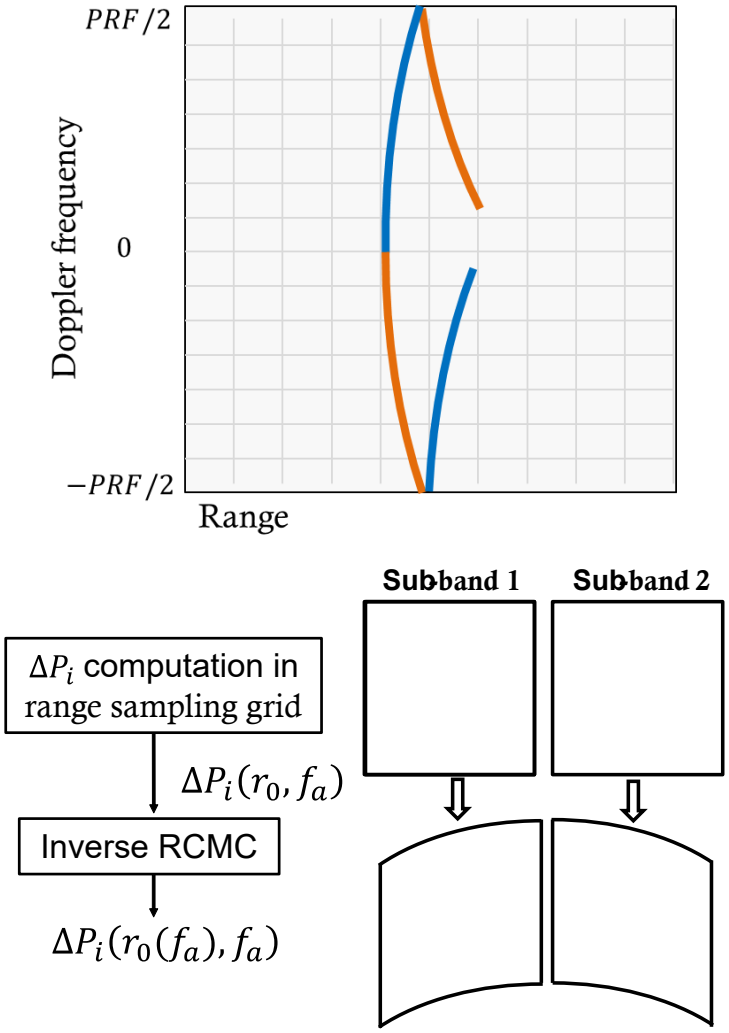

FIGURE 3.12: The top figure illustrates the shape of the range cell migration in the range-Doppler domain in the undersampled data for a two-receiver constellation. The blue and orange parts correspond to the spectral components reconstructed in sub-bands 1 and 2, respectively. The bottom figure shows the deformation of the reconstruction filters P_i required to match the range cell migration of the data.

The problem of efficiency is due to the burden involved in the direct numerical computation of the P_i on the 2D range-Doppler grid $(r_0(f_a), f_a)$. A possible way to solve this consists of computing the P_i for the nominal values of (r_0, f_a) and then interpolating the P_i for each Doppler frequency according to the range cell migration of the data. This process can be interpreted as an interpolation-based inverse RCMC on the reconstruction filters (not on the data).

3.3.4 Orbit Control

Orbit control is an imperative and challenging mission aspect for multi-platform constellations. The position of the elements of the multistatic constellation plays a fundamental role in the feasibility of the data reconstruction and the successful retrieval of the unambiguous Doppler bandwidth and consequent suppression of azimuth ambiguities. Deviations in the along-track position of the spacecraft may result in ill-conditioned sampling. Deviations in across-track may result in time- and range-variant reconstruction errors which can be interpreted as a topography-dependent model mismatch.

Independent of the number of elements in the constellation, controlling the along-track position of the receivers within one resolution period of the reconstructed signal ensures the absence of coinciding samples. This condition can be expressed as a requirement on the control of the along-track position of the spacecraft as

$$\delta t_{\text{atrack}} < \zeta \frac{v_g}{v_{\text{sat}} N_{\text{rx}} B_a} = \zeta \frac{\beta_{\text{res}} \lambda}{v_{\text{sat}} N_{\text{rx}}}, \tag{3.35}$$

where v_g is the ground velocity, v_{sat} is the spacecraft velocity, N_{rx} is the number of receivers in the constellation, λ is the carrier wavelength, B_a is the reconstructed Doppler bandwidth, and ζ is a design factor strictly smaller than one, and ideally smaller than 0.5; the second equation relates the resulting azimuth resolution with the carrier wavelength by introducing the auxiliary parameter β_{res} which will be referred to in the following as resolution index. This identification is pertinent since the accuracy required in processing and reconstruction for different frequencies is inversely proportional to this factor. Figure 3.13 shows Eq. (3.35) – scaled in m with the spacecraft velocity – as a function of β_{res} for different carrier frequencies. As

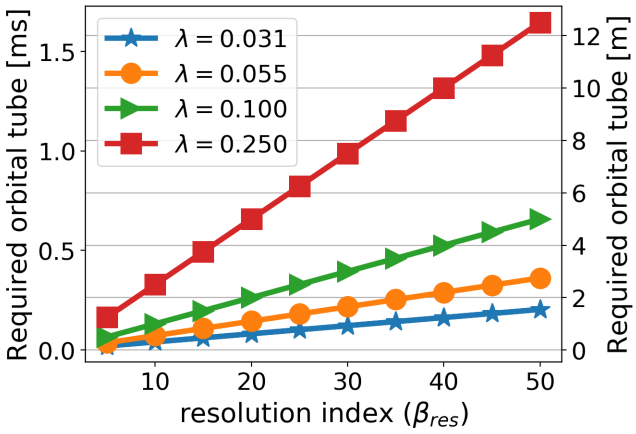

FIGURE 3.13: Orbit control sensitivity of X-, C-, S- and L-band SAR systems: required orbit control accuracy in along-track with respect to azimuth resolution of $\delta_{\text{az}} = \beta_{res}\lambda$, given both in milliseconds and meters.

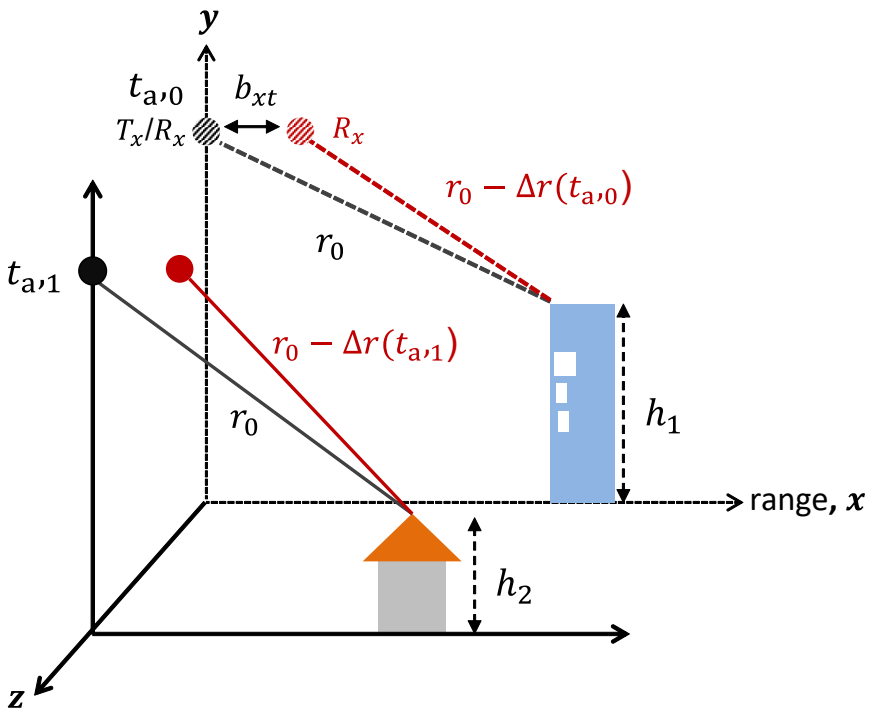

FIGURE 3.14: Illustration of azimuth variant topography-dependent model mismatch due to the across-track baseline. Note that $\Delta r(t_{a,0}) \neq \Delta r(t_{a,1})$. Two targets are placed at different heights and have identical closest monostatic ranges, but different bistatic ranges.

expected, this requirement becomes more stringent for higher frequencies and better resolutions.

In across-track, the limitation is imposed by the topographic gradients within the footprint, since topography imposes an inherent model mismatch in the reconstruction process. Figure 3.14 illustrates the azimuth-variant range deviation depending on the height of the targets, where the model mismatch is caused by the height difference of each point with respect to the reference point (used to compute reconstruction weights). The maximum phase error caused by the model mismatch can be approximated as

$$\epsilon_\phi \approx \frac{2\pi \delta r_{\text{xtrack}} \delta h}{2\lambda \sin \theta_{\text{i}}}, \tag{3.36}$$

where θ_{i} is the incidence angle, and δh is the maximum topographic gradient – in azimuth, actually – within the transmit footprint. Figure 3.15 shows the impact of b_{xt} in terms of ϵ_ϕ, which results in azimuth ambiguities for different carrier frequencies with respect to δh. Analogously to the along-track case, the requirement on the orbital tube becomes more stringent for higher frequencies and also for larger N_{rx}. Orbit control requirements and their implications are further discussed in Chapter 5.

3.3.5 Common Doppler Bandwidth

An essential requirement for the full recovery of the Doppler bandwidth is that the spectrum of the scene observed by all platforms is the same. Another implication of the bistatic observation geometry is, however, the instantaneous frequency deviation. The instantaneous frequency of a monostatic/bistatic survey is given by

$$f_{\text{a,i}} = \frac{1}{\lambda} \frac{\partial r_i(t_{\text{a}})}{\partial t_{\text{a}}} \approx f_{DC,i} + \beta_{a,i\text{a}}. \tag{3.37}$$

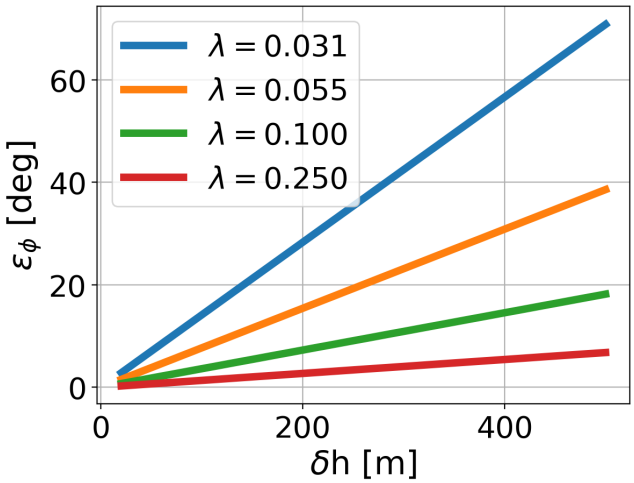

FIGURE 3.15: Orbit control sensitivity of X-, C-, S- and L-band SAR systems: phase error caused by the model mismatch due to $b_{xt} = 5$ m in two-receiver constellation for different carrier frequencies with respect to δh.

Assuming zero-squint, the Doppler rate deviation of a bistatic survey with respect to a reference is equal to $c_2(b_i)$ in Eq. (3.5) and the Doppler centroid deviation is given by

$$\Delta f_{DC,i} = \frac{\Delta t_i v_s^2}{\lambda \sqrt{r_{ref}^2 + v_s^2 \Delta t_i^2}} - \frac{c_1(b_i)}{\lambda}. \tag{3.38}$$

which represents the instantaneous Doppler shift between the monostatic and bistatic SAR acquisitions. An along-track baseline of 5 km in an X-band system with the observation geometry shown in Figure 3.9 results in an instantaneous Doppler shift of 1.9 kHz.

Figure 3.16 illustrates the impact of Δf_{DC} on the reconstruction of the aliased Doppler spectrum assuming band-limitation. In this reconstruction example, a simple two-receiver constellation with one active and one passive sensor is considered. The top-left plot shows the aliased spectrum of the monostatic receiver with zero Doppler centroid (red), and the bottom one shows the spectrum of bistatic survey with $|f_{DC,2}| > 0$ (green). Note that in both cases, a slight oversampling has been added to the triangular shape representation of the spectrum. The grey stripes over the aliased spectrum highlight the non-common Doppler bins between the two receivers. This mismatch of the observed scene spectrum leads to partially recovered spectrum shown on the right (yellow), which consequently results in reconstruction errors. Since unresolved Doppler bins appear both at the center and edges of the spectrum (grey stripes), filtering outside of the processed bandwidth cannot circumvent the reconstruction error. However, the Doppler spectrum of a SAR signal is typically not band-limited due to the sidelobes of the joint antenna pattern, which becomes helpful to handle the shift in f_{DC}. Therefore, the Doppler centroid shift imposed by the bistatic geometry is manageable whenever it remains a fraction of the total azimuth bandwidth of the acquisition.

3.3.6 Atmospheric Effect

Another range delay factor which needs to be addressed is the atmosphere. The round trip travel time of each chirp is delayed by the tropospheric and ionospheric

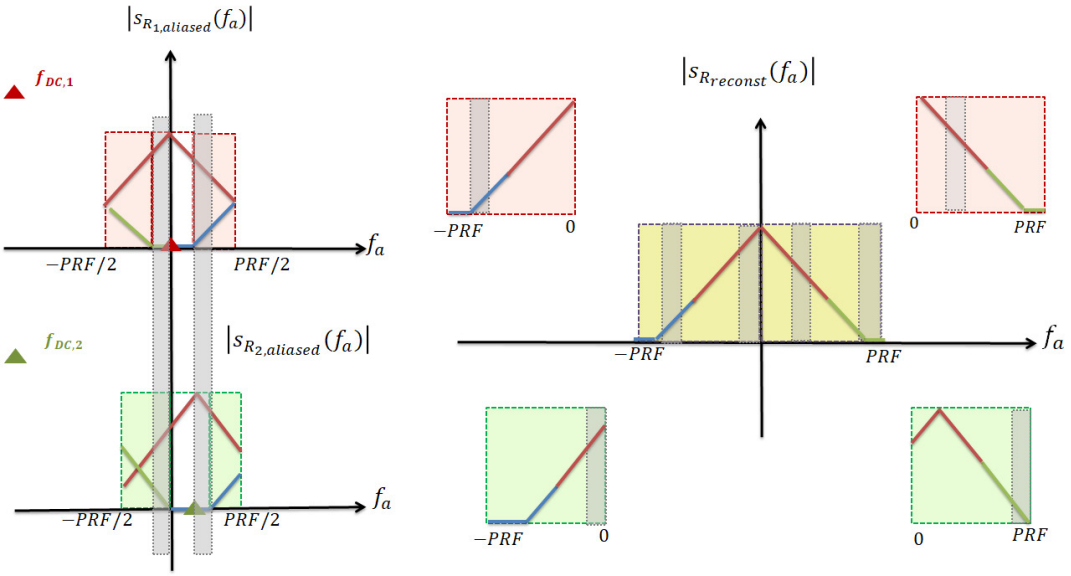

FIGURE 3.16: The recovery of the full Doppler bandwidth may be impossible due to the difference in bandwidth support of each receiver. The illustration of the unrecoverable frequency bins (grey stripes) in a two-receiver multistatic SAR scenario.

layers. The ionosphere causes a frequency dependent (dispersive) phase advance and group delay, whereas the troposphere causes a non-dispersive phase and group delay. Figure 3.17 shows the atmospheric layers and possible range delays for a two-receiver multi-channel constellation.

The atmospheric delays that each receiver of a constellation experiences may differ due to the geometrical differences and thus causes additional range and phase variations. The atmospheric phase delay difference between the receive units must be addressed before the reconstruction.

The tropospheric delays can be classified as hydrostatic (large) and wet (small). The hydrostatic delay is caused by dry gases in the atmosphere, can be modeled with the altitude and pressure knowledge, and is about 2.3 m at the sea level. The wet delay is caused by the precipitable water vapour and may cause up to 40 cm delay. The total tropospheric delay is computed as

$$\Delta r_{trop}(t_a, r_0) = \frac{z \exp[-h(r_{ref})/H]}{\cos(\theta_i(r_0)) \cos(\theta_a(t_a, r_0))} \tag{3.39}$$

where z is a constant zenith path delay in meters, H is a reference height and h is the altitude of the target.

The ionospheric delay of a monostatic sensor is given by

$$\Delta r_{ion}(t_a, r_0) = \frac{40.28\,\mathrm{m^3 s^{-2}}}{f_r^2} \frac{VTEC}{\cos(\theta_i(r_0)) \cos\theta_a(t_a, r_0))} \tag{3.40}$$

where $VTEC$ is the number of electrons in a vertical cylinder and typical values are 5-10 TECU (Total Electron Content Units, 10^{16}). As an example, this average value results in roughly 5.3 cm delay in TerraSAR-X. Note that the individual and total atmospheric delays within the synthetic aperture are the weighted version of the zenith delays, which can be expressed as

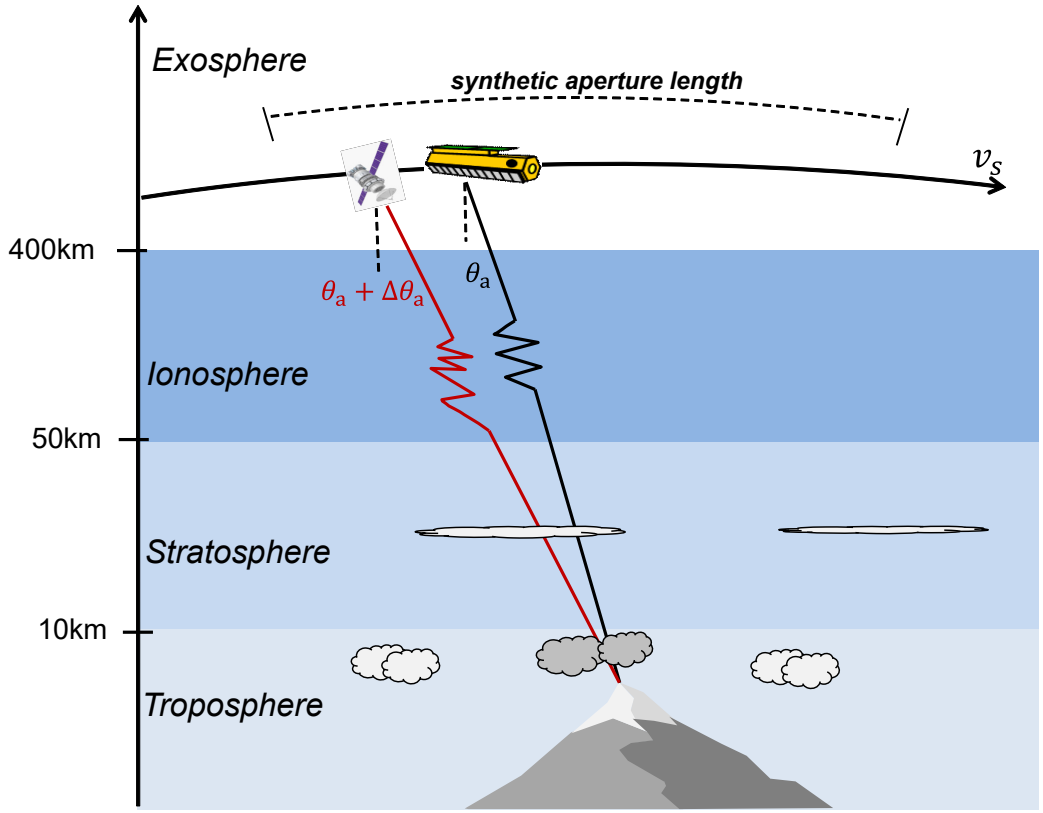

FIGURE 3.17: Illustration of the atmospheric layers and range delays in the ionosphere and troposphere.

$$\Delta r_{atm}(t_a, r_0) = \frac{\Delta r_{ion,zenith} + \Delta r_{trop,zenith}}{\cos(\theta_i(r_0))\cos(\theta_a(t_a, r_0))}. \tag{3.41}$$

The left plot of Figure 3.18 shows the delta atmospheric delay and its corresponding phase error for monostatic and bistatic surveys for a 10 km baseline and a 8λ resolution at X-band. The simulation parameters of both plots are shown in Table 3.2.

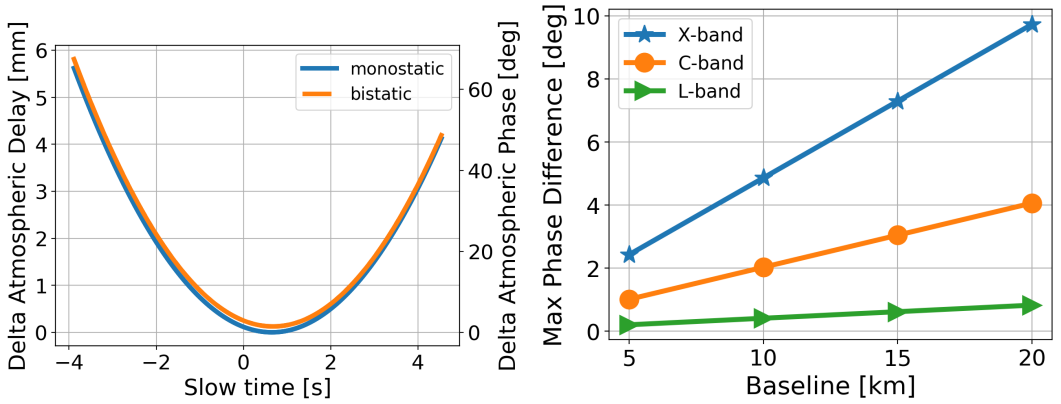

FIGURE 3.18: Left: Delta atmospheric delay and corresponding phase after subtracting the reference offset at zero Doppler for monostatic and bistatic signal. Right: Maximum atmospheric phase deviation of the bistatic survey from a reference (monostatic) with respect to along-track baseline for different carrier frequencies.

TABLE 3.2: Atmospheric delay simulation parameters

Wavelength [m]	0.031 / 0.055 / 0.25
Orbit height [km]	514 / 693 / 745
Target height [km]	0
VTEC [TECU]	10 / 40 / 50
Slant range [km]	547 / 738 / 793

The plot shows the variation of the phase error within the synthetic aperture due to the aperture angle change. As shown in (Prats-Iraola et al., 2014), for very high-resolution systems it is imperative to correct for this error to avoid azimuth defocusing and phase errors. Regarding the reconstruction of the multistatic SAR acquisition, the differential range delay between receivers, i.e., the difference of the monostatic and the bistatic phase in Figure 3.18, is of interest. In an optimal configuration, the incidence angle is the same for all the receivers (no across-track baseline). If the incidence angles of the receivers are different, the across-track baselines in the order of few meters translate to negligible $\Delta\theta_i$ values, i.e., $\Delta\theta_i \approx b_{xt}/r_0 \approx 5 \cdot 10^{-6}$. The actual atmospheric delay difference is caused by the large kilometric along-track baselines, which change the aperture angle of the receivers $\Delta\theta_a$ for each receiver. By following the analogy in (Krieger et al., 2014), the differential range delay due to b_i is given by

$$\frac{\partial \Delta r_{atm}}{\partial \cos(\theta_a)} \approx \Delta r_{atm} \tan(\theta_a) \Delta\theta_a \tag{3.42}$$

where the differential aperture angle is

$$\Delta\theta_a = \tan^{-1}\left(\frac{b_i/2}{r_0}\right) \approx \frac{b_i/2}{r_0}. \tag{3.43}$$

The right plot of Figure 3.18 shows the maximum atmospheric phase difference with respect to the along-track baseline for different carrier frequencies. It is clear that this phase difference becomes relevant for high-resolution systems with large along-track baselines. Despite its magnitude, this phase difference should be addressed prior to the reconstruction to avoid azimuth ambiguities and shifts in azimuth. Note that the simulation has only considered an homogeneous atmosphere, and therefore additional phase errors may occur in more realistic cases.

3.4 Conclusion

This chapter introduced the multi-channel/multistatic SAR concept in azimuth which allows for a high-resolution and wide-swath mode simultaneously. An accurate data model that represents both single- and multi-platform realizations has been derived and its accuracy has been verified. After a brief summary of the state-of-the-art reconstruction algorithms, the impact of the along-track baseline on the accuracy of current signal reconstruction methods for multistatic along-track SAR constellations have been investigated. In scenarios with baselines in the order of kilometers, the difference in the range histories seen by the receivers introduces reconstruction errors visible for resolutions better than 15λ, even for small swaths. In the second part of the chapter, all important geometrical aspects that need to be considered for an accurate reconstruction have been identified and their effects analysed. This

chapter established a profound understanding of the complex bistatic acquisition geometry and its implications on accurate reconstruction approaches, which forms the basis of the processing algorithms discussed in Chapter 4.

Chapter 4

Azimuth Reconstruction Algorithms for Multistatic SAR Formations

In Chapter 3, standard approximations of state-of-the-art reconstruction algorithms have been investigated and shown that they lead to defocusing and to a significant degradation in the suppression of ambiguities in multistatic along-track constellations. Moreover, the impact of those approximations worsens for orbital geometries, hence, the reconstruction coefficients should be preferably computed numerically. The geometrical approximations in the literature often include neglecting the polychromatic nature of the data (coupling between Doppler and range frequencies) and the change of the Doppler rate for the different receivers (lack of quadratic component), which have been shown to introduce significant reconstruction mismatch and raise azimuth ambiguities for increasing along-track baselines. For the sake of establishing a common background, the phase errors due to these two approximations are shown in Figure 4.1 for a two-receiver constellation and different carrier frequencies in curved orbit geometry (see Section 3.3 for the same plots with the linear orbit assumption). For short along-track baselines and moderate resolutions, the consequences of these approximations are negligible. The system parameters used in these simulations are listed in Table 3.1 on page 38 and the observation geometry is illustrated in Figure 3.9. For the analysed cases, the monochromatic assumption [Figure 4.1 left] holds for along-track baselines of definitely less than one kilometer, whereas the linear assumption in Eq. (3.17) [Figure 4.1 right] breaks down for

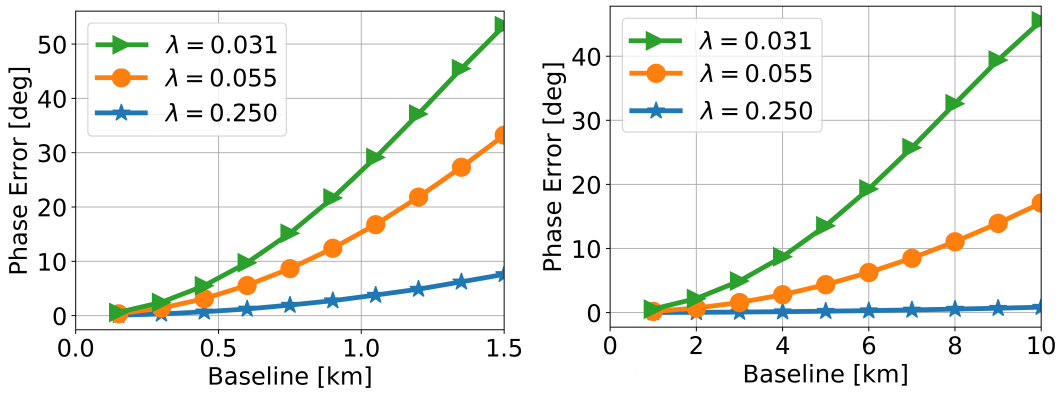

FIGURE 4.1: Phase errors (in degrees) as a function of the along-track baseline caused by a monochromatic reconstruction (left) and the model in (3.17) (right) in a two-receiver system with 15λ azimuth resolution.

along-track baselines larger than a few (e.g., less than four) kilometers. These results suggest that the applicability of the existing approaches is confined to along-track separations up to hundreds of meters and to geometric resolutions coarser than 15λ. Furthermore, in distributed systems with along-track baselines of a few kilometers, the changes in the range history introduce relevant polychromatic errors ignored in the available literature.[1] In particular, a residual range-variant polychromatic quadratic component propagates into the reconstruction algorithm causing defocusing and raise of azimuth ambiguities. The importance of the polychromatic reconstruction for very high-resolution multi-channel (single platform) SAR systems is pointed out in (Cerutti-Maori et al., 2014b), a reference which lacks a consolidated flow addressing the range variance of the reconstruction process (see Figure 3.11), limiting its validity in practical terms for swaths of a few (e.g., less than five) kilometers.

The goal of this chapter is to report accurate and efficient reconstruction strategies for multistatic along-track constellations, valid over large swaths, for large along-track baselines and very high resolution. The reconstruction approaches and their validity are fundamental in providing realistic values for the performance analysis. The geometrical aspects of the azimuth reconstruction that are explicitly incorporated in the current solutions are: i) the range history deviation between receiving channels is modeled as a quadratic polynomial, ii) the range-variance and the polychromatic character of the reconstruction filters are accommodated in a very accurate manner, including the fit of the reconstruction filters to the range cell migration of the data. The two-step reconstruction approaches presented in this chapter are based on the error analysis and investigations reported in Chapter 3. The new algorithms incorporate residual polychromatic corrections which achieve accurate reconstruction for constellations with kilometric baselines over swaths of hundreds of kilometers. The reconstruction can be done either in Doppler or in time domains. It will be later discussed in this section that both provide similar results in well-conditioned sampling scenarios, with the Doppler-domain being more efficient but only suited for regular sampling schemes, while the time-domain can cope with irregular ones.

This chapter is structured as follows. Section 4.1 presents a generalized range-Doppler strategy which can be used for the correction of most geometrical approximations of the current approaches under the assumption of azimuth invariance. The validity of the method is investigated and compared with the algorithms available in the literature. Section 4.2 presents two time-domain reconstruction strategies based on the accurate data model that are capable of accommodating the range-frequency dependence. Both Doppler-domain and time-domain reconstruction methods are driven pursuant to the data model presented in Subsection 3.1.1. Section 4.3 compares the Doppler- and time-domain approaches, and Section 4.4 finally closes the chapter with a discussion.

4.1 Doppler-Domain Reconstruction Algorithm

This section introduces a two-step range-Doppler strategy – which can employ any of the filter weights introduced in Subsection 3.1.2 – capable of accommodating changes in the Doppler rates, the range-variance of the reconstruction filters, and a bulk polychromatic component. The algorithm is inspired in the accurate version of the SAR image formation range-Doppler algorithm as described in (Bamler, Meyer,

[1] Polychromatic corrections are typically required whenever there is a strong coupling between Doppler and range frequencies.

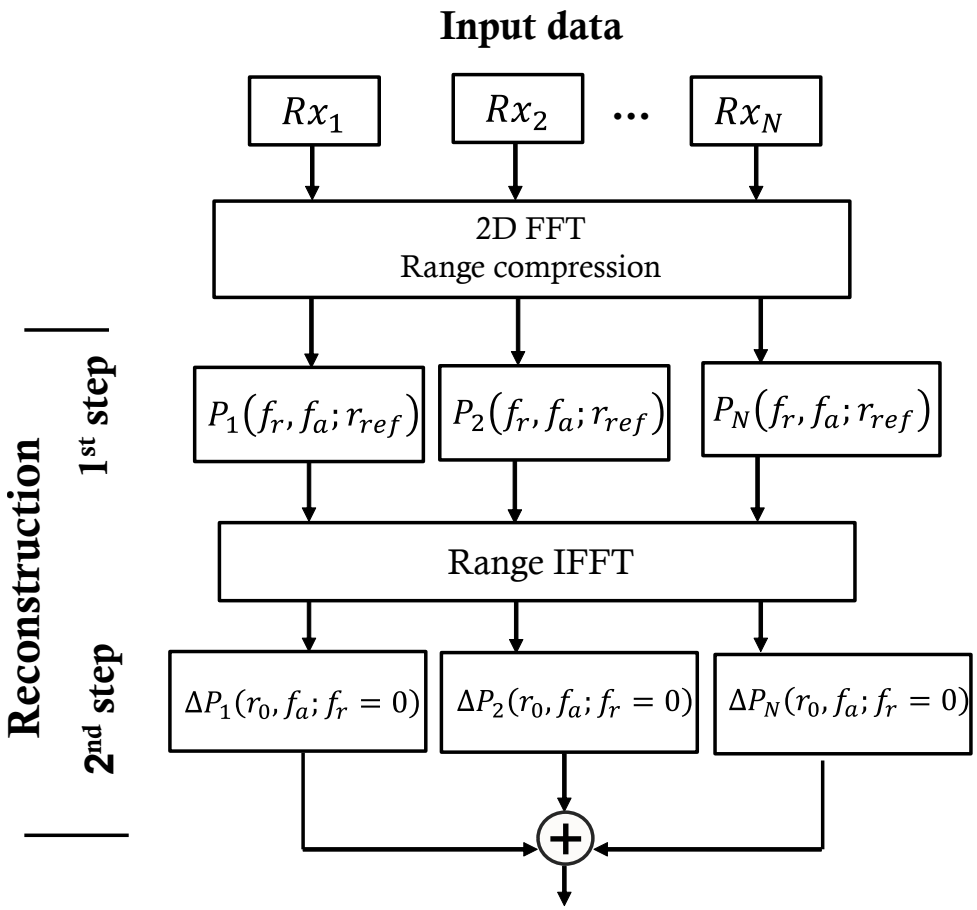

FIGURE 4.2: Block diagram of the two-step Doppler domain reconstruction algorithm. Note that the input data are brought to 2D frequency domain before range compression, since the first step of the reconstruction is done in wavenumber domain.

and Liebhart, 2007), only improving the efficiency of the numerical generation of the processing functions.

To accommodate simultaneously the range-variant and polychromatic nature of the azimuth reconstruction, a two-step strategy, which is an idea originally presented in (Sakar et al., 2018) as a conclusion of the analysis, is proposed. The filter weights, P_i, are approximated as the cascade of two filters [see (4.1)]: 1) a polychromatic bulk part applied in the wavenumber domain and computed for a reference range (e.g., center of the swath) and, 2) a range-variant polychromatic part applied in the range-Doppler domain to compensate for the residual components of the reconstruction filters as given by (4.2)-(4.4). Figure 4.2 shows the block diagram of the proposed reconstruction algorithm.

After the input raw data are brought to the wavenumber domain (2D FFT) and are range compressed, the data of the receive channels go through the bulk reconstruction filter in the wavenumber domain (1st step of the reconstruction) and are then brought back to the range-Doppler domain. The range-variant differential reconstruction filters are updated for every range bin and matched to the range cell migration of the data as discussed in Subsection 3.3.3 (2nd step of the reconstruction). After filtering, the data of all receive channels are added up to form the reconstructed sub-band. The suggested two-step approach can be mathematically described as the factorisation of the reconstruction filters

$$P_i \approx P_i(f_r, f_a; r_{ref}) \Delta P_i(f_r, f_a; r_0(f_a)), \tag{4.1}$$

where r_{ref} corresponds to a target at the center of the swath (T_2 in Figure 3.9), and ΔP_i is computed as

$$\Delta P_i = \left| \frac{P_i(0, f_a; r_0)}{P_i(0, f_a; r_{ref})} \right| \exp\left[j \Delta\varphi_i(f_r, f_a; r_0) \right], \tag{4.2}$$

where the phase of the differential reconstruction filter is expressed as

$$\begin{aligned} \Delta\varphi_i(f_r, f_a; r_0) = &\left[\varphi_i(0, f_a; r_0) - \varphi_i(0, f_a; r_{ref}) \right] \\ &+ \Delta\varphi_{i,resi}(f_r, f_a; r_0), \end{aligned} \tag{4.3}$$

where $\varphi_i(\cdot)$ is the phase of P_i and $\Delta\varphi_{i,resi}$ is a polychromatic residual phase term. Note that the use of the different reconstruction methods falls back to the use of different P_i and the suggested strategy is hence not linked to any specific approach in the literature.

By setting $\Delta\varphi_{i,resi} = 0$ in (4.3), Figure 4.3 compares the performance of the two-step algorithm for the simulations presented in Figures 3.6, 3.7, 3.8 computed with the same analytical model shown in Eqs. (3.30) and (3.31). The phase error is significantly reduced in all cases and kept below 1 deg in most of them, which extends the range of validity of range-Doppler reconstruction techniques for swaths of tens and even hundreds of kilometers and baselines a factor four to five larger than the approaches in the literature. Nevertheless, the contribution of $\Delta\varphi_{i,resi}$ becomes significant for increasing along-track baselines and swaths.

4.1.1 Residual Correction: Derivation of $\Delta\varphi_{i,resi}$

The analysis with the linear orbit assumption has already revealed that the initial version of the two-step reconstruction falls short for very high-resolution systems with hundreds of km of swath. Figure 4.4 shows the phase error as a function of the along-track baseline for different swath widths in a two-receiver X-band constellation with 15λ resolution with a curved orbit. This plot represents a comparison to the performance plots of the literature shown in Figure 4.1.

Setting a quality threshold at 15°, a reasonable value for ensuring an acceptable quality of IRF, the maximum along-track baseline separation is limited to less than 3 km for 100 km swath width. Figure 4.5 shows the residual phase of the reconstruction filter, i.e., Eq. (4.3) considering $\Delta\varphi_{i,resi} = 0$, for the upper limit scenario of 3 km baseline and 100 km swath width. The left plot shows that this phase has a linear shape in range frequency and it is nearly constant in the Doppler domain. The right plot shows that the phase also changes linearly in slant range. This linear variation of the residual phase suggests that one can approximate $\Delta\varphi_{i,resi}$ as

$$\Delta\varphi_{i,resi}(f_r, f_a; r_0) \approx 2\pi f_r \delta t_r(r_0; f_a), \tag{4.4}$$

where $\delta t_r(r_0; f_a)$ describes a range-variant shift which results in a stretching of the filtered data. This stretching can be efficiently corrected by means of a range interpolation in the range-Doppler domain. After removal of the expression in (4.4) from the data, Figure 4.6 shows that the residual phase error has practically disappeared. Figure 4.7 shows the second step of the reconstruction consisting of: i) a differential

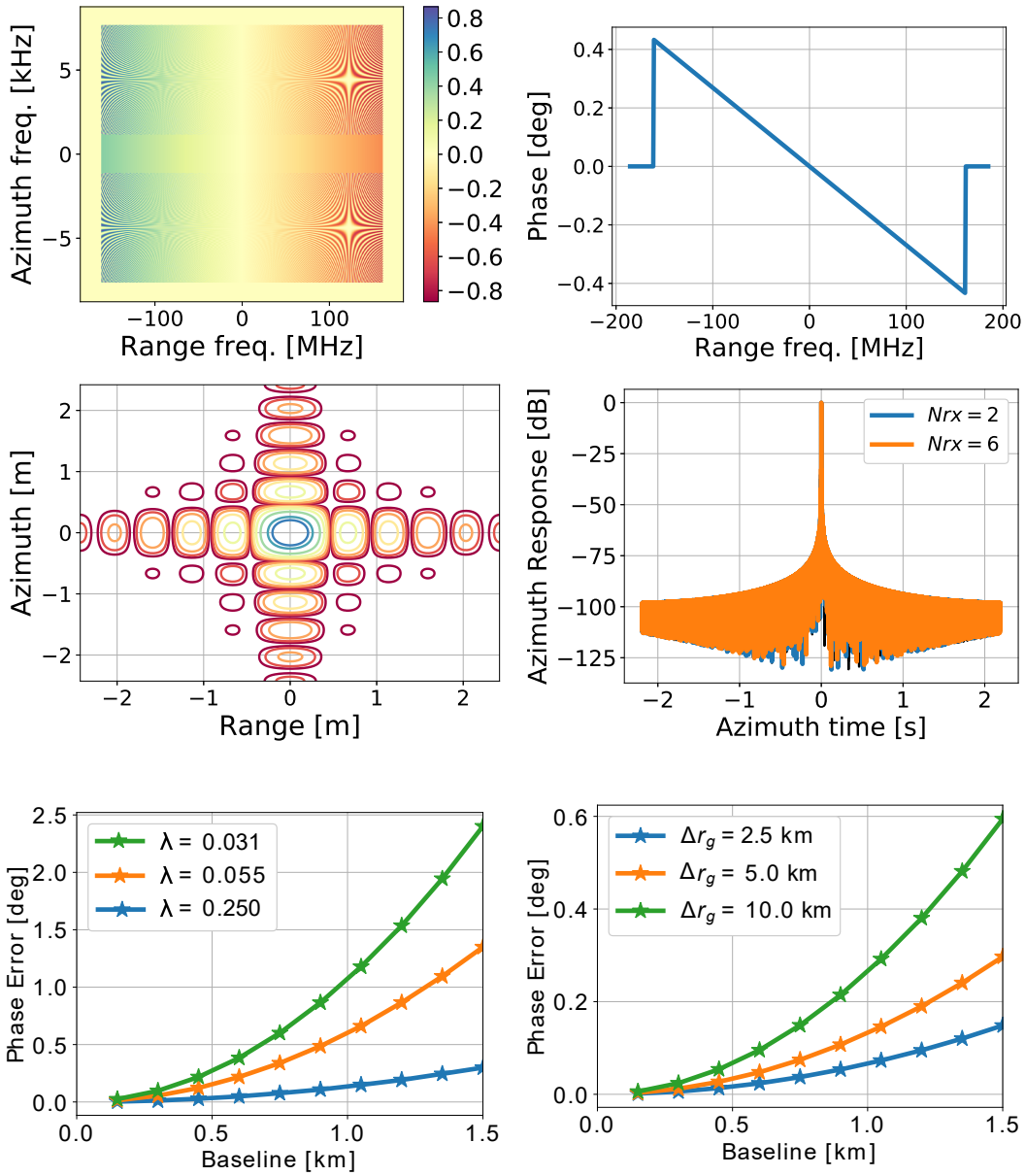

FIGURE 4.3: Errors after using the generalized two-step range-Doppler reconstruction suggested in (Sakar et al., 2018). The simulations correspond to the ones conducted for Figures 3.6, 3.7, 3.8, respectively. In all cases, the phase error (in degree) is reduced by more than one order of magnitude with respect to state-of-the-art approaches.

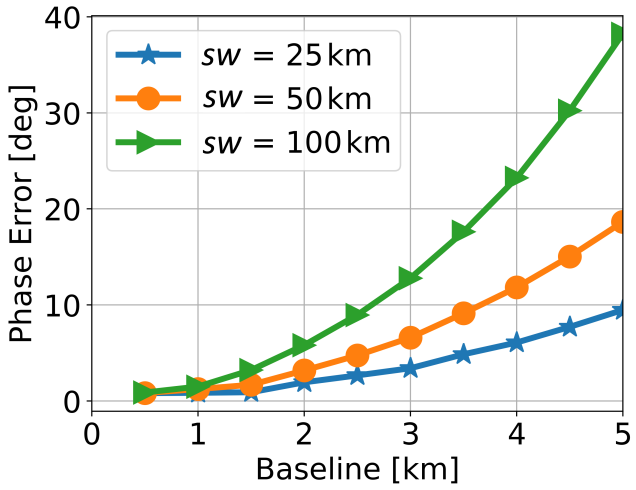

FIGURE 4.4: Phase error caused by the reconstruction method in (Sakar et al., 2018) (i.e., $\Delta\varphi_{i,\text{resi}} = 0$) for a two-receiver X-band constellation with 15λ resolution and swath widths of 25, 50 and 100 kilometers, respectively.

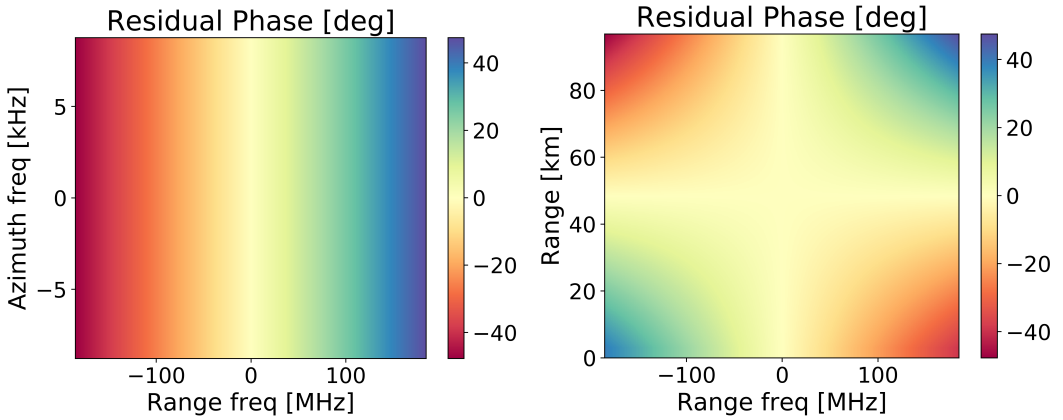

FIGURE 4.5: Residual phase after removal of the monochromatic part of Eq. (4.3) for the simulation scenario of Figure 4.11 (left) in the wavenumber domain for a near range target and (right) in the range-range frequency domain for $f_\text{a} = 0$.

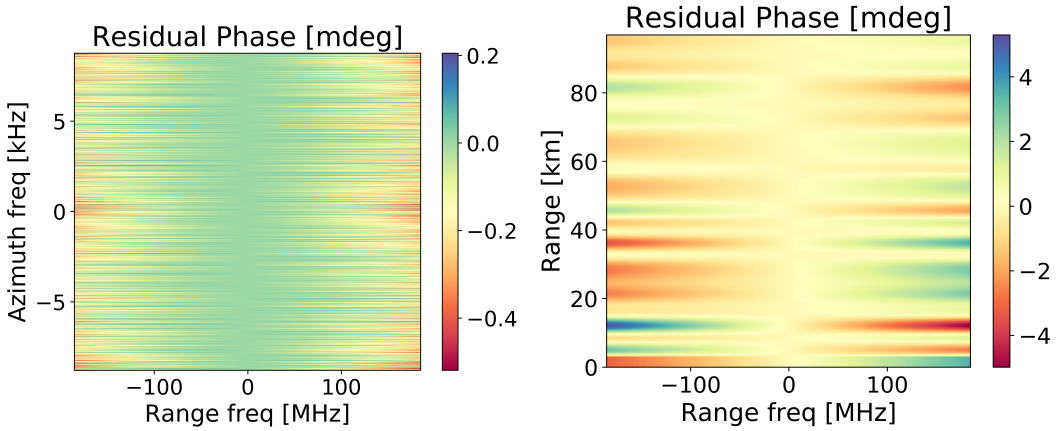

FIGURE 4.6: Residual phase after correction of (4.4) for the simulation scenario of Figure 4.11. The left plot shows the residual phase in the wavenumber domain for a near range target. The right plot shows residual phase in the range-range frequency domain for $f_\text{a} = 0$.

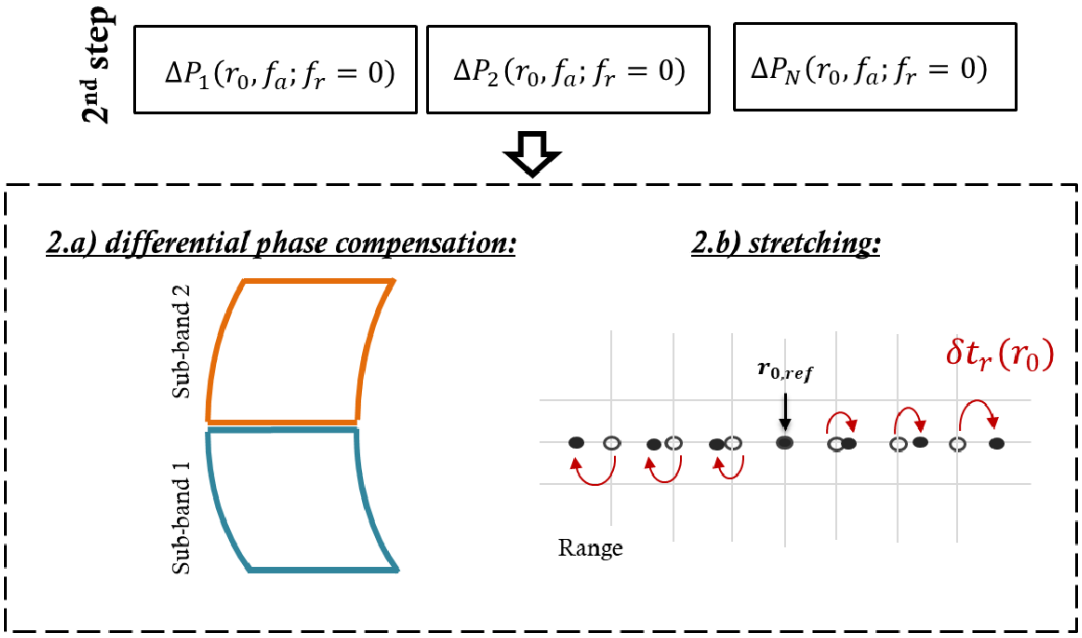

FIGURE 4.7: The second step of the two-step reconstruction, composed of a (left) differential phase compensation and (right) an interpolation. Note that the left-hand side illustration represents the fitting of differential phase compensation terms to the RCM of the aliased data in the range-Doppler domain as discussed in Subsection 3.3.3.

monochromatic range-variant filtering with $\Delta P_i(r_0, f_a; f_r = 0)$ where $\Delta\varphi_{i,\text{resi}} = 0$, and ii) a polychromatic range interpolation with $\Delta\varphi_{i,\text{resi}}(f_r, f_a; r_0)$. A low-order interpolator typically suffices to effect this residual correction in an accurate manner. Due to the smooth nature of $\delta t_r(r_0; f_a)$, its computation can be performed by scaling the values of the slopes of the residual phase of the reconstruction filters after linear regression. This regression can be computed using two to four samples in Doppler and range, so the impact on the overall burden is negligible. Figure 4.8 replicates Figure 4.4 showing the performance of the proposed reconstruction methodology for swath widths of 25, 50 and 100 kilometers, respectively. The phase error, caused by the impossibility to match the full range cell migration in the undersampled data, shows little dependence with the swath width and stays below 3° for a five kilometer baseline. These results suggest that this two-step reconstruction approach is capable of accommodating all relevant residual polychromatic components over wide swaths in an efficient manner.

4.1.2 Filter Validity

As any Fourier-based SAR processing kernel, the reconstruction algorithm has been derived under the assumption of azimuth invariance, i.e., the validity of constant geometric parameters within the processing block. As discussed in (Rodriguez-Cassola et al., 2015a), the validity of this assumption in an orbital geometry can be affected by topography, the rotation of the Earth, or the curvature of the orbits, resulting in a (space-variant) change of the effective velocity of the survey. Under the zero across-track baseline assumption, the sensitivity of the phases of the P_i filters

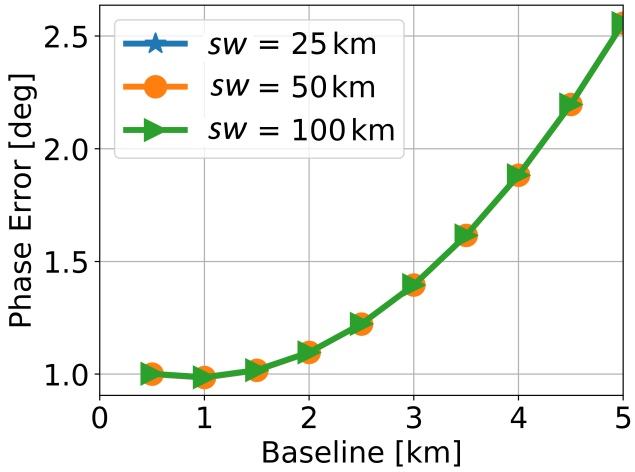

FIGURE 4.8: Phase error caused by the reconstruction method proposed in this thesis for a two-receiver X-band constellation with 15λ resolution and swath widths of 25, 50, and 100 kilometers, respectively.

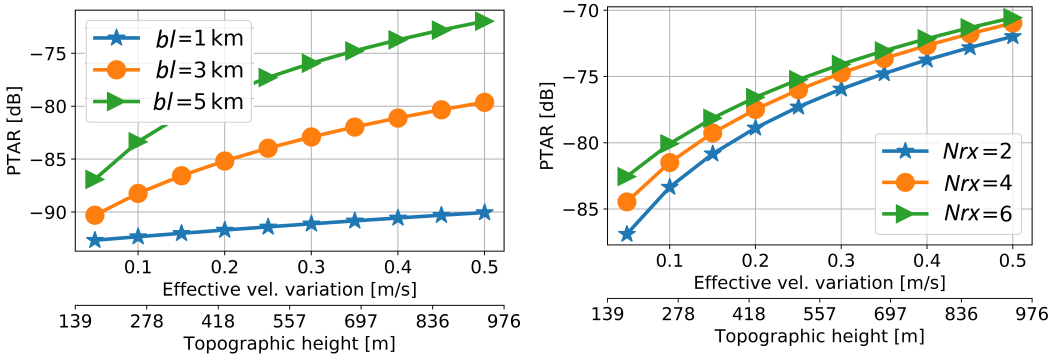

FIGURE 4.9: The peak-to-ambiguity ratio (PTAR) variation with respect to the effective velocity and topographic height for different along-track baselines (left) and number of receivers (right) in an X-band system with 15λ azimuth resolution. Note the variation of the phase errors in the reconstruction process due to a topography mismatch in the effective velocity within the transmitted bandwidth is negligible for the resolutions considered in the analysis.

with respect to the effective velocity can be approximated as

$$\delta\varphi_i(v_e) \approx \pi \left(\frac{f_0 + f_r}{c} \frac{b_i^2 \delta v_e}{r_0 v_e} \right), \tag{4.5}$$

where δv_e is any effective velocity variation in slow time. It is easy to see that the along-track baseline enhances the importance of this residual error, which may generate a raise in the ambiguities and the phase error at the maximum of the impulse response function. A phase error in the image pixels might be corrected after SAR focusing by means of a pixel-wise compensation.

In order to quantify the impact of the azimuth invariance assumption, the values of the sensitivity to topography presented in (Rodriguez-Cassola et al., 2015a) are used. Figure 4.9 shows the azimuth ambiguity level generated by (4.5) in terms of peak-to-ambiguity ratio (PTAR), measured as the ratio of the highest ambiguity level to the peak level of the main lobe. The simulations correspond to an X-band constellation with 15λ resolution. Note that a rectangular antenna pattern has been

assumed and no ambiguities due to the antenna sidelobes are to be expected. The left plot shows the variation of the ambiguity ratio with respect to the along-track baseline and the right plot shows the variation with respect to the number of receive channels. The increase in the ambiguity levels suggests that the impact of the changes in the effective velocity introduced by topography or the orbit curvature are minor, and can in practical terms be handled by updating the parameters of the reconstruction filters with every new processing block. In the case of extreme topographic variations within the footprint, a time-domain reconstruction as suggested in (Rodriguez-Cassola et al., 2015b) may be used.

4.1.3 Comparison of Reconstruction Results

This section presents a comparison of the reconstruction algorithms in (Krieger, Gebert, and Moreira, 2004b), an initial version of two-step reconstruction in (Sakar et al., 2018) and the one with the residual corrections in (Sakar et al., 2020a). The inversion method in (Krieger, Gebert, and Moreira, 2004b) provides an optimum filter computation result under regular sampling conditions. As discussed above, the two-step reconstruction approach can be extended to any other class of reconstruction algorithms in the literature just by modifying the shape of the reconstruction filters. An X-band constellation with 15λ resolution, curved orbits and the observation parameters of Figure 3.9 are used as a reference scenario. The results of each simulation show the phase error in the wavenumber domain, a 2D impulse response function zoomed close to the main lobe and azimuth profiles showing the first azimuth ambiguities raised by the reconstruction.

Figure 4.10 shows the reconstruction results of the algorithm in (Krieger, Gebert, and Moreira, 2004b) for a two-channel system with 10 m (left) and 800 m (right) along-track baselines. An analysis with respect to the swath width is irrelevant in this case, since the errors are dominated by the polychromatic components and the changes in the Doppler rate for the longer baselines. For the along-track baseline of 10 m, analogous to a single platform system, the algorithm shows good performance, with phase errors within the band smaller than 4°, an exact impulse response function, and ambiguities below -85 dB. For the baseline of 800 m, the phase error at the edges of the spectrum reaches up to $\pm 100^\circ$, resulting in a clear degradation of the impulse response and raise of azimuth ambiguities. The conclusion is that the method in (Krieger, Gebert, and Moreira, 2004b) provides an almost exact reconstruction for single-platform systems, but shows significant degradation in multistatic scenarios.

Figure 4.11 shows the reconstruction results of the two-step reconstruction method in (Sakar et al., 2018) for two along-tack baseline configurations: 1 km (left) and 3 km (right). In both simulations, the point target is located 50 km away from the reference point (that is used for the polychromatic bulk correction) to simulate the far range condition of a 100 km swath case. The results for the 1-km baseline show that the phase error remains less than 8°, the impulse response of the system shows no degradation and the azimuth ambiguities remain below -80 dB. In the case of the 3-km baseline, mentioned as a threshold in Figure 4.4, significant phase errors appear eventually resulting in raised ambiguities and a range shift of the impulse response function.

Figure 4.12 shows the reconstruction results of the generalized two-step range-Doppler reconstruction method proposed in (Sakar et al., 2020a) with a 5 km along-track baseline separation and a 100 km swath width for a constellation of two (left) and six (right) receivers. In both cases, the phase error at the edges of the spectrum remains less than 10°, no range shift in the impulse response is visible and the

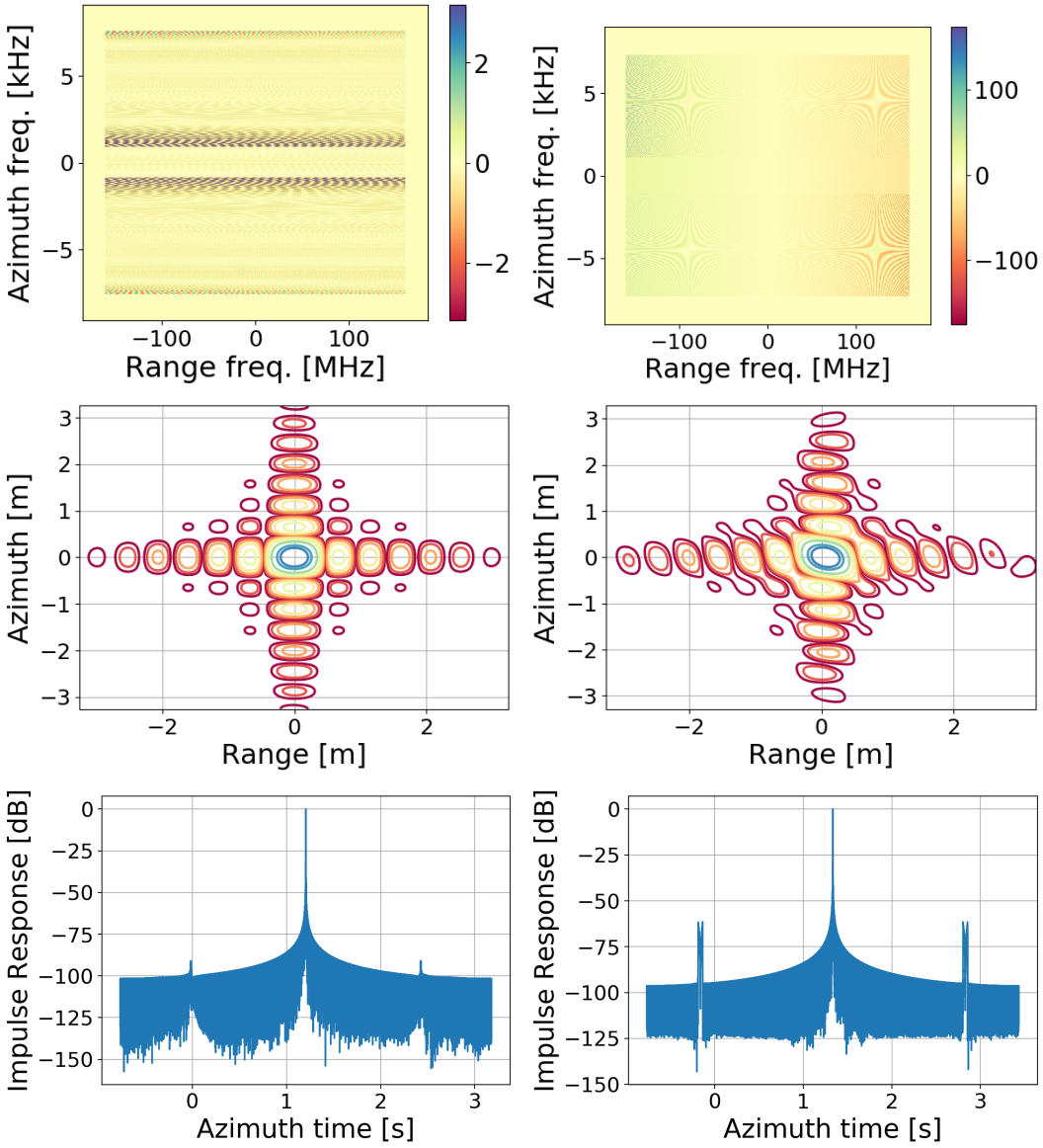

FIGURE 4.10: Point target reconstruction results with the method in (Krieger, Gebert, and Moreira, 2004b) for an X-band, 15λ azimuth resolution system with $b_2 = 10$ m (left) and $b_2 = 800$ m (right): (top) phase error in degrees, (middle) contour plot of the impulse response function, (bottom) azimuth point target response showing the ambiguities.

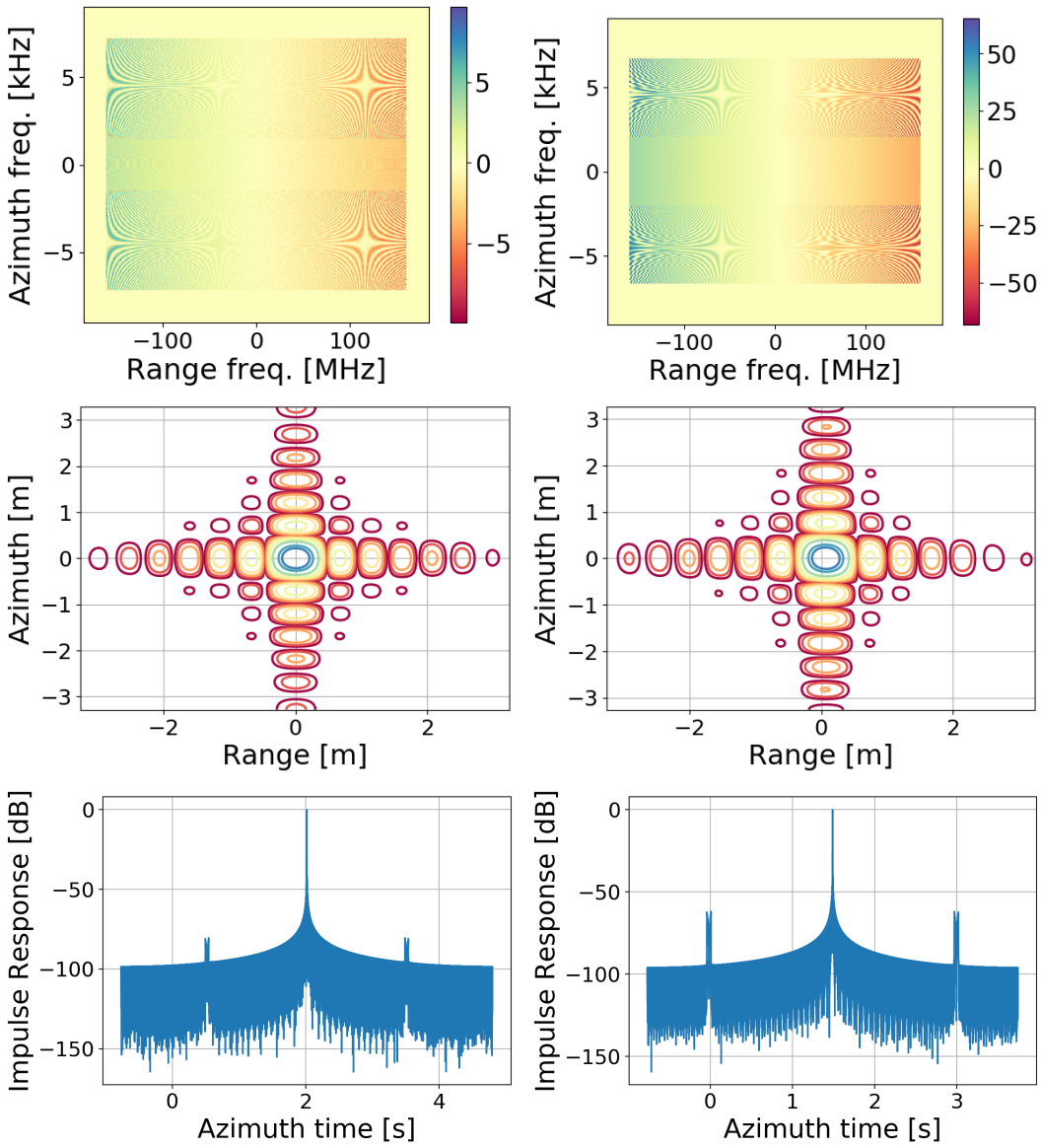

FIGURE 4.11: Point target reconstruction results with the method in (Sakar et al., 2018) for an X-band, 15λ azimuth resolution system with $b_2 = 1$ km (left) and $b_2 = 3$ km (right): (top) phase error in degrees, (middle) contour plot of the impulse response function, (bottom) azimuth point target response showing the ambiguities. The reference range for the bulk polychromatic reconstruction is 50 km away from the point target.

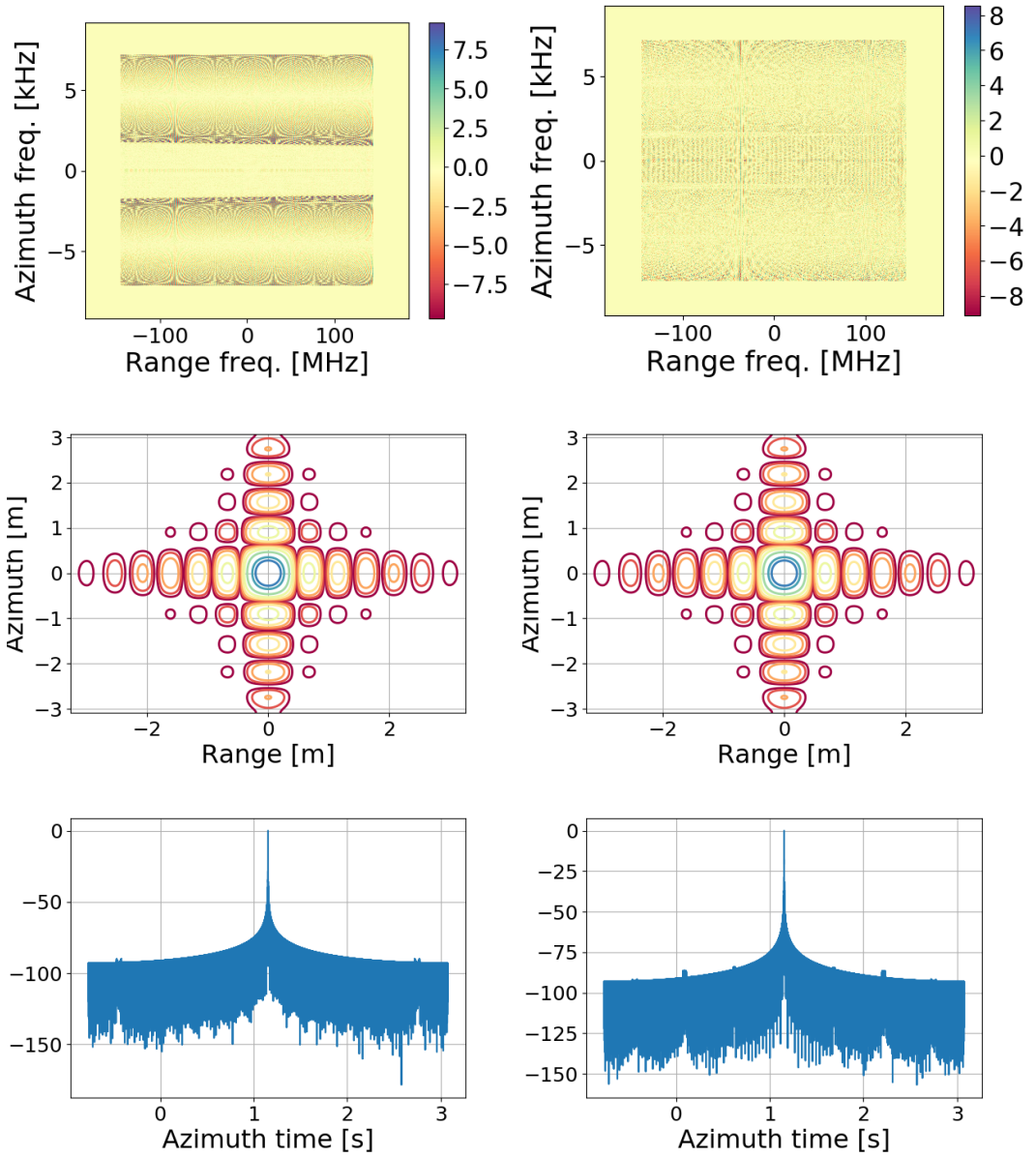

FIGURE 4.12: Point target reconstruction results with the algorithm suggested in (Sakar et al., 2020a) for an X-band, 15λ azimuth resolution system with $b_2 = 5$ km: (top) phase error in degrees, (middle) contour plot of the impulse response function, (bottom) azimuth point target response showing the ambiguities. The left and right plots correspond to two and six-receiver constellations, respectively. The reference range for the bulk polychromatic reconstruction is 50 km away from the point target.

azimuth ambiguities appear at around -90 dB, certainly due to the mismatch introduced by the range-cell migration in the handling of the sub-bands. As discussed in (Sakar et al., 2018), a larger number of receive satellites is expected to affect the performance of the reconstruction, as it results in more spectral copies in the aliased spectrum and more phase jumps in the reconstructed band. The results show very little degradation with respect to the former case, which suggests the robustness of the two-step reconstruction algorithm with residual corrections.

4.2 Reconstruction in Time Domain

The previous section presented a very accurate and thorough reconstruction approach effected in the Doppler domain. As stated in the introduction, any filter weight can be applied in both Doppler and time domains due to the equivalence of the azimuth time and Doppler frequency, which can be clearly noted in the relation already shown in Eq. (2.12), namely,

$$f_D = -K_\mathrm{a} t_\mathrm{a} \tag{4.6}$$

where K_a is azimuth chirp rate. This section presents a novel polychromatic time domain reconstruction approach valid for both constant and varying PRI schemes.

Similar to the approach followed in Section 4.1, the signal received by any receiver of the multistatic constellation will be expressed as the product of a transfer function common for all the constellations and a specific amplitude and phase deviation for each receiver, i.e.,

$$v_i(f_\mathrm{r}, f_\mathrm{a}) = A_i(f_\mathrm{a}, b_i) H_\mathrm{ref}(f_\mathrm{r}, f_\mathrm{a}) \exp\left\{-\mathrm{j}\Delta\Phi_i(f_\mathrm{r}, f_\mathrm{a}; b_i, t_{\mathrm{in},i}[m])\right\}, \tag{4.7}$$

where i refers to the receiver, f_r and f_a are the range and azimuth frequency, respectively, $t_\mathrm{out}[k]$ represents the time samples regularly spaced, A_i is the joint antenna pattern corresponding to receiver i, H_ref is the transfer function of a reference sensor of the constellation (e.g., the transmitter), $\Delta\Phi_i$ is a residual phase term which accounts for the range history difference between the reference and receiver i, b_i is the baseline of receiver i from the transmitter, and $t_{\mathrm{in},i}$ describes the azimuth sampling of receiver i, assumed to be within the correlation distance of $t_\mathrm{out}[k]$. Figure 4.13 sketches the sampling situation before and after reconstruction. As discussed in Chapter 3 and (Sakar et al., 2018), $\Delta\Phi_i$ can be well approximated by a quadratic polynomial [see Eq. (3.11)]. Note that in the case of single-pass constellations $t_{\mathrm{in},i}$ is the same for all receivers and in repeat-pass constellation $\Delta\Phi_i = 0$.

Since the analogy of the suggested sampling scheme with the staggered SAR case is evident (Villano, Krieger, and Moreira, 2014), a Wiener filter (for the considered case equivalent to a least mean squares or best linear unbiased estimator) is chosen to compute the reconstruction weights for each output time instant.[2] Compared with reconstruction approaches in the literature, the suggested algorithm is capable of accommodating bistatic range histories and patterns and the polychromatic nature of the radar echoes, which have been shown to introduce significant reconstruction mismatch, range-cell shift and raise to azimuth ambiguities for increasing along-track baselines and resolutions (Sakar et al., 2018).

The computation of the weights according to the minimization of the mean square estimation error for each output time instant and a given slant range involves

[2] In case of a recurrent PRI variation, the weights need to be computed only for one PRI variation window.

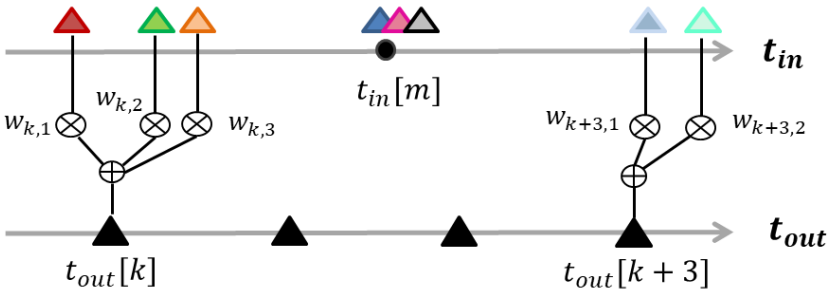

FIGURE 4.13: Illustration of the time-domain reconstruction with the Wiener filter for varying PRI and α. Note the number of samples in the output grid is lower than that of the receivers, i.e., oversampling may be required to compensate for the irregularity of the sampling.

the solution of N_{cl} non-linear equations, N_{cl} being the number of receivers with samples within the correlation window, which can be expressed in matrix form as

$$\underline{\boldsymbol{w}}_{\text{MSE}}(f_{\text{r}}; t_{\text{out}}[k]) = \underline{\boldsymbol{R}}_{\boldsymbol{v}}^{-1}\underline{\boldsymbol{r}}_{\boldsymbol{d}}, \tag{4.8}$$

where for each f_{r}, $\underline{\boldsymbol{R}}_{\boldsymbol{v}}$ is the $N_{\text{cl}} \times N_{\text{cl}}$ autocorrelation matrix and $\underline{\boldsymbol{r}}_{\boldsymbol{d}}$ is the $N_{cl\times 1}$ cross-correlation column vector. The autocorrelation and cross-correlation functions are

$$\underline{\boldsymbol{R}}_{\boldsymbol{v}}(f_{\text{r}}; t_{\text{out}}[k]) = \underline{\boldsymbol{v}}(f_{\text{r}}, f_{\text{a}}; t_{\text{out}}[k])\underline{\boldsymbol{v}}(f_{\text{r}}, f_{\text{a}}; t_{\text{out}}[k])^{H}, \tag{4.9}$$

$$\underline{\boldsymbol{r}}_{\boldsymbol{d}}(f_{\text{r}}; t_{\text{out}}[k]) = \underline{\boldsymbol{v}}(f_{\text{r}}, f_{\text{a}}; t_{\text{out}}[k])v_{\text{ref}}, \tag{4.10}$$

where $\underline{\boldsymbol{v}}(f_{\text{r}}, f_{\text{a}})$ is N_{cl}-element column vector,

$$\underline{\boldsymbol{v}}(f_{\text{r}}, f_{\text{a}}) = \left[v_1(.), v_2(.), \cdots v_{N_{cl}(.)}\right]^T \tag{4.11}$$

H denotes Hermitian transpose, and

$$\begin{aligned} v_{\text{ref}}(f_{\text{r}}, f_{\text{a}}; t_{\text{out}}[k]) &= A_{\text{ref}}(f_{\text{a}})H_{\text{ref}}(f_{\text{r}}, f_{\text{a}}) \\ &= A_{\text{ref}}(f_{\text{a}})\exp(-\text{j}2\pi t_{\text{out}}[k]f_{\text{a}}) \end{aligned} \tag{4.12}$$

where $A_{\text{ref}}(f_{\text{a}})$ is the antenna pattern of the reference of the constellation. Note that the weights are both range-time and range-frequency dependent, but not Doppler-frequency dependent due to the sum operation over f_{a} in the matrix multiplication in (4.9) and (4.10). The length of the Wiener filter extends to the correlation length of the reconstructed signal, which should at least cover the separation corresponding to the azimuth resolution of the system (Villano, Krieger, and Moreira, 2014).

Figure 4.14 shows the characterisation of the 2D impulse response of a multistatic L-band along-track constellation operated with a variable PRI with the parameters shown in Table 4.1. The PRI is random and uniformly distributed in the interval

$$\text{PRI} \in \left[\overline{\text{PRI}}\left(1 - \frac{m}{2}\right), \overline{\text{PRI}}\left(1 + \frac{m}{2}\right)\right], \tag{4.13}$$

where m is the variation margin. Note that $m = 0$ corresponds to a constant PRF case. The baseline of all receivers is around 1 km and has been generated randomly within one azimuth resolution segment and kept constant for the duration of the

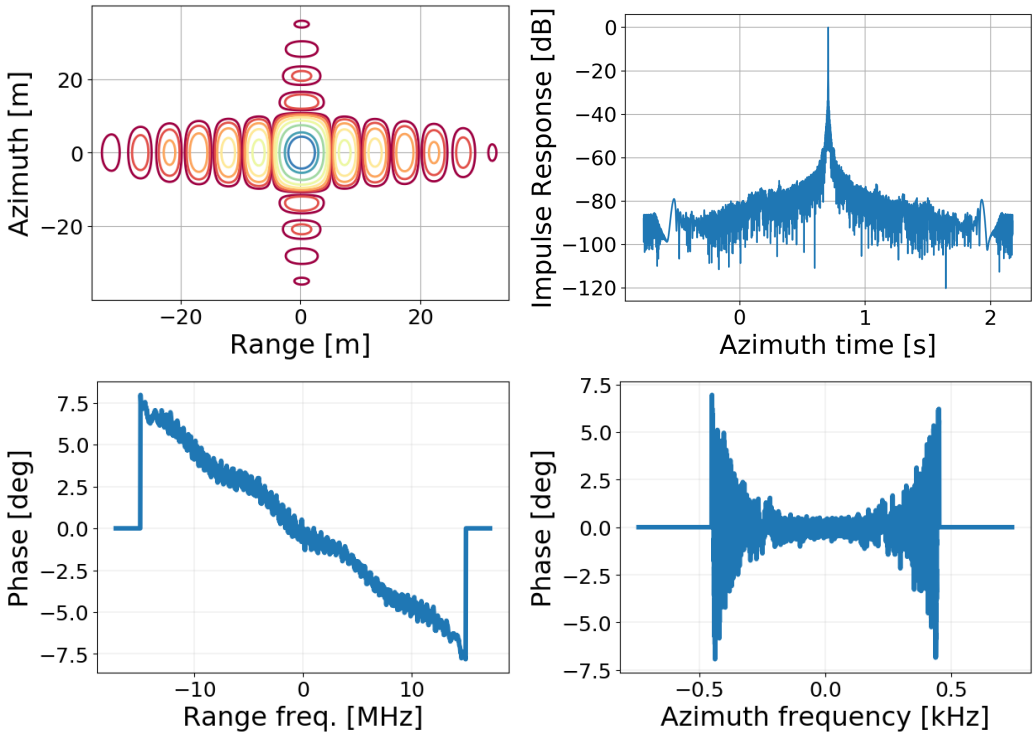

FIGURE 4.14: 2D impulse response computed after monochromatic time-domain reconstruction using the parameters listed in Table 4.1. For the sake of illustration, the reconstruction coefficients of (4.8) have only been computed for $f_r = 0$.

TABLE 4.1: System parameters used in the simulation of Figure 4.14.

Parameter	**Symbol**	**Value**
Wavelength [m]	λ	0.25
Mean PRF [Hz]	PRF	296
Azimuth resolution [m]	δ_{az}	5
Transmitted bandwidth [MHz]	B_{rg}	30
Number of Rx	N_{rx}	10
Along-track baseline [km]	b_i	~ 1
System scaling	η_{SS}	5
Oversampling	α	1
PRI variation [%]	m	10
Velocity [m/s]	v_s	7100

simulation. From that perspective, the figure shows a single realization which may not be used to draw quantitative conclusions, but is fully representative of the validity of the approach. The figure shows an accurate focusing and a good ambiguity suppression, as expected from the parameters of the simulation. No major trend is identified in the azimuth phase plot (bottom right), other than increased noise at the edges of the band. Note that, however, the reconstruction has been conducted with weights computed at $f_r = 0$ and can be considered as monochromatic, which is the reason why a linear phase ramp in the range frequency domain appears (bottom left), even for the modest transmitted bandwidths.

Two different ways of correcting for the polychromatic effects in the reconstruction are proposed (Sakar et al., 2020b): i) using a bank of band-pass filters, and ii) by means of a bulk *a priori* phase correction.

4.2.1 Polychromatic Reconstruction: Band-pass Filter Method

The band-pass filter method is illustrated in Figure 4.15. The data are range band-pass filtered in a number of different branches, each reconstructed in time domain with the central wavelength of the sub-band, then stitched together in the range frequency domain. The central wavelength of the band-pass filters is

$$\lambda_i = \frac{c}{f_0 + \delta f_i}, \tag{4.14}$$

where δf_i is the shift to the center of the sub-band. Note that some overlap and feathering between the band-pass filters should be used in order to guarantee phase continuity. Figure 4.16 shows the reconstruction results of a point target with the parameters of Figure 4.14. The results show that the linear phase error is successfully removed with this method. The number of the required sub-bands depends on the range resolution. In this example, 16 sub-bands were used, which results in longer processing times for finer resolution systems.

4.2.2 Polychromatic Reconstruction: *A Priori* Bulk Phase Correction

An alternative – and less taxing – solution is based on using an *a priori* bulk phase correction of the first term in Eq. (3.11) for a given reference range. The term, besides being Doppler independent, allows to compensate for most of the polychromatic terms prior to reconstruction.

The block diagram of this approach is shown in Figure 4.17. The first step is to remove the dominant polychromatic term of a reference slant range in range frequency domain, which can be expressed as

$$\Delta\varphi_{i,\text{bulk}} \approx 2\pi \frac{f_0 + f_r}{c} C_0(r_{0,\text{ref}}), \tag{4.15}$$

where obviously f_r covers the entire range frequency extent. After the data are brought back into the time domain, a regular monochromatic reconstruction containing the rest of the phase terms in Eq. (3.11) for the center range frequency can be applied.

To provide the necessary clarity and insight, Figures 4.18 and 4.19 elaborate the basis of this approach. The left plots of Figure 4.18 show the first term in Eq. (3.11) (top) and the phase of a polychromatic range-variant reconstruction filter w_i defined in Eq. (4.8) (bottom). It is evident that the phase of the reconstruction filter is almost equal to the first term of the phase deviation and the dominating phase in the

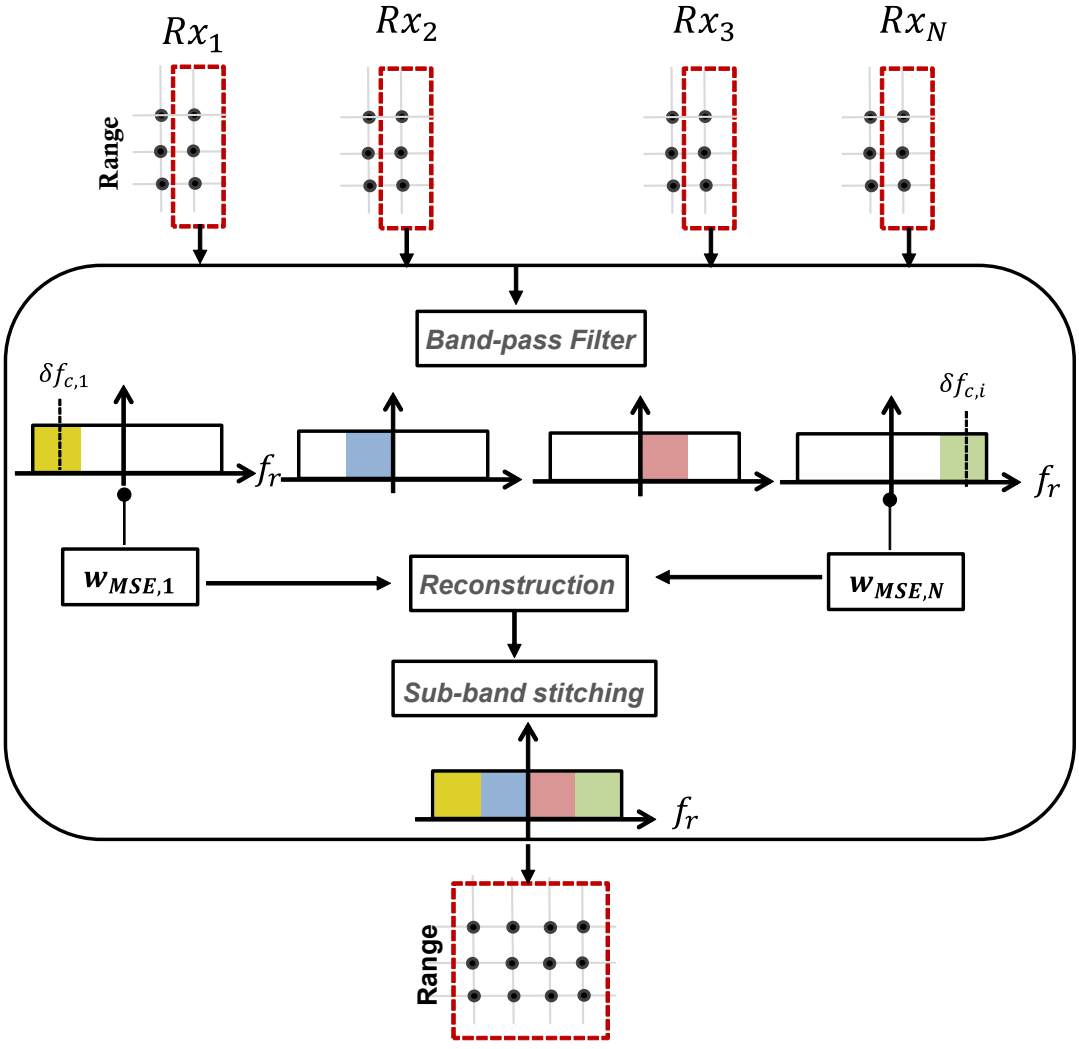

FIGURE 4.15: Band-pass filter approach: Illustration of polychromatic time-domain reconstruction. The input data are filtered in the range-frequency domain and brought back to the time domain for the reconstruction with the center frequency of each sub-band. After the simultaneous reconstructions, the sub-bands are stitched in range-frequency domain and the initial range sampling is retrieved.

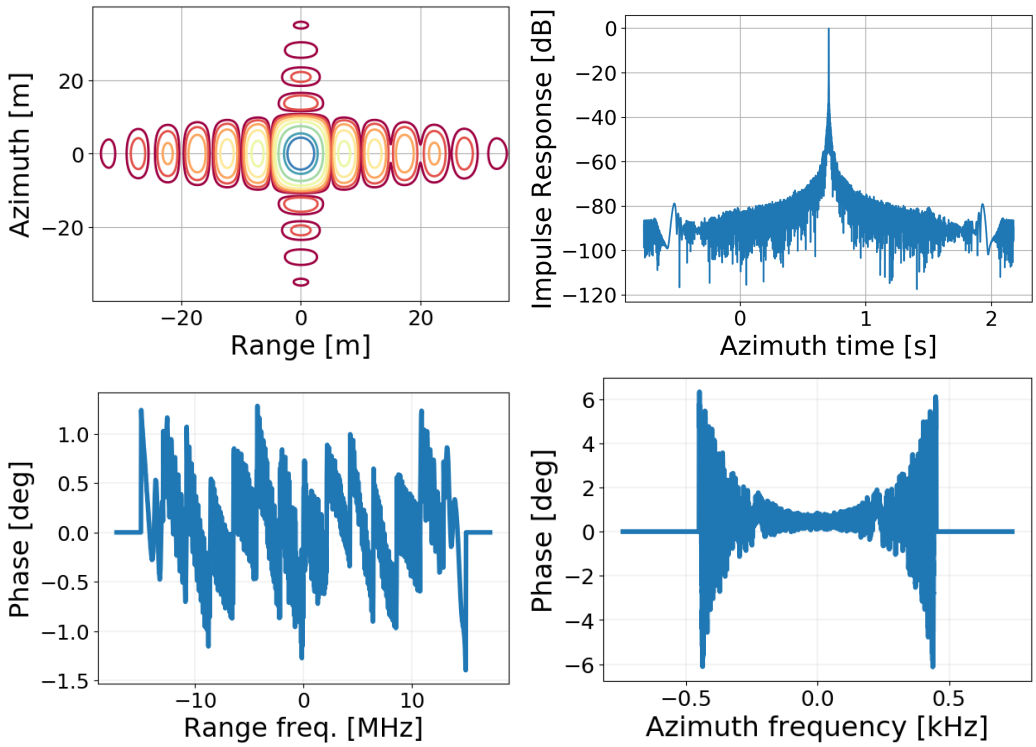

FIGURE 4.16: Polychromatic reconstruction approach using filter bank with sixteen band-pass filters.

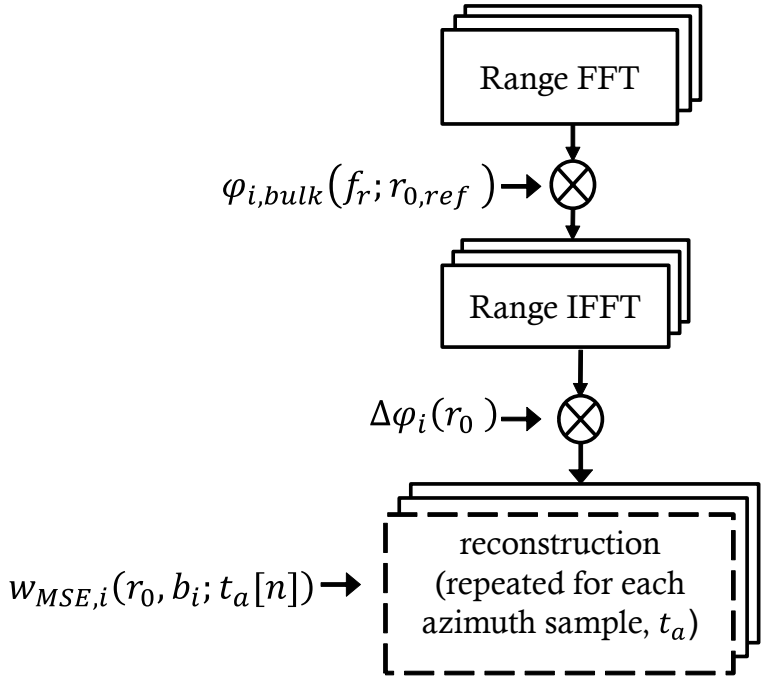

FIGURE 4.17: Block diagram of the *a priori* phase compensation approach.

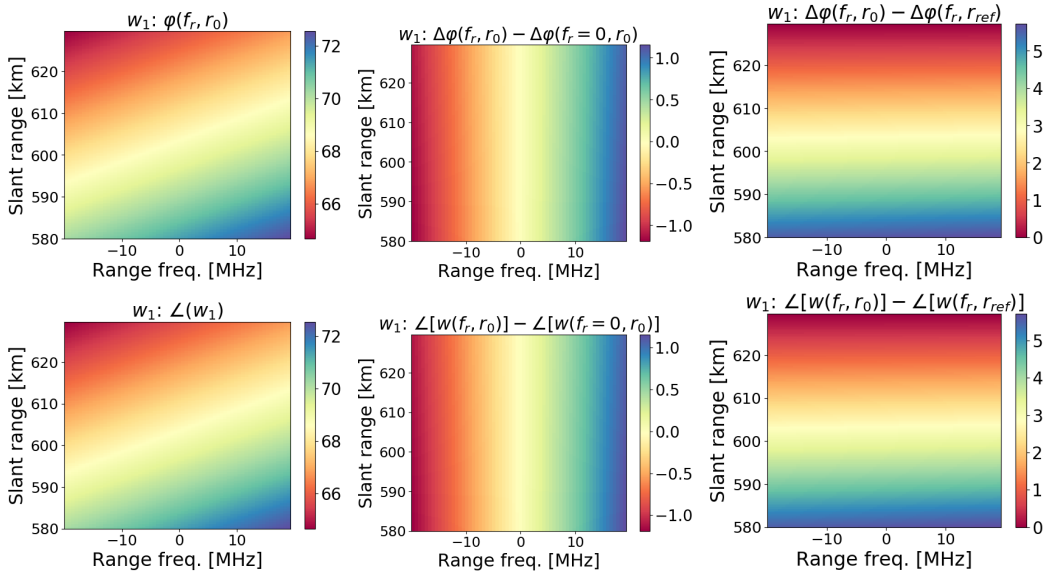

FIGURE 4.18: Top: First term of the residual phase defined in (3.11), bottom: phase (in degrees) of reconstruction filter defined in (4.8). The left plots show variation of the phases with respect to range and range frequency for 15λ systems in L-band, the middle plots show the residual (in degrees) phase, if variation in range frequency is neglected, and the right plots show the residual phase (in degrees), if variation in slant range is neglected.

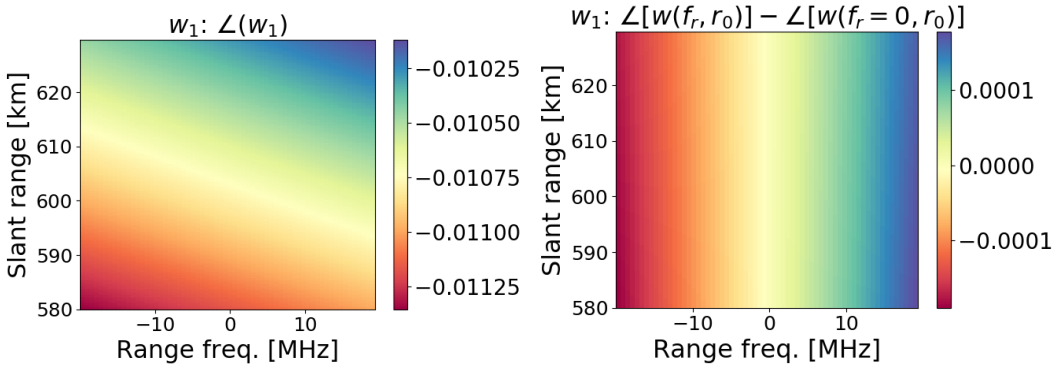

FIGURE 4.19: (Left): 2D phase (in degrees) of the reconstruction filter w_1, (right): uncompensated phase (in degrees) of the reconstruction filter w_1.

reconstruction filter comes from this bulk term. The middle and left plots show remaining uncompensated phase errors, if the reconstruction is done only accounting for the center frequency (monochromatic, range-variant) or alternatively for the reference range (polychromatic, range-invariant), respectively. For an L-band system with 15λ resolution and 100 km swath width, the results suggest that range-variant terms introduce larger phase deviations.

Figure 4.19 shows the phase of reconstruction filter when the bulk phase term is removed prior to the reconstruction and the remaining uncompensated phase. As seen from the right plot, the residual phase is negligibly small. Figure 4.20 shows the results of the reconstruction of the same simulation scenario using this second method. As in the bandpass filter method, the linear phase in range frequency is removed and the impulse response function presents no shift in range.

It is evident that the combination of the proposed methods might provide a reasonably efficient solution for very high-resolution multistatic SAR constellations,

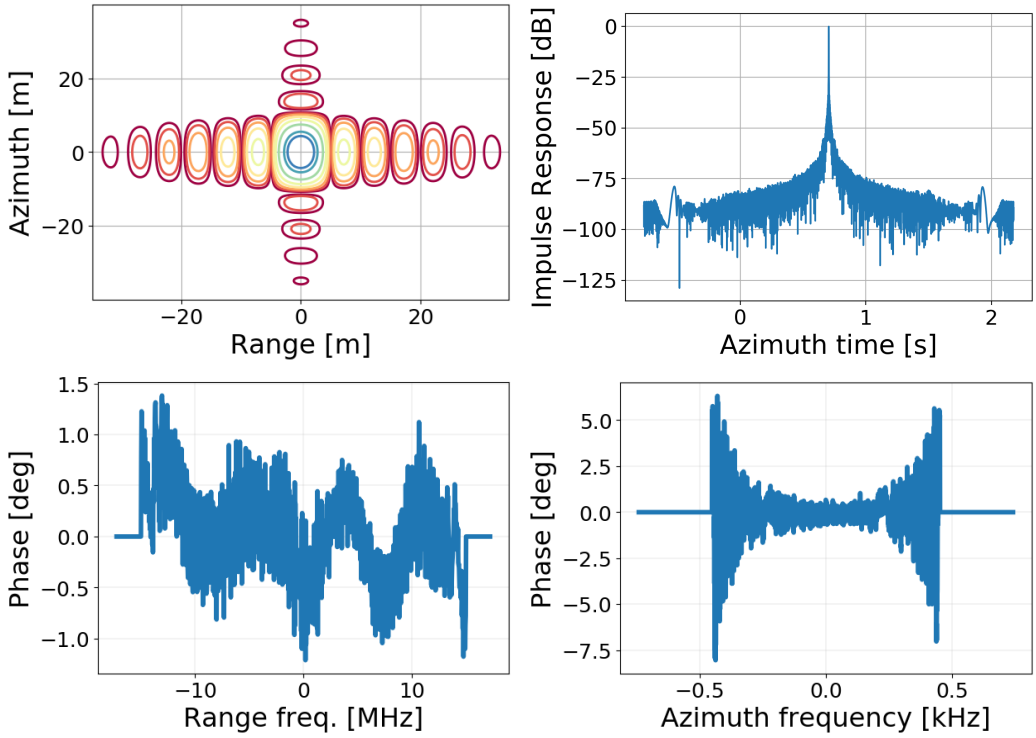

FIGURE 4.20: Polychromatic time-domain reconstruction with *a priori* phase compensation. The point target is placed 20 km away from the reference range bin.

TABLE 4.2: System parameters used in the simulations of Figures 4.21 and 4.24. The number of the receiving satellites are $N_{rx} = (1+\alpha)\eta_{SS}$.

Parameter	**Symbol**	**Value**
Wavelength [m]	λ	0.25
Mean PRF [Hz]	PRF	238
Number of Rx	N_{rx}	8
Swath Scaling	η_{SS}	5
Oversampling	α	0.5
Margin	m	0.1

such an approach being realized as i) an *a priori* bulk phase correction for a reference range, followed by ii) a band-pass reconstruction using a reduced number of range sub-bands.

For the sake of completeness, Figure 4.21 shows the results of a reconstructed target for two different cases of PRI variation. The figure shows the ability of the suggested algorithm to cope with different types of PRI sequence, showing results for a random variation (left), and a fast linear variation (right), repeated with a frequency of 30 transmit intervals. The parameters used in simulations are given in Table 4.2. As expected, the variation of the PRI results in a smoothening of the azimuth ambiguities causing an overall increase of the noise floor (or integrated side-lobe ratio) in the response. This smoothening appears to be better distributed in the fully randomized case. The main reason for that is the fact that randomly selected PRI within a range naturally deals with any periodic long sampling gaps in case of coinciding sampling. In comparison to the single-platform or single-platform multi-channel staggered SAR configuration, the repetitive sampling gaps cannot be overcome by

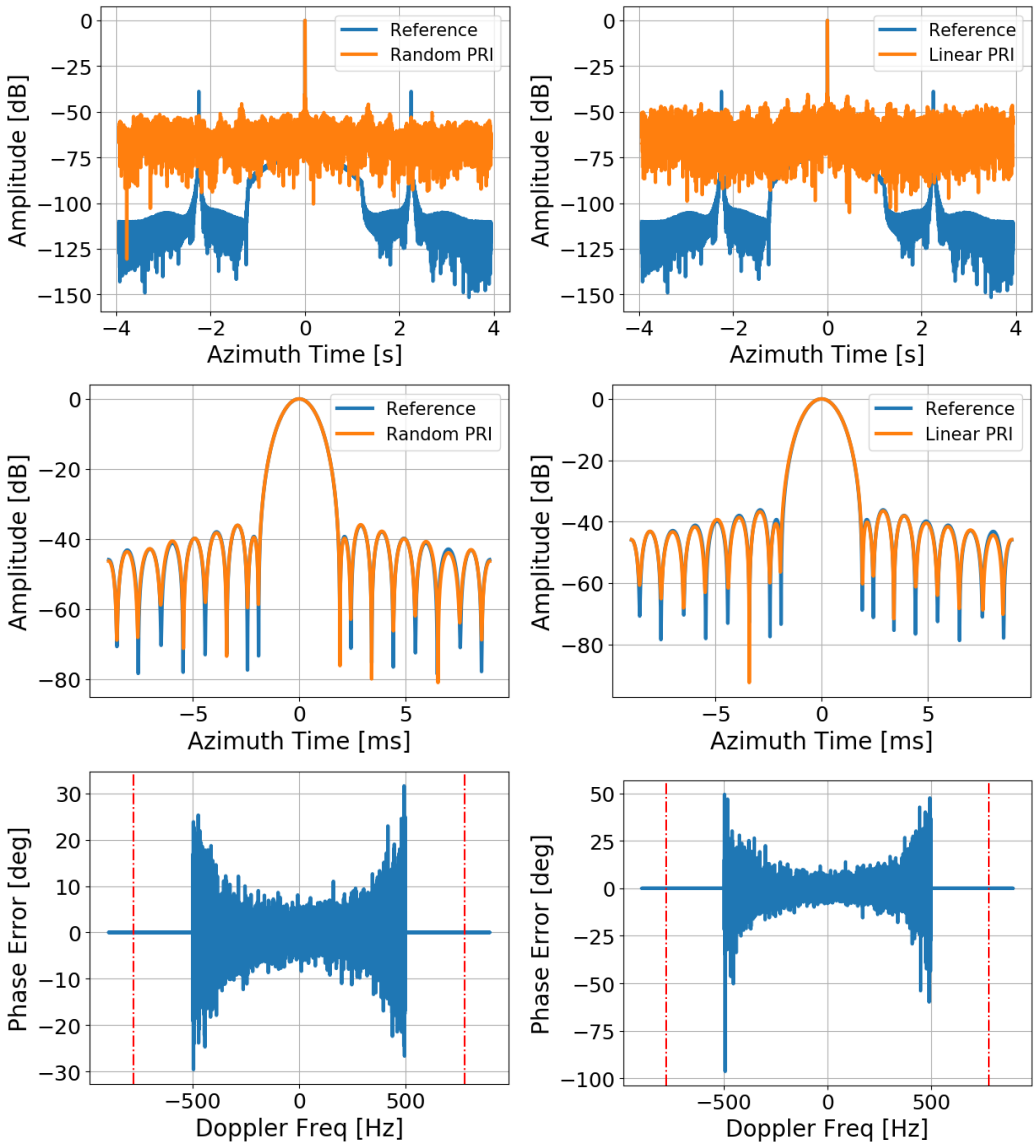

FIGURE 4.21: Reconstruction results using the suggested algorithm with sub-band accommodation of the polychromatic aberrations for (left) random, and (right) fast linear PRI variations using the simulation parameters of 4.2. The figure shows the impulse response (top), a zoom over the peak and principal side-lobes (middle), and the phase error in the Doppler domain (bottom).

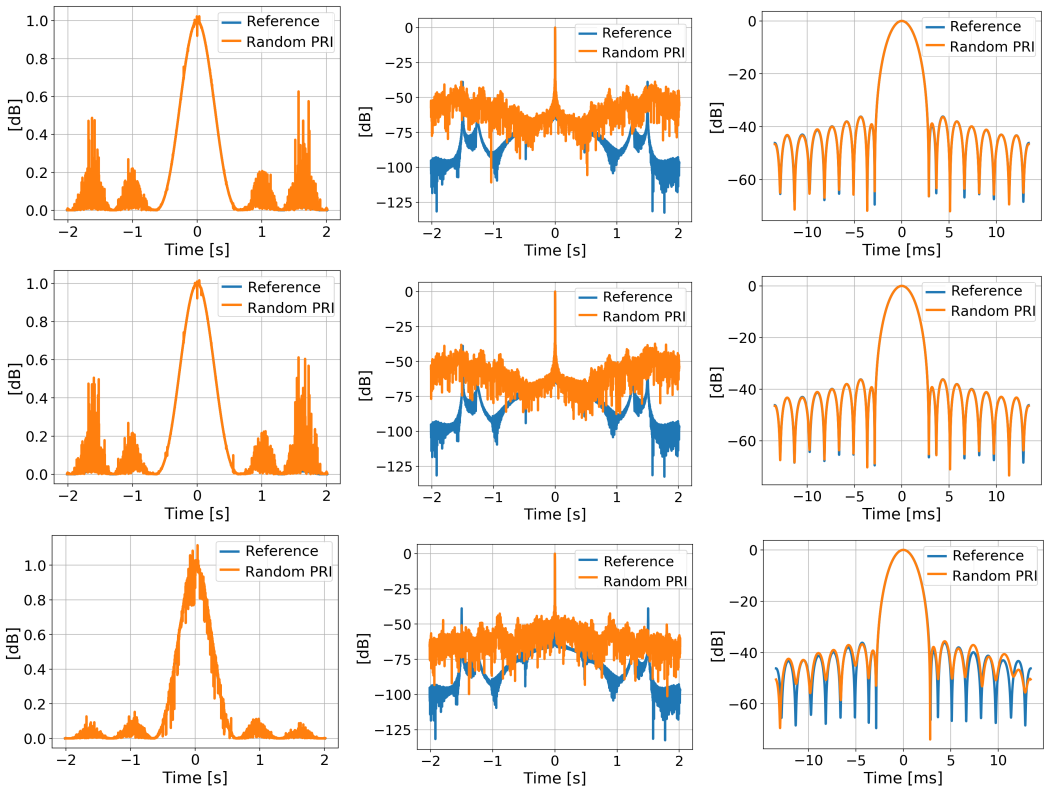

FIGURE 4.22: 1D time domain reconstruction of a constellation with random PRI variations using the simulation parameters of Table 4.2 ($N_{rx} = 8$) for a correlation length of (top row): L_a/v_s, (middle row): $10L_a/v_s$ and (bottom row): $L_a v_s/2$. Left: Reconstructed raw data, middle: Full impulse response function, right: zoomed impulse response function. Blue line: reference, orange line: reconstruction with random PRI.

simply designing a PRI variation, since the sampling condition is equally influenced by the relative receiver positions. In terms of efficiency, the linear PRI variation provides an advantage because its temporal pattern roughly repeats in the case of the reconstruction weights. Note that the simulations in this and the following sections include all azimuth ambiguities to be able to present a fair comparison between the reference and reconstructed signals.

4.2.3 Correlation Length

As discussed previously, the maximum distance between input samples used for reconstruction and output time instant $t_{out}[k]$ is defined by the correlation length, L_a/v_s (Villano, Krieger, and Moreira, 2014), since the auto-correlation function of the random-complex process becomes uncorrelated outside of this length. On the other hand, the reconstruction process is a regularization of a non-uniform sampling scheme via interpolation, and the longer the interpolator length is, typically the better an interpolator performs. In this section, the correlation length limit is discussed briefly. For time-domain reconstruction, the sampling condition, entailed by the system PRF and the position of receivers, is essential for the final performance. For the interpolation, the number of available samples and their distance to the point of interest are essential. Figure 4.22 shows a comparison of the reconstruction results with the correlation length defined by (top) one antenna length, (middle) half of the

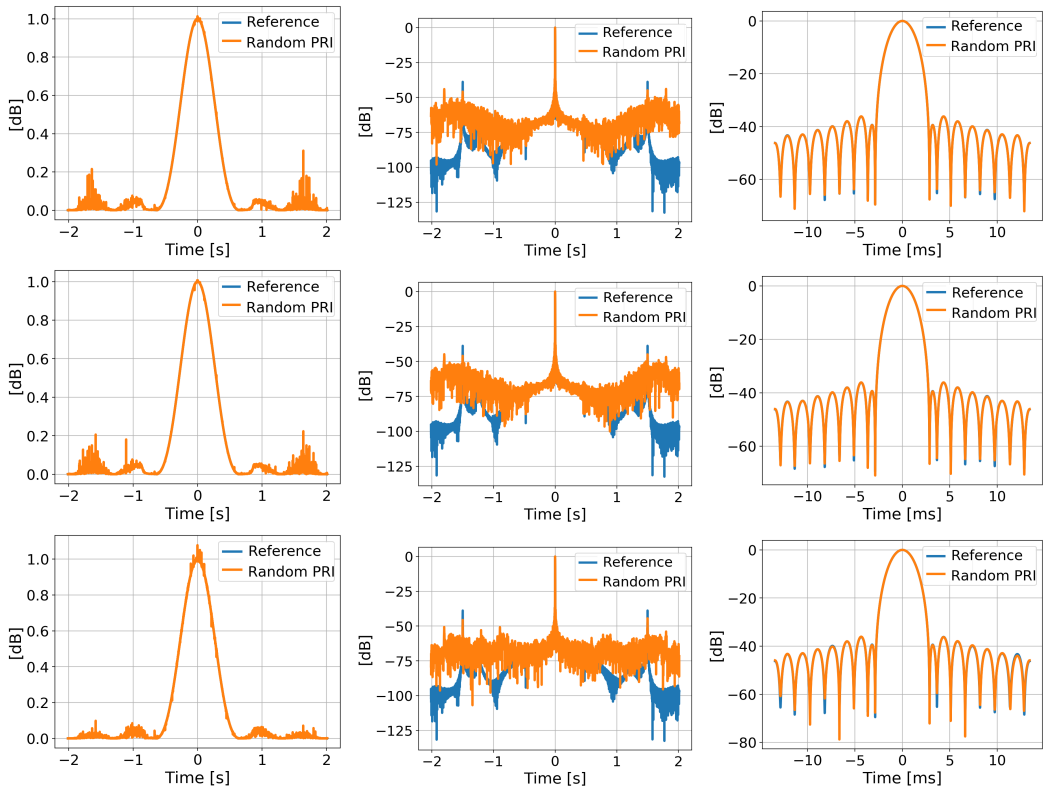

FIGURE 4.23: 1D time domain reconstruction of a constellation with random PRI variations using the simulation parameters of Table 4.2 with $\alpha = 1$ ($N_{rx} = 10$) for a correlation length of (top): L_a/v_s, (middle): $10L_a/v_s$ and (bottom): $L_a v_s/2$. Left: Reconstructed raw data, middle: Full impulse response function, right: zoomed impulse response function. Blue line: reference, orange line: reconstruction with random PRI.

antenna length and (bottom) ten times the antenna length. In all cases, the reconstruction of the main lobe is fairly good, whereas there is a prominent noise power on the sidelobes that increases with increasing correlation length. Another obvious outcome is that the samples outside of one correlation length do not contribute to the performance of the reconstruction, in terms of resolution, AASR and PSLR. On the other hand, half of a correlation length results in better AASR at the expense of jitter in the main lobe. As it will be discussed extensively in Chapter 5, one viable option to decrease the noise is to increase the samples of interpolation by increasing the number of receivers (with oversampling α). Figure 4.23 shows that a larger number of receivers favours a shorter correlation length.

4.3 Equivalence between Time- and Doppler-Domain Reconstruction

In order to provide further insight into the particularities of time- and Doppler-domain reconstruction for multistatic SAR constellations, this section provides a direct comparison of methods presented in Section 4.1 and Section 4.2 . Both methods have been shown to be valid for multistatic constellations with large along-track baselines, high resolution, and over swaths of hundreds of kilometers. As discussed in (Sakar et al., 2020a), the Doppler-domain approach is independent of the method

with which the reference reconstruction filters are computed, i.e., any of the methods reported in (Krieger, Gebert, and Moreira, 2004b; Gebert, Krieger, and Moreira, 2009; Cerutti-Maori et al., 2014a; Sikaneta, Gierull, and Cerutti-Maori, 2014; Li et al., 2005; Cerutti-Maori et al., 2014b) can be used to compute the reference filters.

Figure 4.24 shows the reconstruction results for a constant PRF case using the simulation parameters of Table 4.2 in (left) time and (right) Doppler domains. As expected, the performance of the reconstruction is similar in both cases, with similar levels of noise floor as in the reference case. The Doppler-domain reconstruction, however, provides lower levels of azimuth ambiguities and phase noise because of the limited correlation length assumed for the derivation of the reconstruction weights in the time domain, which results in a slight increase of aliasing. As shown in (Sakar et al., 2020a), the reconstruction algorithm can remove the geometry related phase deviations resulting from the bistatic observation geometry very accurately. Nevertheless, the sidelobes of the joint antenna pattern raise the azimuth ambiguities along the acquisition (Gebert, Krieger, and Moreira, 2009).

A more interesting scenario for multistatic SAR processing is the reconstruction in the Doppler domain for periodic PRI variation schemes, in which each sample of a PRI cycle should be handled as an additional channel (Villano, Krieger, and Moreira, 2014). This of course increases the size of the reconstruction matrices, which is expected to raise the computational burden and the impact of noise and numerical instabilities with respect to the constant PRI model. Figure 4.25 shows the reconstruction results using time- and Doppler-domain algorithms for a linear PRF case with the same repeat pattern of thirty pulses used as in the previous example and the simulation parameters of Table 4.2.

The top-left plot illustrates a direct comparison of reconstructions in the Doppler domain with a constant (orange) and a linearly varying PRI (green), and in time domain with the same linear PRI variation (blue). The differences between the blue and green curves, clearer than in the previous example, are due to the limited length of the correlation window used for the time-domain reconstruction. The conclusion of the section is however clear: besides the fact that any of the reconstruction methodologies discussed may be successfully applied in operational scenarios, they provide a solid basis for the estimation of the performance and efficiency of realistic multistatic SAR constellations operated with constant, periodic, and fully random (i.e., aperiodic) PRI schemes.

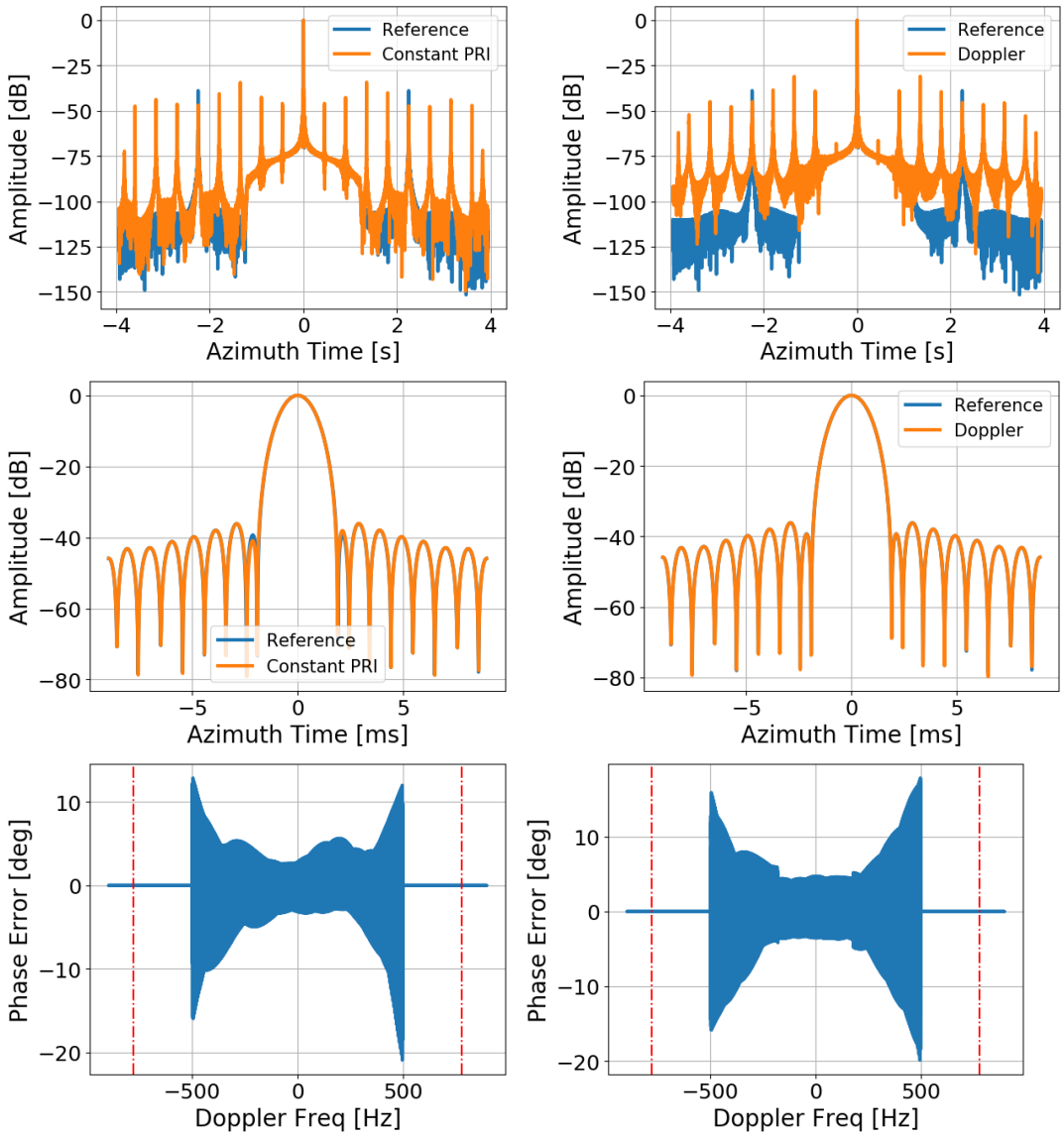

FIGURE 4.24: Reconstruction results for (left) time- and (right) Doppler-domain algorithms using the simulation parameters of Table 4.2. The figure shows the impulse response (top), a zoom over the peak and principal side-lobes (middle), and the phase error in the Doppler domain (bottom).

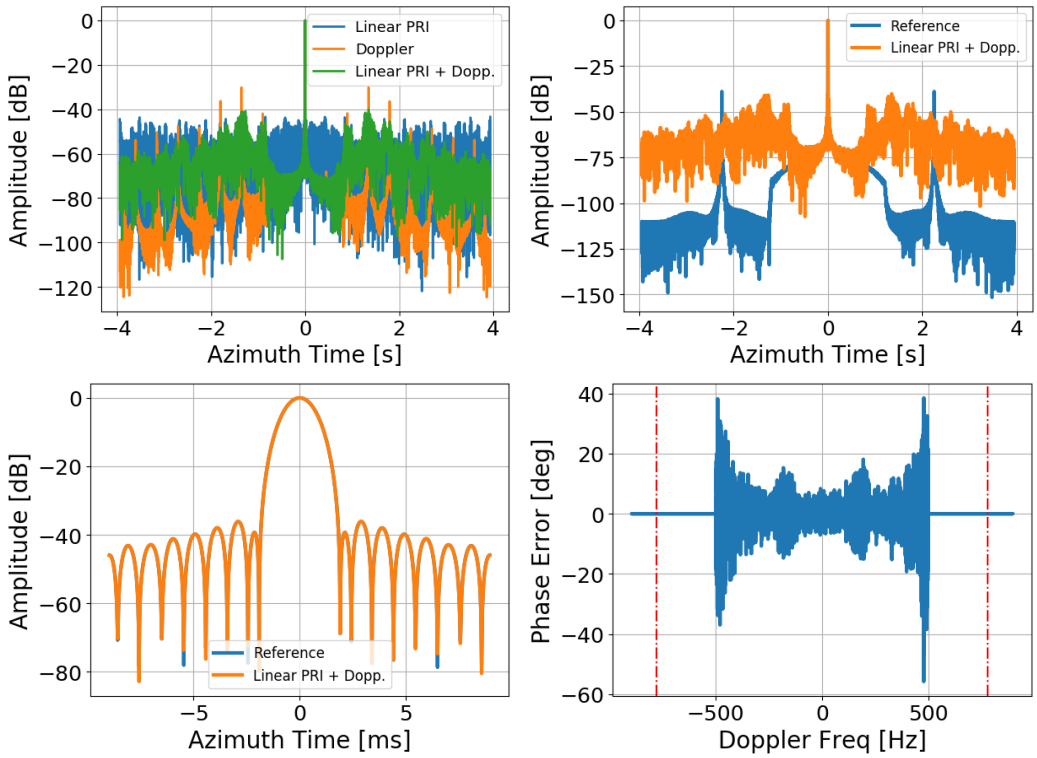

FIGURE 4.25: Reconstruction comparison of linear PRI variation in time and Doppler domains using the same simulation parameters of Table 4.2. The figure shows the impulse response (top), a zoom over the peak and the first side-lobes (bottom-left), and the phase error in the Doppler domain (bottom-right).

4.4 Conclusion

Multistatic SAR constellations with large along-track baselines and high resolution require a more elaborated reconstruction approach than those available in the literature in order to accommodate polychromatic and range-variant phase differences between the sensors. Due to several geometrical approximations, the reconstruction methods in the literature, originally developed for single-platform systems, fail to achieve the accuracy required for multistatic constellations with baselines larger than just a few hundred meters. In order to address this gap in the literature, this chapter has presented several accurate azimuth reconstruction approaches in Doppler domain and in time domain.

The work as presented in (Sakar et al., 2018) suggested a two-step Doppler domain reconstruction approach to accommodate the polychromatic terms of the azimuth reconstruction, which provided good accuracy for range blocks in the order of a few kilometers. Beyond these values, it has been shown that uncompensated polychromatic terms introduced range shifts and relevant phase errors in the reconstructed data. Further work, presented in (Sakar et al., 2020a), proposed an improved two-step azimuth reconstruction approach for multistatic SAR constellations achieving accurate polychromatic reconstruction in orbital cases and over swaths of hundreds of kilometers. The method consists of a range-invariant bulk polychromatic correction effected in the wavenumber domain followed by a range-variant residual correction in the range-Doppler domain, which includes a residual range interpolation removing the remaining polychromatic terms. It has been shown in Section 4.1 that the suggested algorithm achieves accurate reconstruction with very

high-resolution systems, kilometric baselines, and over areas of hundreds of kilometers. The accuracy of the method is verified also with a larger number of receivers. The investigations suggest that this approach can be considered as the general Fourier-based solution for the azimuth reconstruction of multistatic SAR data.

Based on the gained knowledge on the azimuth reconstruction in Doppler domain, two different polychromatic time-domain reconstruction approaches were presented in Section 4.2. Both of the methods are valid for constant and varying PRI configurations. The filter bank approach applies band-pass filters to the data such that each sub-band is reconstructed with respect to its central frequency, and then stitched together in the range frequency domain. The *a priori* phase correction approach corrects for the dominating bulk phase in range frequency domain and the residual phase deviation is compensated in a monochromatic manner. Both of the methods are validated with 2D point target reconstruction. Finally, the equivalence of Doppler and time-domain reconstruction approaches have been discussed.

Besides being equivalent, Doppler-domain and time-domain approaches are suitable for different system scenarios. The Doppler-domain algorithm can be chosen for systems operated with constant PRI schemes or periodic PRI variation schemes. Compared to time-domain algorithms, the Doppler-domain approach is computationally less taxing. On the other hand, it may fail due to the ill-conditioned sampling, especially for systems with periodic PRI variation schemes because of the increase in the number of the channels. Time-domain approaches can deal with both constant and irregular sampling schemes, and are more robust when dealing with ill-conditioned sampling. As hinted, the main disadvantage of time-domain approaches is the computational time, which may be circumvented by an efficient implementation of the approach. Note that improving the efficiency of proposed algorithms is beyond the scope of this thesis, but it will be addressed as a follow-up work.

Chapter 5

Sampling and Constellation Analysis

A distributed SAR system utilized for high-resolution wide-swath imaging where every unit works with a pulse repetition frequency (PRF) under the Nyquist rate ($f_{Nyquist}$) requires an azimuth reconstruction step to recover the unambiguous Doppler spectrum before the SAR image formation can take place. Chapter 3 established the background for exact reconstruction approaches and Chapter 4 introduced several accurate reconstruction algorithms working either in the Doppler domain or in the time domain, which are valid for both single- and multi-platform HRWS mode SAR systems with constant and varying PRI schemes. The aim of this chapter is to derive a realistic multistatic constellation allowing kilometric along-track baselines for future mission scenarios, enabling very high-resolution data acquisitions over large swaths considering the current orbit control accuracies. The usability of a varying PRI scheme on the sampling instabilities in multistatic constellation is analysed, and based on this analysis, an L-band system with 1.5 m resolution over 300 km swath is suggested.

This chapter is structured as follows. Section 5.1 introduces the considered system architectures, Section 5.2 investigates the orbit control requirements for multistatic SAR constellations in azimuth and Section 5.3 presents a thorough investigation on the impact of PRI variation schemes over the sampling condition. Section 5.4 analyses the reconstruction performance with different PRI variation schemes, and then, based on the outcomes of the reported investigations, proposes an L-band constellation. Section 5.5 finally closes the chapter with a discussion.

5.1 System Overview

Figure 5.1 shows two possible realizations of multistatic SAR along-track constellations, corresponding to a semi-active configuration with one-Tx and all-Rx satellites (top) and a fully-active configuration with all-Tx/Rx satellites (bottom), both typically operated below the Nyquist PRF imposed by the antennas.

In the semi-active case, a set of receivers collect the echoes corresponding to the signal transmitted by a single satellite, and the unambiguous reconstruction of the data is done using the echoes of all receivers. In the fully active case, the echoes are collected by the same satellite, also operated under its Nyquist frequency, and the unambiguous reconstruction of the data is done using the echoes collected by the different satellites. This configuration is referred to as the pursuit monostatic acquisition mode, where the baselines are quite large such that there is no common bandwidth between different receivers. The distinction is intended to be canonical and other operation modes can be thought of from the combination of the former

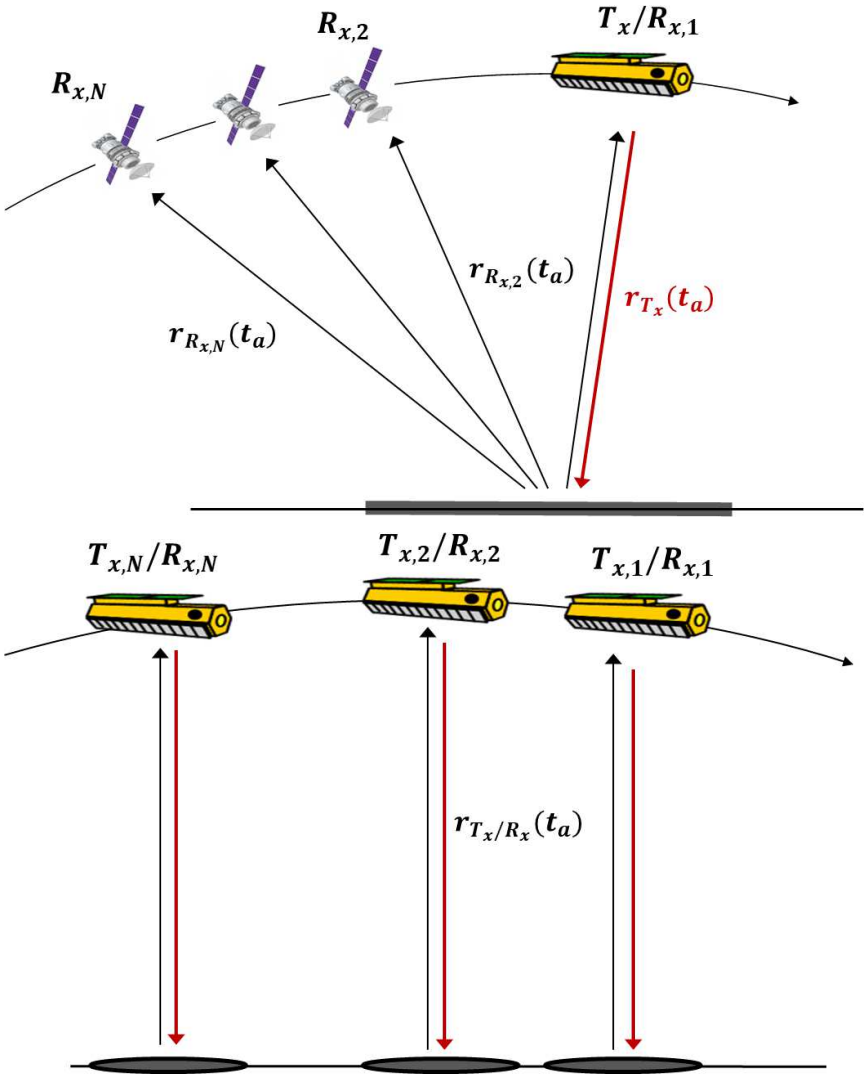

FIGURE 5.1: Along-track distributed SAR constellation geometry: (top) semi-active multistatic SAR with one Tx and all Rx sensors, (bottom) fully active with all Tx/Rx sensors (pursuit monostatic mode).

two. There are many conclusions which could be derived at system level from the basic architectures presented below. The chapter will however only focus in the fact that the semi-active case shows better efficiency, but the reconstruction needs to account for the different observation geometries of the elements of the constellation.

5.2 Orbit Contol

As discussed in Chapter 3, the position of the elements of the multistatic constellation plays a fundamental role in the feasibility of the data reconstruction and the successful retrieval of the unambiguous Doppler bandwidth and consequent suppression of azimuth ambiguities. For an optimum reconstruction performance, the equivalent phase center of each transmit/receive pair must be displaced by the multiples of v_s/PRF in the along-track direction (Krieger, Gebert, and Moreira, 2004b), which ensures a uniform sampling, and a zero across-track baseline. However, this condition in high-resolution systems implies very stringent orbital tubes with an accuracy of less than one meter, very challenging to achieve by the current state of the technology. Deviations in the along-track position of the spacecraft may result in ill-conditioned sampling. Deviations in across-track may result in time- and range-variant reconstruction errors which can be interpreted as a topography-dependent model mismatch. Some of the state-of-the-art reconstruction methods can deal with the nonuniformity (Krieger, Gebert, and Moreira, 2004b), (Gebert, Krieger, and Moreira, 2009), (Sakar et al., 2020a), (Cerutti-Maori et al., 2014a), (Sikaneta, Gierull, and Cerutti-Maori, 2014) while retrieving the entire Doppler spectrum, but the reconstruction in case of coinciding samples can be achieved by smartly filtering out the redundant channels from the reconstruction at the expense of resolution loss (Cheng et al., 2017), (Liu and He, 2016) and (Liu et al., 2017).

Depending on the frequency band, even a small across-track baseline in the order of a few meters may result in large phase errors over mountainous regions. The topographic height change within the footprint imposes an inherent model mismatch in the reconstruction process, resulting in phase errors and ambiguities. Figures 5.2 and 5.3 show the effect of a 5 m across-track baseline with a 300 m of topography gradient on the reconstructed point target at L band and X band, respectively. As in Section 3.2, a two-receiver constellation with approximately uniform sampling is chosen to isolate the impact of the topography-dependent model errors. The data from the first receiver correspond to the downsampled reference monostatic signal and the data from the second receiver contain the remaining half of the Nyquist-sampled signal, which incorporates a model mismatch. The phase error at the edges of the spectrum in an X-band system reaches up to 60 degrees, whereas an L-band system is less affected with phase errors up to 12 degrees. Since only the passive receiver has a constant phase error in the example, the phase profile of the reconstructed data shows jumps. The average phase error appears at the maximum of the IRF and also results in azimuth ambiguities. These results corroborate the hypothesis presented in Subsection 3.3.4 that the current state of technology seems to convey the idea that the implementation of multistatic SAR along-track constellations seems to be more feasible in the case of systems operating at lower frequencies with good to moderate resolution.

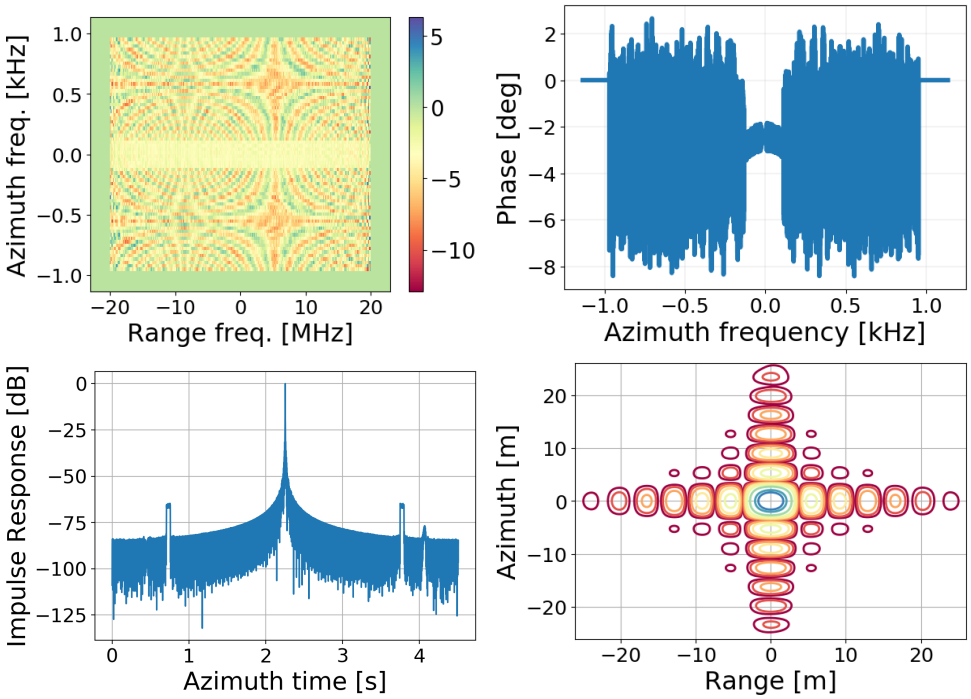

FIGURE 5.2: Point target reconstruction results with $\delta h = 300\,\text{m}$ for an L-band, 15λ azimuth resolution system with an across-track baseline of $b_{xt} = 5\,\text{m}$ (top-left): phase error, (top-right): phase error cut in the Doppler domain with $f_r = 0$ Hz, (bottom-left): azimuth point target response showing the ambiguities, (bottom-right): contour plot of the impulse response function.

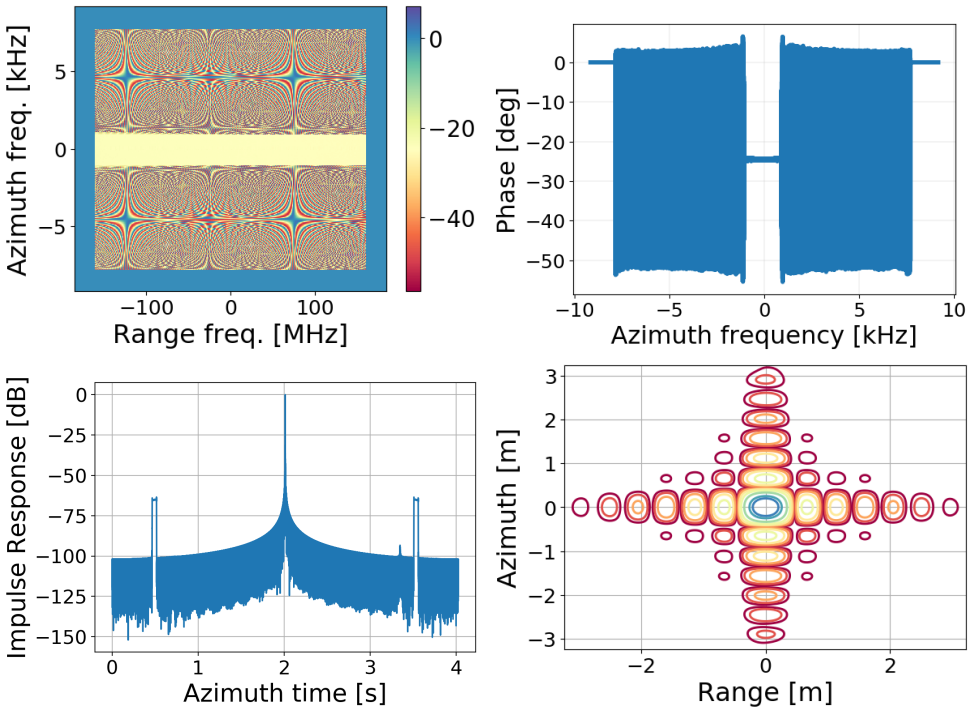

FIGURE 5.3: Point target reconstruction results with $\delta h = 300\,\text{m}$ for an X-band, 15λ azimuth resolution system with an across-track baseline of $b_{xt} = 5\,\text{m}$ (top-left): phase error, (top-right): phase error cut in the Doppler domain with $f_r = 0$ Hz, (bottom-left): azimuth point target response showing the ambiguities, (bottom-right): contour plot of the impulse response function.

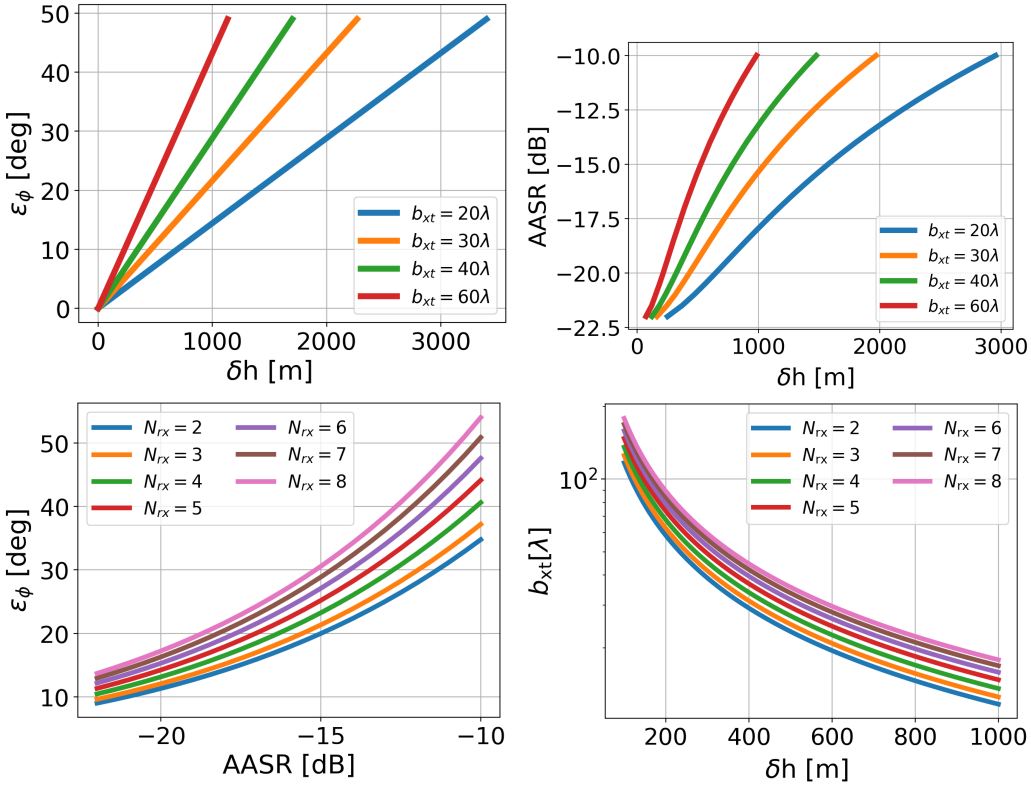

FIGURE 5.4: Orbit control sensitivity of X-, C-, S- and L-band SAR systems: the impact of across-track baseline in terms of the phase error and AASR. Top plots show the phase error due to the model mismatch (left) and resulting AASR (right) for different orbital tubes with respect to the topographic height variation in azimuth. Bottom plots show the phase error and AASR relation for different constellation sizes (left) and requirement on the across-track baselines (right).

Reformulating Eq. (3.36) within the current system design framework, the orbital tube imposed on the elements of the constellation can be approximated as

$$b_{\text{xt}} \approx \frac{\epsilon_\phi(\text{AASR}, N_{\text{rx}})}{2\pi} \frac{2\lambda r_0 \sin\theta_{\text{i}}}{\delta h}, \tag{5.1}$$

where ϵ_ϕ is the maximum phase excursion which can be tolerated within the elements of the constellation. As indicated in the notation, the value of ϵ_ϕ is a design parameter which depends on the AASR value of the specification and the number of spacecraft in the constellation.[1]

Figure 5.4 shows the impact of the across-track baseline as a function of the phase error and the corresponding AASR with respect to the topographic variation δh within the scene. For the analysis, the across-track baseline is defined in terms of wavelength, which brings a natural comparison between different carrier frequencies. The top plots have been computed assuming a constellation of two satellites, with a reference Tx/Rx unit (zero across-track baseline) and an Rx unit whose across-track baseline ranges from $20\lambda - 60\lambda$. As expected, the phase error

[1]Note that the bistatic range history with an across-track baseline can be approximated as $r_i(t_{\text{a}}, b_{xt}; r_0) \approx r(t_{\text{a}}) + r_0 + \delta r_0(b_{xt}) + \frac{v_{\text{s}}^2 t_{\text{a}}^2}{r_0 + \delta r_0(b_{xt})}$, where $r(t_{\text{a}})$ is the monostatic range history defined in Eq. (2.10). The topography-dependent model mismatch is independent of azimuth resolution, since the model mismatch does not introduce a linear error and the quadratic error becomes negligibly small due to relatively short across-track baselines in multistatic SAR concepts [$\delta r_0(b_{xt}) \ll r_0$].

(top left) and resulting AASR (top right) increase linearly with the topographic variations and across-track baselines. A topographic variation of one kilometer with a 20λ (5 m at L-band and 0.6 m at X-band) across-track baseline results in a phase error of 15 degrees and an AASR of -17.5 dB. An increase in the number of receivers increases the number of sub-bands and consequently the number of ambiguities. The bottom-left plot illustrates the relation between the phase error and AASR for different constellation sizes. Note that all receive-only units are assumed to have the same across-track baseline. Despite the increased number of ambiguities, larger constellations are less sensitive to the topographic variations and the total AASR degradation is inversely proportional to the number of satellites. The reason for this is the decrease in the power of each ambiguity. This analysis may serve as a system design tool for computing the requirement on the orbital control accuracy by using Eq. (5.1). The bottom-right plot shows the requirement on the orbital tube for constellation sizes ranging from two to eight for AASR values better than -20 dB, for the case of a near incidence of 20 deg and an orbit height of 514 km.[2] Analogously to the along-track case, the requirement on the orbital tube becomes more stringent for higher frequencies. Note that this requirement may be relaxed for higher orbits and smaller swaths (with larger incidence angles). In the presented analysis, however, a threshold between 10 and 20λ, covering topographic variations up to 1-2 km, represents an acceptable compromise for global applications.

To put these numbers in perspective, results from the PRISMA mission (D'Amico et al., 2013) report control accuracies for small baseline scenarios in along-track and across-track better than 16 and 5 meters, respectively. The latter value seems to be aligned with the orbital tube requirement for L-band constellations, but off by an order of magnitude for C-band and X-band systems. With respect to the along-track requirement, roughly a fraction of the antenna size divided by the number of receivers, the results reported with PRISMA seem to be by more than one order of magnitude off.

5.3 The Use of Variable PRI Schemes

For the cases in which the control of the along-track position of the spacecraft exceeds the requirement in Eq. (5.1), the use of variable PRI schemes (changing the time interval between consecutive pulses continuously) is expected to help with the occurrence of coinciding samples and the ill conditioning of the reconstruction process. As mentioned in Subsection 3.1.1, the effective input sampling in azimuth is determined by the receiver phase centers and the operational PRF, and the desired output sampling (uniform sampling grid) is determined by the final system PRF (PRF_0). Figures 5.5-5.7 show the sampling condition in a circular form (top) and its equivalent on the azimuth time axis in a linear form (bottom) for a constant PRI scheme, and a varying PRI scheme without and with coinciding samples, respectively. [3] As long as the relative distance between the transmitter and the receivers in the orbit are stationary, the PRI scheme (constant, randomly varying or linearly varying) does not change the relative sampling condition. However, the PRI variation changes the start of each sampling cycle and prevents the periodic occurrence

[2] A near incidence of 20 deg from this orbit height combined with far incidences of 50 or 60 deg results in around 370 or 570 km swaths, respectively.

[3] It is common in the literature to represent the sampling condition linearly with the time axis. However, the circular representation illustrates better the periodicity of the sampling condition and shows clearly the position of the available input samples (received pulses) in the vicinity of each output sample. Therefore, each sampling condition is represented with both circular and linear forms.

of the poor sampling within the footprint, which represents the main contribution of a varying PRI scheme. Note that the coinciding sampling cannot be resolved by anything other than drifts in the orbit (expressed as δb_i in the figures).

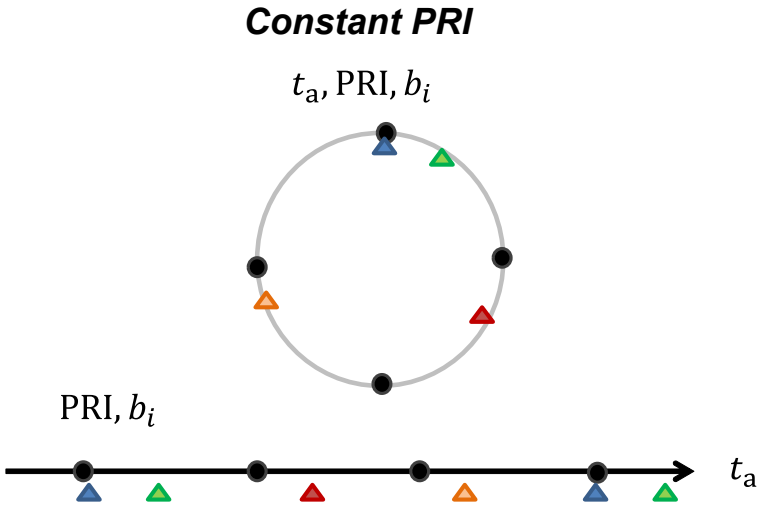

FIGURE 5.5: Non-uniform sampling scheme with constant PRI. The colored triangles represent the input (received) data sampling positions and the black points represent the uniform output sampling grid.

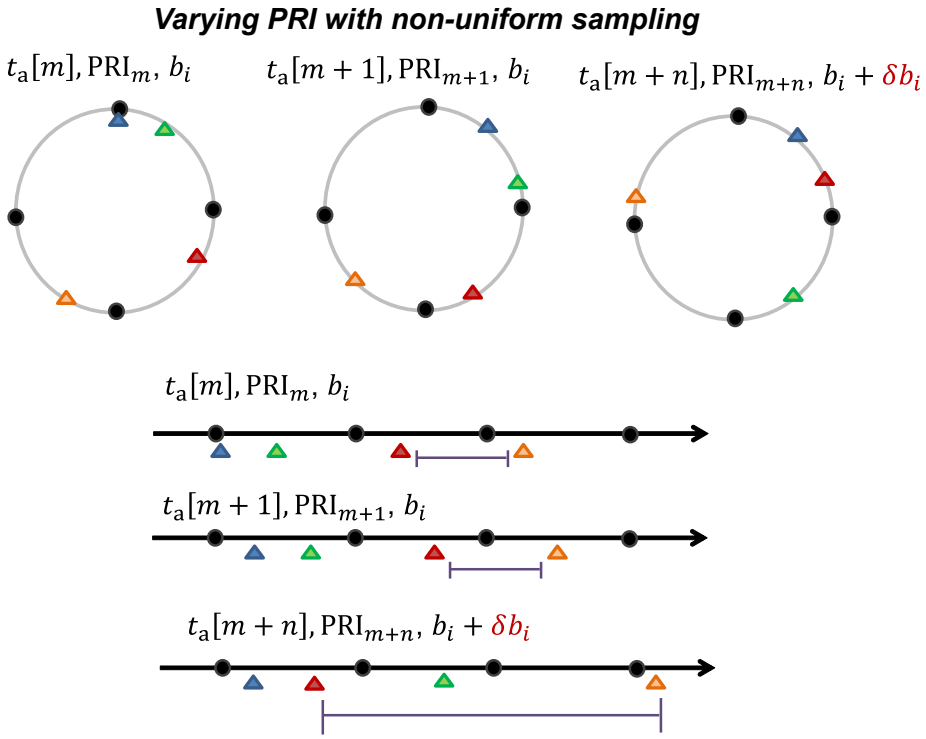

FIGURE 5.6: Non-uniform sampling scheme with random PRI at three time instants showing the relocation of the samples in the sampling circle and azimuth time axis, and the possible change in the relative distance between the samples due to drifts within the orbital tube. The colored triangles represent the input (received) data sampling positions and the black points represent the uniform output sampling grid.

Figure 5.8 illustrates the improvement caused by a randomized sampling scheme when compared to a regular one with coinciding samples by showing the azimuth

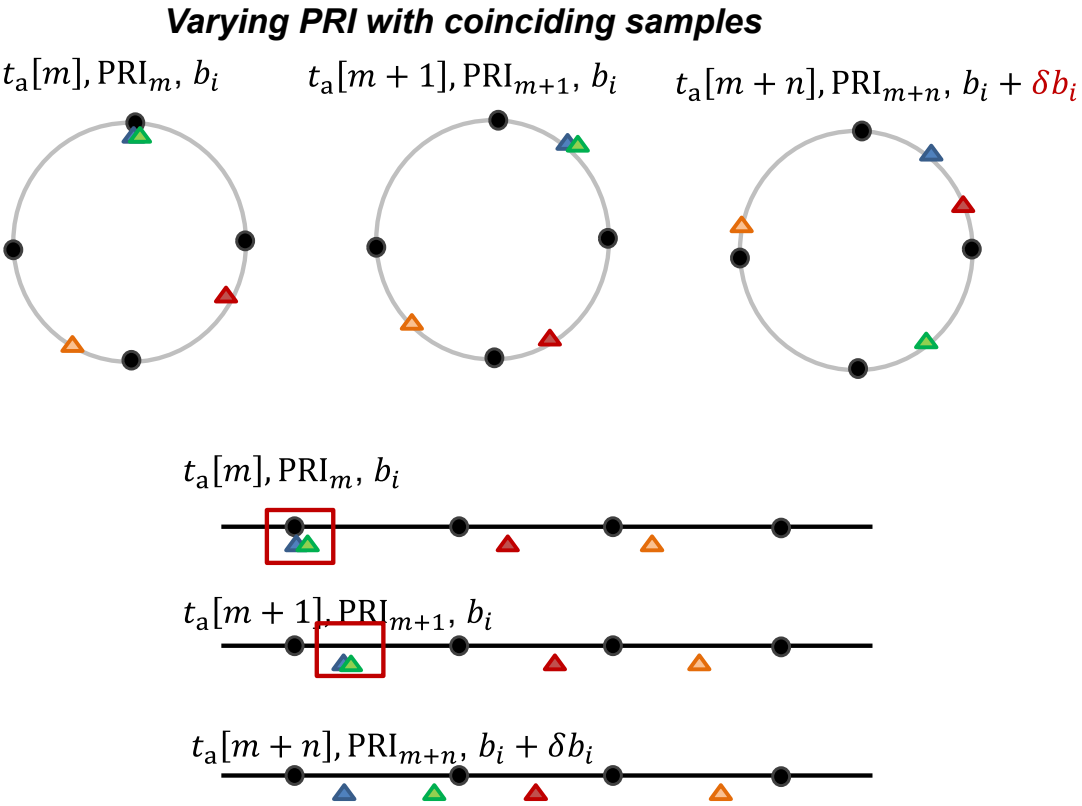

FIGURE 5.7: Coinciding sampling scheme with random PRI at three time instants showing the relocation of the samples in the sampling circle and azimuth time axis, and possible change in the relative distance between the samples due to drifts within the orbital tube. The colored triangles represent the input (received) data sampling positions and the black points represent the uniform output sampling grid.

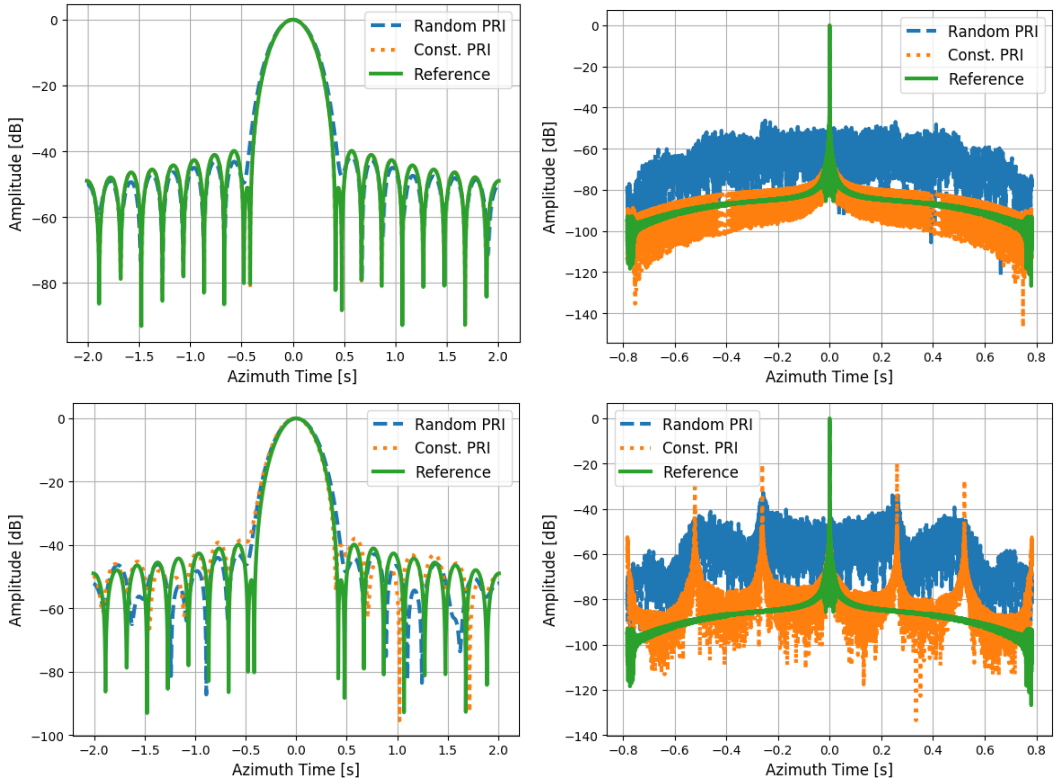

FIGURE 5.8: Zoomed impulse response function (left) and impulse response function (right) of a point target with constant and varying PRI in case of uniform sampling (top) and coinciding sampling (bottom).

impulse response of an L-band multistatic SAR constellation of five satellites with 30λ resolution for a constant and a fully random PRI with uniformly distributed variations up to 20%. The top plots show the zoomed impulse response function (left) and the full impulse response function (right) for uniform sampling whereas the bottom plots show the same results for a coinciding sampling condition with four available receivers. Both the degradation and the improvement of the random PRI scheme with respect to the well-conditioned and ill-conditioned sampling scenarios are noticeable, with a clear improvement of the ambiguity rejection capabilities of the system.

The straightforward solution for improving the sampling scheme without causing the use of larger antennas or multi-channel architectures is the increase of the sampling rate of the constellation, either by raising the PRF of operation, which results in a reduction of the unambiguous swath, or by the use of a larger number of receive satellites. Without loss of generality, the following section investigates SAR constellations providing an azimuth resolution of δ_{az} and a (slant) swath width of W_{s} that results from upscaling the unambiguous (slant) swath width corresponding to the PRF of operation ($W_{\mathrm{s},0}$) by a factor of system scaling η_{ss}. In general, the constellation will require a number of receiving satellites larger than system scaling

($N_{rx} > \eta_{ss}$), i.e.,

$$W_s = W_{s,0} \cdot \eta_{ss} \tag{5.2}$$

$$\text{PRF} = \frac{\text{PRF}_0}{\eta_{ss}} \tag{5.3}$$

$$N_{rx} = \eta_{ss}(1+\alpha) \quad \text{with } \alpha > 0, \tag{5.4}$$

where α can be interpreted as the oversampling factor by means of number of receivers. The purpose of the analysis in this chapter is to characterize the value of the oversampling factor α for realistic multistatic SAR constellations. This characterization is done numerically by means of a Monte-Carlo analysis conducted with simulated data further processed with practical implementations of reconstruction algorithms (introduced in Section 4.2) and SAR processing algorithms, both working in the time and range-Doppler domains. In the case of a variable PRI scheme, the variation will be controlled using a margin parameter m, i.e.,

$$\text{PRI} \in \frac{1}{\text{PRF}} \left[1 - \frac{m}{2}, 1 + \frac{m}{2}\right]. \tag{5.5}$$

Let us start by looking into the number of valid samples as a function of the sampling characteristics. Validity in this case is defined as the percentage of the output regular grid samples that have at least one irregular input sample in the vicinity of one azimuth antenna length. Figure 5.9 shows the percentage of valid samples as a function of the oversampling factor for constant and uniformly distributed random PRI schemes with margins varying from 10% to 30%. The solid lines represent the mean values whereas the vertical bars correspond to the standard deviation.

The left and right figures correspond to the simulations with a factor five and ten of the Nyquist PRF of the transmit antenna, i.e., system scaling η_{ss}, at X-band, C-band, S-band and L-band, respectively. The positions of the receivers are random and uniformly distributed within η_{ss} output resolution cells. The curves show a similar behaviour in all cases and tend to saturate for increasing values of oversampling factor. As expected, the results are independent of the carrier wavelength and change mildly with system scaling. Constellations imaging larger swaths are more prone to poor sampling due to the increased probability of coinciding samples. The mean validity values are higher for the constant PRI scheme and varying PRI schemes with lower variation margins, especially for higher oversampling values. On the other hand, the standard deviation of validity is reduced when increasing the variation range of the PRI, which suggests that operating multistatic SAR constellations with variable PRI schemes keeps the system performance stable.

Although the average validity values point at a constant PRI scheme usage, varying PRI schemes prove its advantage for bad sampling conditions. To evaluate the sampling validity fairly, it is necessary to take a look at the worse case scenarios with respect to the ones presented in the analysis above. Figure 5.10 shows the 3σ values of Monte-Carlo simulation as a function of the oversampling factor with a system scaling of five and ten for the systems in interest, namely, S-band (top) and L-band (bottom). As expected, all varying PRI schemes guarantee better sampling when compared to the constant PRI scheme, especially for lower oversampling factors, and lower range of PRI variations yield better sampling for increasing oversampling factors. The outcomes of this analysis support the hypothesis of operating multistatic SAR constellations with variable PRI schemes whenever overall sampling (i.e., operation PRF, azimuth resolution, and number of receivers) approaches Nyquist if the

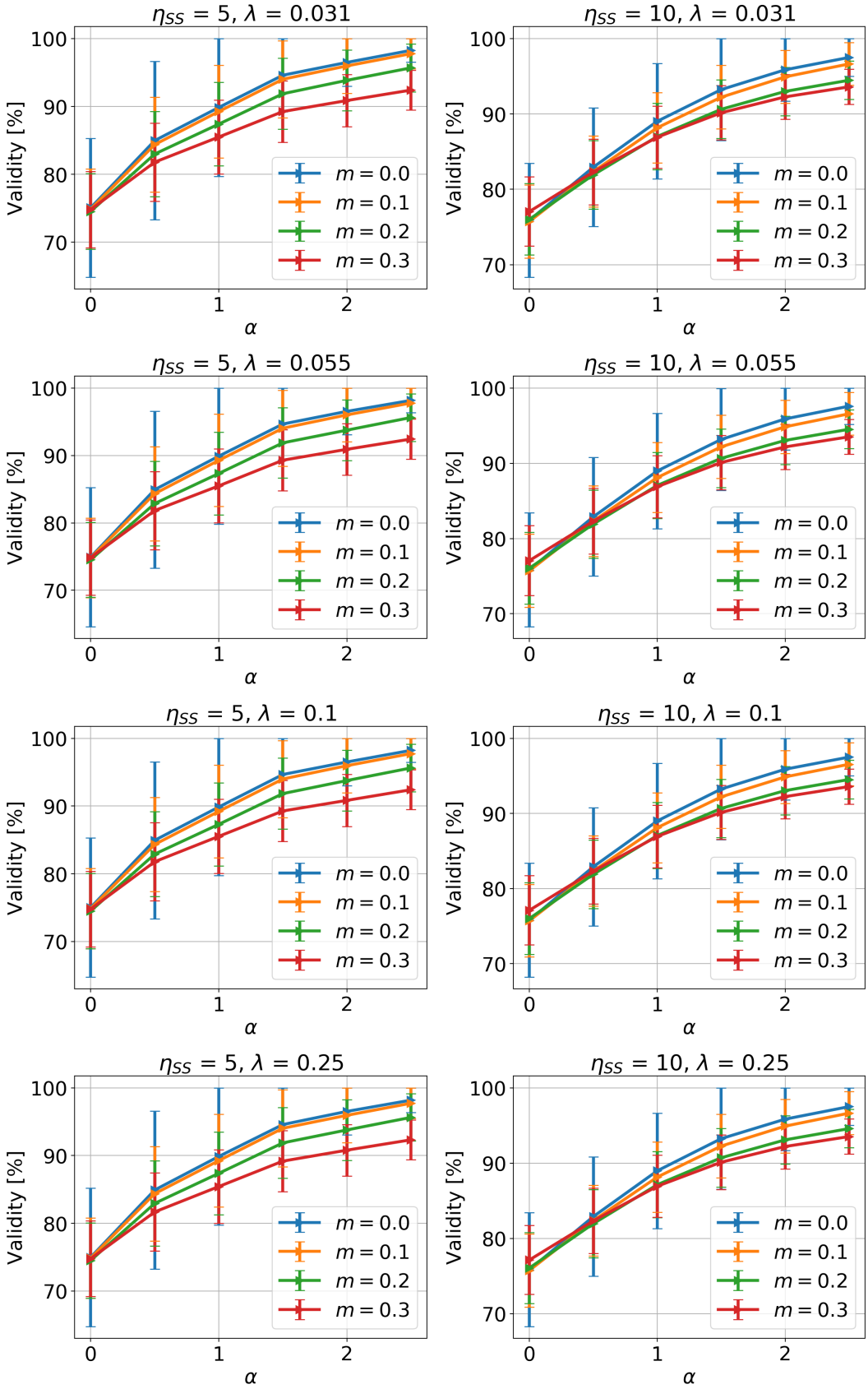

FIGURE 5.9: Monte-Carlo analysis of the percentage of the recoverable output samples with 500 iterations for 30λ resolution with system scaling of five (left) and ten (right) at X-band, C-band, S-band and L-band, respectively. The solid lines show the mean values and the vertical lines represent the standard deviation.

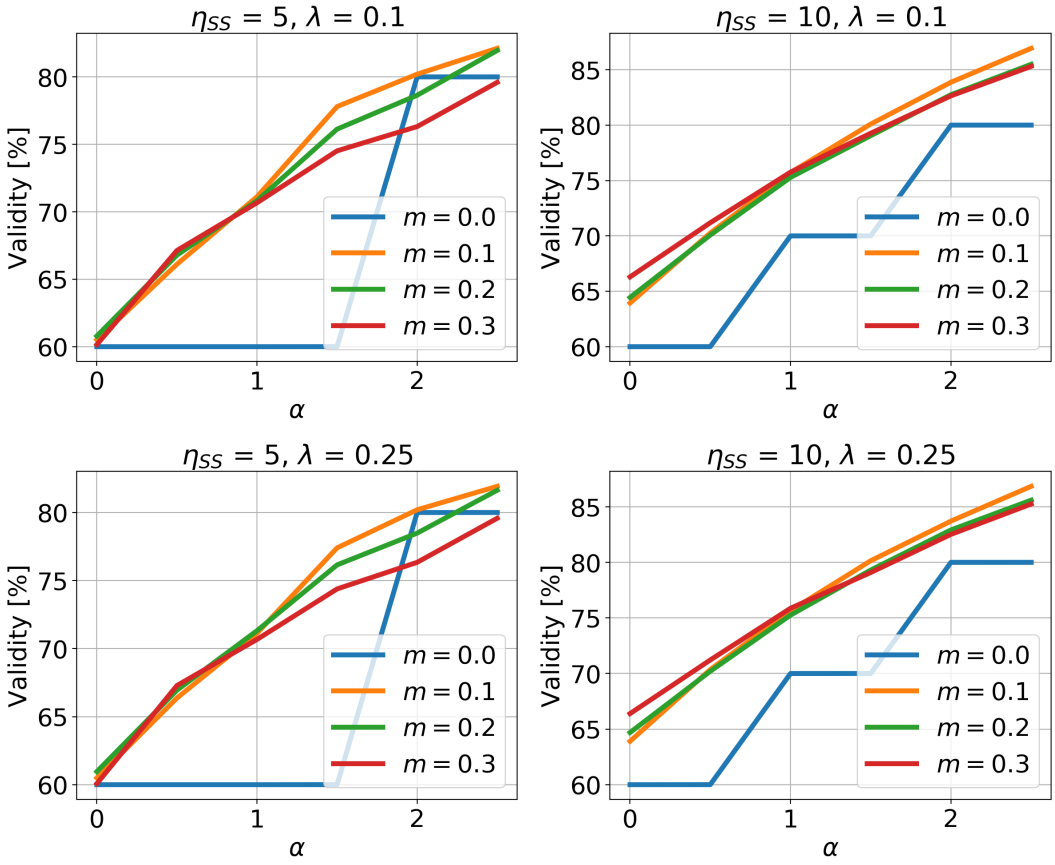

FIGURE 5.10: Monte-Carlo analysis of the recoverable output samples with 500 iterations for 30λ resolution in S-band (top) and L-band (bottom) with system scaling of five (left) and 10 (right). The plots show the percentage of the valid samples for the worst sampling case (3σ).

orbit control accuracy does not meet the requirements discussed in Subsection 5.2.

5.4 System Analysis

The analyses above and in Section 5.2 have shown that multistatic SAR constellations require very precise orbit control, with increasingly stringent requirements for higher frequencies and better resolutions. Displacement of the sensors in along-track may cause the ill-conditioning of the azimuth sampling, making the recovery of the entire Doppler band impossible. A possible solution already hinted above is the combination of an increase in the number of receivers ($N_{rx} > \eta_{ss}$) with the use of a variable PRI scheme. Displacement of the sensors in across-track direction cause the raise of ambiguities caused by reconstruction model mismatch, even more relevant in the case of scenes with strong topographic variations. As shown in Section 5.2, the sensitivity with topography decreases for lower frequencies.

The current section aims at providing a sensitivity analysis to show examples of feasible multistatic SAR constellations in along-track exceeding the imaging capabilities of current systems. It is chosen to focus on lower frequency constellations (e.g., L-band and S-band) because of two main reasons: i) the orbital tube requirements appear technologically attainable, and ii) the improvement of azimuth resolution comes associated with a reduction of the antenna size which may allow for the use

of smaller platforms. Since the reconstruction performance highly depends on the sampling condition which is a dynamic parameter, the analysis has been conducted by using a Monte Carlo approach.

Figures 5.11 and 5.12 show the mean and standard deviation of the Monte Carlo analyses over 300 iterations in terms of AASR with respect to oversampling in number of receivers for PRI variation margins ranging between 0% and 30% in the case of S-band and L-band constellations, respectively. The azimuth ambiguities of systems with a constant PRI appear in the focused image at the shifted intervals of (Curlander and McDonough, 1991)

$$\Delta x_{az} = \pm \frac{PRF \lambda r_0}{2 v_{eff}^2} v_g \tag{5.6}$$

as localized artifacts. However, the ambiguities of the systems with a varying PRI scheme appear in the image as a noise-like disturbance. Therefore, the AASR is computed from the simulated data as defined in (Villano, Krieger, and Moreira, 2014), i.e.,

$$\text{AASR} = 10 \log_{10} \left(\frac{P_{\text{sl}} - P_{\text{sl,ref}}}{P_{\text{ml}}} \right) \tag{5.7}$$

where P_{sl} and P_{ml} are the sidelobe and mainlobe power, respectively, and $P_{\text{sl,ref}}$ is the sidelobe power for an ideal response. The sidelobe powers have been computed within three integration time lengths (± 1.5).

The resolution of the system is set to 30λ in all cases, but as expected any major impact of the resolution, other than the accuracy of the reconstruction and more stringent requirements on orbit control in the along-track direction, has not been observed. It goes without saying that the reconstruction performance improves with the increasing values of α in all cases. The parameter system scaling has been set to five and ten for the left and right plots, respectively. And as expected too, increasing values of system scaling seem to require higher oversampling due to the increasing susceptibility for a poor sampling condition. The top and middle plots show the reconstruction performance of semi-active constellations with random and linear PRI variations, respectively, while the bottom plots show for the sake of comparison the behaviour of fully-active constellations with random PRI variations. Note, however, in all cases the blue dashed-dotted line corresponds to a constant PRI case. The black dashed line represents a reference value of -22 dB.

In all cases, the use of a variable PRI scheme provides more stable performance, with a smaller standard deviation for larger margins in the case of interest for values of oversampling factor between 0 and 1. Another outcome of the analysis is that an increasing oversampling factor also increases the standard deviations. The reason for this is the possibility of well conditioned sampling as well as the coinciding sampling condition increases with increasing number of receivers. Nevertheless, despite the standard deviation extent, the worst possible performance of a system with high oversampling values is still better than the one with lower oversampling factors. The random variation shows slightly better ambiguity rejection capabilities than the fast linear PRI variation, especially for larger margin of PRI. In All-Tx/Rx configuration, the mean AASR for different values of margin remain similar, where similar to the one-Rx/all-Tx configurations the standard deviation increases for larger oversampling factors. As hinted above, increasing the value of η_{ss} (right plots) increases the ambiguity levels due to an increase in the number of overall channels and spectral copies. The S-band and L-band performance plot trends with respect to the oversampling factor and PRI margin agree quite well, with a difference of better AASR

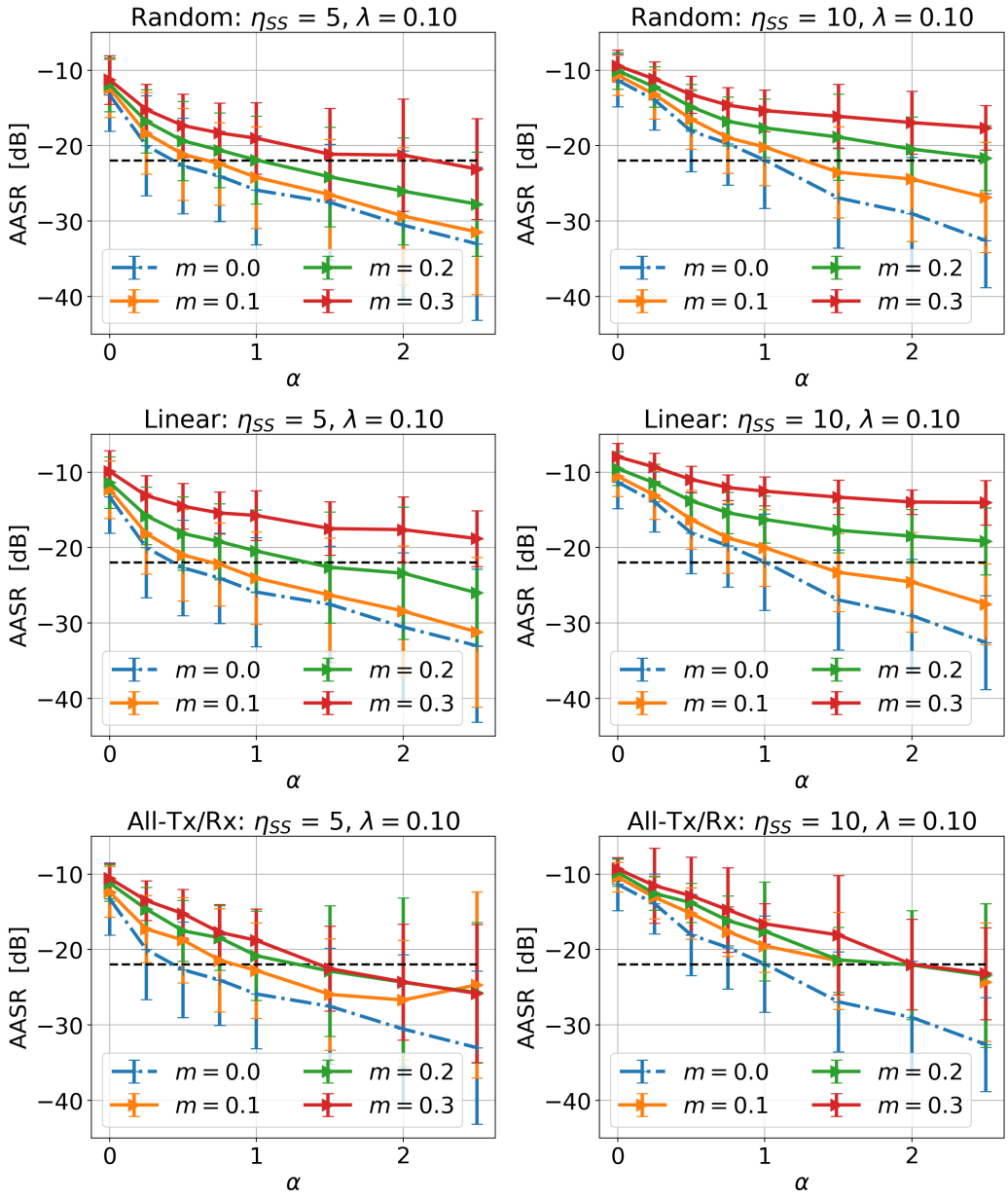

FIGURE 5.11: Reconstruction performance for a system scaling of 5 (left) and 10 (right) in terms of mean and standard deviation of AASR with different PRI variation margins in S-band. The number of the receiving satellites are $N_{\text{rx}} = (1 + \alpha)\eta_{\text{SS}}$. (Top): One-Tx/all-Rx configuration with random PRI variation, (middle): Semi-active configuration with linear PRI variation, (bottom): Fully-active configuration with random PRI variation.

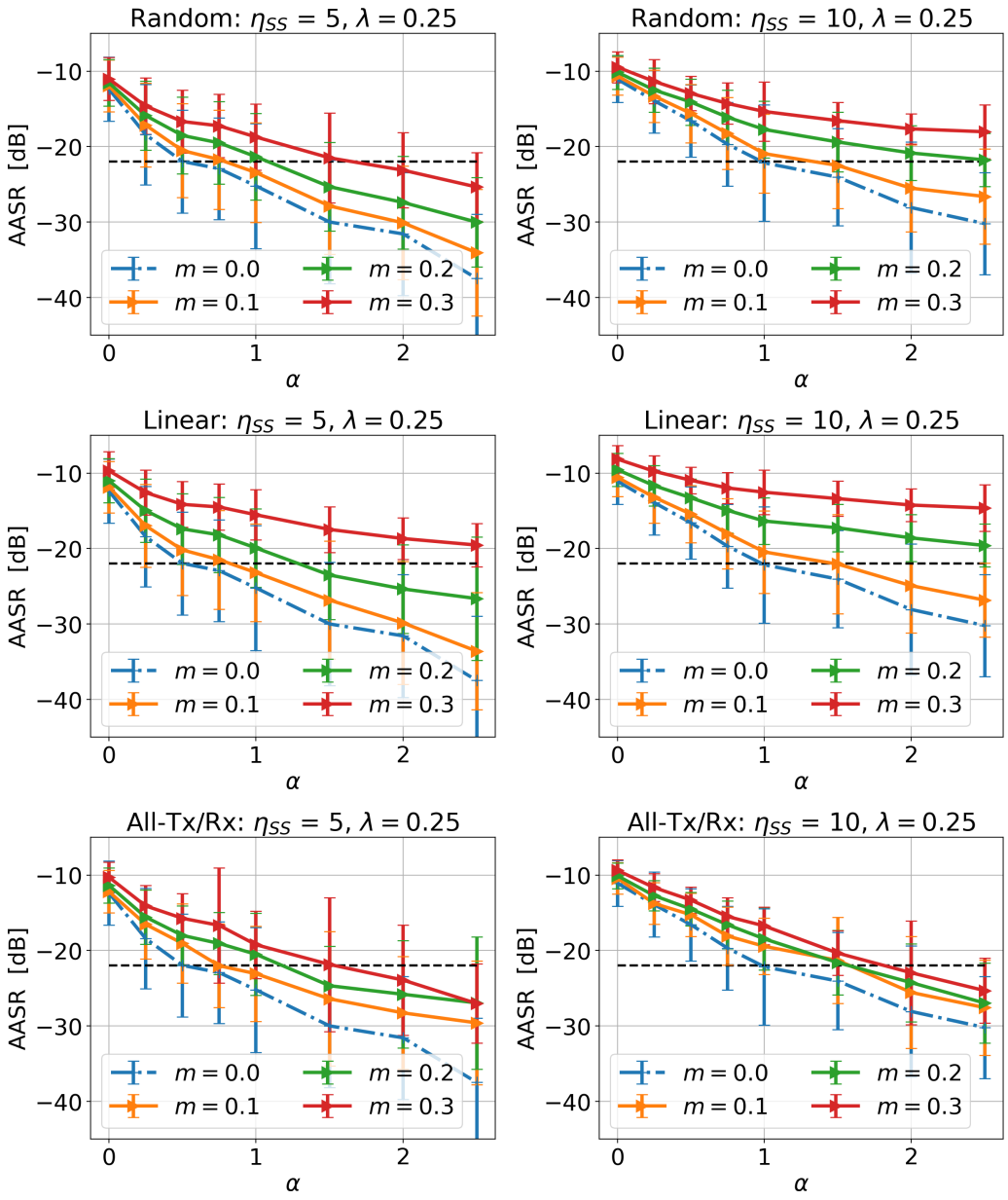

FIGURE 5.12: Reconstruction performance for an L-band multistatic constellation with η_{ss} values of 5 (left) and 10 (right) in terms of mean and standard deviation of AASR with different PRI variation margins in L-band. The number of the receiving satellites can be computed as $N_{rx} = (1 + \alpha)\eta_{ss}$. (Top): Semi-active configuration with random PRI variation, (middle): Semi-active configuration with linear PRI variation, (bottom): Fully-active configuration with random PRI variation.

TABLE 5.1: L-band Exemplary System Design Parameters

Mission performance requirements		
Parameter	Symbol	Value
Wavelength	λ	0.25 m
Swath width	W_s	300 km
Azimuth resolution	δ_{az}	1.5 m
System parameters		
Orbit height	h_s	655 km
Incidence angle	θ_{min} / θ_{max}	13.6° / 35.0°
Slant range	R_0	674 km - 800 km
Mean PRF	PRF	630 Hz
PRF margin	m	0.1
Number of Rx	N_{rx}	20
Receive antenna size	l_{az}, l_{rg}	3 m x 4 m
Oversampling	α	1
Along-track baseline	b_i	$100i \pm \delta$ m

expectations at L-band thanks to the coarser resolution. All AASR results and validity plots shown in Figure 5.9 agree on the effect of the oversampling factor and PRI variation margin, namely higher margin results in lower standard deviation and lower mean value for increasing oversampling factor. This analysis with respect to the oversampling factor and the margin exhibits a compromise between the stability and the budget, and supports the usability of a PRI variation.

Based on the presented investigations, a feasible system scenario and a processing approach are suggested in the following. The goal is to image a swath width of 300 km with a geometric resolution of 1.5 m. The system parameters are summarized in Table 5.1. An L-band system is chosen to mitigate the topography sensitivity, and random PRI variation with $m = 10\%$ to avoid any periodic reconstruction artefacts. The Monte-Carlo analysis in Figure 5.12 shows that an oversampling of one and a PRI variation margin of 0.1 ensure an AASR better than -20 dB for 30λ resolution. By keeping the same PRI variation parameters, a system with five times better resolution is expected to deliver slightly worse and yet acceptable performance. With the parameters listed in Table 5.1, another Monte-Carlo analysis of the 1D point target reconstruction with 100 iterations is performed. The time-domain reconstruction is done as explained in 4.2. The PRI sequence as well as the sampling condition are randomly determined for each simulation iteration. Figure 5.13 shows the zoomed impulse response function (left) and the full impulse response function (right) of a reconstructed and focused point target at near range (top), mid range (middle) and far range (bottom) with $N_{rx} = 20$. The results additionally prove that the proposed reconstruction method can remove the geometry-related phase variation very well besides the regularization of the input data. The mean performance parameters, namely, PTAR, PSLR, ISLR and AASR, are shown in Table 5.2 accordingly. Note that the computation of the AASR includes the entire noise-like disturbance outside of the mainlobe. The reference values represent the performance values of a monostatic system with the same azimuth resolution. The average AASR of the system remains around -20 dB, which is a small price for the sake of a low PTAR and PSLR.

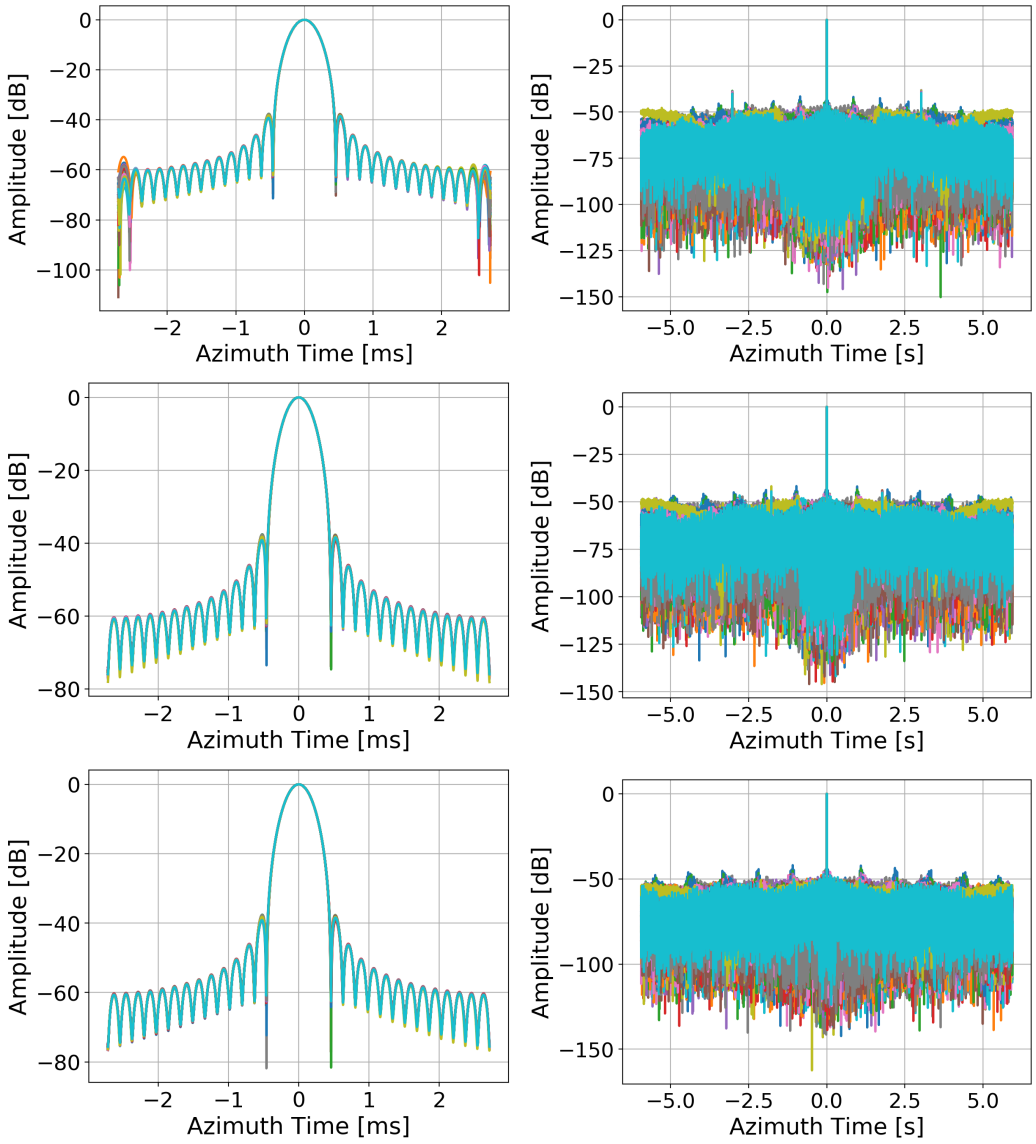

a) Zoomed impulse response function, b) Full impulse response function

FIGURE 5.13: Monte-Carlo analysis with 100 iterations. Reconstructed and focused point target impulse response at near range (top), mid range (middle) and far range (bottom) with the system parameters listed in Table 5.1.

TABLE 5.2: Mean performance parameters of the example system in L-band ($\alpha = 1$ and $N_{rx} = 20$)

	Near range	Mid range	Far range	Reference
PTAR	-38.63 dB	-38.38 dB	-38.39 dB	-38.16 dB
PSLR	-38.64 dB	-38.40 dB	-38.41 dB	-38.18 dB
ISLR	-18.43 dB	-19.20 dB	-19.56 dB	-25.34 dB
AASR	-19.45 dB	-20.56 dB	-20.92 dB	-26 dB

5.5 Conclusion

The performance of the multistatic SAR reconstruction fairly depends on the sampling condition determined by the PRF and the relative position of the receiving platform with respect to the transmitter. In spite of the accurate reconstruction approaches presented in Chapter 4, the available orbit control technology cannot ensure good sampling conditions that fully avoid redundancy, hence, forcing the usage of auxiliary receivers. The goal of this chapter was to derive a realistic constellation for future mission scenarios. The usability of a varying PRI scheme in terms of sampling condition and reconstruction performance have been analysed in several practical cases. The analysis showed that a PRI variation may improve the sampling condition and reconstruction performance, and the best PRI variation margin depends on the oversampling factor. Higher PRI margins are better fit for low oversampling factors, while oversampling factors larger than one require a lower PRI variation margin. Finally, an exemplary distributed L-band SAR constellation in along-track has been investigated and the reconstruction performance has been verified based on a Monte-Carlo analysis. The results have supported the mission parameters suggested by the sensitivity analysis, and showed that the suggested time-domain algorithm achieves accurate reconstruction with high-resolution systems, kilometric baselines, and over areas of hundreds of kilometers.

Chapter 6

Conclusion

This chapter provides an overview of the contributions (Section 6.1) and the obtained results (Section 6.2) of this work. In addition, Section 6.3 gives an outlook of further research topics.

6.1 Thesis Objectives

Synthetic Aperture Radars (SARs) are very popular instruments for spaceborne remote sensing offering a large range of applications for Earth monitoring and planetary exploration. Not only does SAR provide high-resolution, day-and-night and weather-independent images, but also many polarimetric and interferometric tools for the retrieval of qualitative and quantitative physical information of areas of interest. In recent years, there has been an increasing interest in high-resolution SAR data with short temporal baselines to study the dynamic processes of the Earth. As discussed in Chapter 2, the conventional SAR, however, faces a fundamental trade-off in terms of the maximum resolution and swath width that can be achieved simultaneously, resulting in the impossibility to deliver high-resolution data on a global scale with a short temporal baseline.

To overcome the inherent limitation of SAR, numerous innovative high-resolution wide-swath SAR imaging modes and processing techniques have been proposed in this thesis (Chapter 3), all essentially based on a multi-aperture reception scheme. Next-generation spaceborne SAR systems aim at very high-resolution imaging with short temporal baselines by utilizing both new modes and processing techniques. The additional receive units in multi-aperture systems can be obtained by either splitting the transmit antenna in azimuth and/or in elevation when receiving, i.e., multi-channel, or deploying multiple receivers on different platforms, i.e., multistatic. One viable realization of such a concept is distributed SARs with along-track baselines operated under the Nyquist frequency, offering the potential of flexible observation geometries and enhanced performance with reduced sensor complexity and costs. In such a system, since the echoes of the individual receivers appear aliased, the recovery of the unambiguous Doppler spectrum via azimuth reconstruction approaches is required before SAR image formation occurs.

As discussed in Chapter 3, numerous methods for multi-channel/multistatic azimuth reconstruction exist in the literature. Depending on the optimization methodology, the shape of the reconstruction filter weights varies. However, most of these approaches essentially resemble the method in (Krieger, Gebert, and Moreira, 2004b), which is based on the generalized sampling theory (Papoulis, 1977). The validity of these algorithms rely on all channels supporting nearly the same spectrum of the scene observed and the range histories. Evidently, the existing approaches perform fairly well for small along-track separations of the phase centers, such as in

close formation SAR constellations or more likely single-platform multi-channel systems. In distributed systems with along-track baselines of a few km, the changes in the range history introduce strong polychromatic variations which are ignored in the available literature. In particular, a residual range-variant polychromatic quadratic component propagates into the reconstruction algorithm causing defocusing and a significant raise of ambiguities.

The goal of this doctoral work has been to derive a realistic distributed SAR constellation allowing kilometric along-track baselines for future mission scenarios, enabling very high-resolution data acquisition over large swaths. This goal imposes to define an accurate reconstruction method that accommodates range-variance and the polychromatic character of the reconstruction filters and to overcome time-variant sampling instabilities. The work presented in this thesis has introduced multistatic SAR with long along-track baselines, derived an accurate data model and presented several reconstruction approaches suitable for along-track multi-aperture systems ranging from single platform (multi-channel) to distributed constellations with large along-track baselines.

6.2 Summary of Results

After introducing the conventional SAR and bistatic/multistatic counterpart in Chapter 2, the first contribution is reported in Chapter 3. Due to the complex imaging geometry of multistatic SAR with large along-track baselines, the azimuth reconstruction becomes more elaborated and the analytical data model widely adopted by the methods in the literature does not suffice. Section 3.1 presented an accurate (numerically derived) signal model for along-track multistatic constellations. The shortcomings of the reconstruction algorithms in the literature were analysed with the error estimation equations derived in Section 3.2 [Eq.s (3.30), (3.31)]. This model allows for the evaluation of the model errors directly, avoiding any computational burden of the reconstruction. The impact of the geometrical approximation adopted by the methods in the literature was investigated in detail. The first examined geometrical approximation was the uncompensated Doppler rate. It has been shown that the phase error introduced by the mismatch in the reconstruction increases with increasing resolutions and baselines, limiting the use of the common Doppler rate approximation to 5 km baseline for high-resolution systems. Then the focus was turned to the coupling between range time and range frequency in the reconstruction filter. The reconstruction with the monochromatic approximation is limited to shorter baselines, of less than 1 km, while the range-invariant polychromatic reconstruction method is limited by the maximum swath width up to 5 km. This summarized analysis proved that the validity of the existing algorithms is limited to along-track baselines smaller than a few hundred meters and to geometrical resolutions coarser than 15λ.

One of the main contributions of this work was the identification of all relevant aspects of the azimuth reconstruction, which paved the way for the development of several accurate processing approaches (Section 3.3). These aspects are: 1) precise modelling of the range history deviation between the channels, 2) range time and range frequency variant transfer function, 3) reconstruction filter design taking into account range cell migration of the data, 4) orbit control as a crucial variable on the system performance, 5) tolerable maximum along-track baseline regarding the common Doppler support of all receiving channels and 6) atmospheric effects on the reconstruction performance. The items 1)-3) describe the geometrical aspects

that an accurate reconstruction method must compensate, nevertheless, the algorithms in the literature fail to incorporate them. The items 4)-6) describe design constraints for a realistic multistatic SAR constellation. In multi-aperture systems, the positions of the gathered samples determine the successful retrieval of the unambiguous Doppler bandwidth and the efficient ambiguity suppression. The sampling positions are governed by the distance between each receive unit and the transmitter and by the system PRF, which are constant design parameters in single-platform systems. In distributed systems, however, the position of each platform in the orbit can only be controlled as precise as the current technology allows for, causing the sampling condition of the constellation a time-variant problem. Very high-resolution distributed SAR systems demand very precise orbit control to avoid sampling instabilities in along-track and phase errors due to the topography-dependent model mismatch. Sections 3.3.4 and 5.2 presented an analysis on the orbital tube requirements for different carrier frequencies and showed that today's orbit control technology (within 5-10 m range) cannot accommodate the imperatively required precision (<1 m) for very high-resolution systems with short wavelengths (X-band, C-band).

For the full recovery of the Doppler spectrum, it is fundamental that the spectrum of the scene observed by all platforms covers at least the processed bandwidth of the system. Note that the bistatic observation geometry introduces a baseline- and wavelength-dependent Doppler centroid shift, which can result in non-common Doppler frequencies among the receivers (Subsection 3.3.5). The aliased spectrum clearly makes it impossible to band-pass filter the non-common bands, hence, the maximum along-track baseline must be addressed as a system design parameter. A fairly less concerning issue, the impact of the atmosphere, was addressed in the last subsection. Tropospheric and ionospheric delay variations between the platforms are a well described topic in the interferometric SAR literature. However, the impact of the atmospheric delay difference between the channels on the reconstruction was first investigated in this thesis and shown that only very high-resolution systems with along-track baselines larger than 5 km experience low to moderate phase errors, which makes the issue a second-order subject. Nevertheless, any potential phase error impairing the reconstruction performance must be corrected regardless of their magnitude.

Based on the investigations reported in Chapter 3, accurate azimuth reconstruction approaches for multistatic SAR constellations were developed and discussed in Chapter 4. The reconstruction process can be thought of an interpolation of the irregular input data to the regular output grid while correcting for amplitude and phase deviations, and it is possible to conduct the reconstruction in time domain or in Doppler domain. Due to its computational efficiency as in any other Fourier-domain processing approach, the attention has been first focused on the Doppler-domain reconstruction (Section 4.1). A two-step reconstruction approach that accommodates the polychromatic terms of the azimuth reconstruction and provides good accuracy for range blocks in the order of a few kilometers is presented. Without loss of generality, the matrix inversion filter estimator presented in (Krieger, Gebert, and Moreira, 2004b) was used as a reference of the analysis, although it can be replaced with any other approach.The geometrical aspects that the approach explicitly incorporated in the reconstruction solution were the items 1)-3) discussed above. Although this two-step reconstruction approach performed readily one order of magnitude better than state-of-the-art reconstruction algorithms, the analysis showed that residual phase deviations become crucial for systems with large swath widths. An additional step that incorporates these residual corrections in the range-Doppler domain proved to achieve accurate reconstruction for constellations with kilometric baselines over

swaths of hundreds of kilometers. Since Doppler-domain reconstruction is typically suited to regular sampling schemes, the focus was then turned to time-domain reconstruction in Section 4.2, which can naturally cope with irregular sampling scenarios with a varying PRI scheme. Two novel polychromatic time domain reconstruction methods, valid for both constant and varying PRI, have been developed in the frame of this thesis. As in the Doppler domain approach, the suggested algorithms can handle bistatic range histories and patterns, as well as the polychromatic nature of the radar echoes. The first time-domain approach (band-pass filter approach) performs monochromatic reconstruction on few overlapping band pass filtered input data for the center frequency of each range frequency block. After the reconstruction, the sub-bands are stitched together to form the complete range bandwidth. The number of blocks should be determined depending on the range resolution. The second method (bulk *a priori* phase correction) compensates the largest phase deviation term (range-time and range-frequency dependent, Doppler-frequency independent) before the reconstruction, so that the range frequency dependence of the remaining phase deviation is negligible. The accuracy of all reconstruction methods has been evaluated and verified with point target simulations.

Chapter 5 pursued the goal of deriving a realistic multistatic constellation that is capable of circumventing the shortcomings of current state of the orbit control technology. An analysis on the topography sensitivity revealed that the multistatic HRWS concept in azimuth was suitable for longer wavelength systems, such as S-band and L-band. In terms of ill-conditioned sampling schemes, the usefulness of a PRI variation scheme with respect to the oversampling by means of the receive units for two different system concepts, one-Tx/all-Rx and all-Tx/Rx, was investigated in Section 5.3. The main contribution of varying PRI schemes was the localization of ill-conditioned sampling randomly, consequently preventing high azimuth ambiguities at the expense of a higher noise floor. A more extensive PRI variation analysis was done with the Monte-Carlo method to address the azimuth time variant sampling condition properly. The results showed that the use of a PRI variation may improve the sampling conditions for lower oversampling factors (<1), but lower PRI variation margins (10%) are better suited for higher oversampling values. Building upon the investigations, an L-band system with 1.5 m resolution and 300 km swath width, acquiring high-resolution images on a global scale with a revisit time of 10 days has been proposed. The system can be realized with a 0.5 oversampling factor, employing 15 receive units, and a randomized PRI variation with 10% margin.

This thesis introduced, investigated, and validated various innovative polychromatic reconstruction techniques, including system design considerations with special focus on the requirements of distributed SAR systems with large along-track baselines. As proved with the detailed simulations, the developed algorithms represent an important asset for the realization of future HRWS imaging SAR systems based on multistatic constellations working under Nyquist. Thanks to its flexibility and cost-efficiency, multistatic SAR systems open a door to numerous SAR applications and constellation concepts. Furthermore, the developed reconstruction methods have the potential to be a fundamental resource for the data processing of future SAR systems.

6.3 Outlook

The current state of orbit technology and processing strategies allow for multistatic SAR concepts for HRWS imaging with certain constraints. Nevertheless, there is still

need for further processing strategies and concepts to overcome these limitations. In terms of data processing, unlike the Doppler-domain reconstruction approach, the time-domain polychromatic reconstruction algorithm presented in Chapter 4 is computationally expensive, especially in the case of a random PRI variation. An efficient implementation of the algorithm, possibly following a similar methodology as in fast backprojection approaches (Yegulalp, 1999; Ulander, Hellsten, and Stenström, 2003), that allows for on-board processing and data volume reduction would be a logical follow-up of this work. High-resolution data with short temporal resolution demands large data storage, downlink and ground processing capacity. A constellation with transponder like receivers forwarding the received data to the transmitter unit, referred as MirrorSAR (Krieger et al., 2018), may benefit from on-board azimuth reconstruction and volume reduction greatly. In fact, future SAR constellation concepts including MirrorSAR would appreciate even more an efficient generic reconstruction tool capable of processing multi-aperture data intakes both all-along-track and all-across-track configurations. Additionally, a post-processing algorithm correcting for the topography related model mismatch error would ease the stringent orbit control requirements for short wavelength SAR systems, extending the detail of acquired information due to its higher penetration capabilities. The reference (Kraus et al., 2019) investigates few approaches to circumvent this issue and shows that reconstruction in time-domain with nullsteering method offers promising results.

The processing approaches presented in this thesis have been validated with realistic simulation scenarios including real orbit and digital elevation model obtained from TerraSAR-X mission. Relying on the trend for HRWS mode imaging concepts, the validation of algorithms using either airborne sensors or TerraSAR-X/TanDEM-X SAR data is of interest. The proof of concept with real data requires very accurate clock synchronization and channel balancing, i.e., correction of hardware-related amplitude and phase differences between receiving units. The internal clock of each platform may experience slightly different drifts, and the signal path in the receive units may have different lengths, both resulting in uncompensated phase errors in the reconstruction. Efficient algorithms to estimate and correct for the clock drifts and channel imbalances will play an important role on the performance of multistatic SAR reconstruction and deserve a special attention. The information to calibrate the receivers can be exchanged by using calibration tones or they can be estimated from the data after coregistration. For the latter, the aliased spectrum of multistatic SAR data operated below Nyquist frequency poses a challenge for the estimation and correction of the imbalances.

Once the remaining processing and operational issues have been addressed, a distributed SAR concept will be an invaluable asset for researchers in order to study and understand the dynamic processes of the Earth. A large constellation with subclasses, each allowing for full recovery of the Doppler bandwidth, can be utilized for single-pass interferometry (along-track or across-track) or tomography. Moreover, single-pass high-resolution interferometric data with short revisit times can be used for differential interferometric applications for change detection. Due to its sensitivity to the topography, a large constellation may improve the potential of SAR tomographic techniques in terms of vertical resolution and number of acquisitions. As in other radar applications, the gained knowledge in Single-Input-Multiple-Output (SIMO) SAR systems paves the way for Multiple-Input-Multiple-Output (MIMO) systems, which can be combined with different SAR imaging modes such as TOPS/ScanSAR to improve the performance and capabilities.

Appendix A

List of Publications of the Author

A.1 Journal Publications

1. Sakar, N., Rodriguez-Cassola M., Prats-Iraola P., A. Reigber and Moreira A. (2018). "Analysis of Geometrical Approximations in Signal Reconstruction Methods for Multistatic SAR Constellations with Large Along-Track Baseline". In: *IEEE Geoscience and Remote Sensing Letters* 15.6, pp. 892–896.

2. Sakar, N., Rodriguez-Cassola M., Prats-Iraola P. and Moreira A. (2020). "Azimuth Reconstruction Algorithm for Multistatic SAR Formations with Large Along-Track Baselines". In: *IEEE Transactions on Geoscience and Remote Sensing*, vol. 58, no. 3, pp. 1931 - 1940.

3. Sakar, N., Rodriguez-Cassola M., Prats-Iraola P. and Moreira A. (2022). "Sampling Analysis and Processing Approach for Distributed SAR Constellations with Along-track Baselines". In: *IEEE Transactions on Geoscience and Remote Sensing*, vol. 60, pp. 1-12, 2022.

A.2 Conference Publications

1. Sakar, N., Rodriguez-Cassola M., Prats-Iraola P., A. Reigber and Moreira A. (2017). "Analysis of Geometrical Approximations in Signal Reconstruction Methods for Multistatic Large Along-track Baseline SAR Constellations". In: *European Radar Conference (EURAD)*. Nürnberg, Germany, pp. 5–8.

2. Sakar, N. and M. Rodriguez-Cassola (2018). "Generalized Range Doppler Reconstruction Algorithm for Multistatic Along-track SAR Constellations". In: *Proceedings of European Conference on Synthetic Aperture Radar (EUSAR)*. Aachen, Germany, pp. 1–5.

3. Sakar, N., Rodriguez-Cassola M., Prats-Iraola P., A. Reigber and Moreira A. (2018). "Investigations on the Reconstruction of Multistatic Large Along-Track SAR Constellations for HRWS Imaging". In: *IEEE International Geoscience and Remote Sensing Symposium (IGARSS)*. Valencia, Spain, pp. 3659–3662.

4. Sakar, N., Rodriguez-Cassola M., Prats-Iraola P. and Moreira A. (2019). "Doppler Based Azimuth Reconstruction Algorithm for Multistatic SAR Formations in High Resolution Wide Swath Mode". In: *IEEE International Geoscience and Remote Sensing Symposium (IGARSS)*. Yokohama, Japan, pp. 1124–1127.

5. Sakar N., Rodriguez-Cassola M., Prats-Iraola P. and Moreira A. (2020). "Polychromatic Time Domain Reconstruction Approach for Along-track Multistatic

SAR Constellations with Varying PRI". In: *IEEE Radar Conference*, Florence, Italy, 2020, pp. 1-6.

Bibliography

Aguttes, J. P. (2003). "The SAR Train Concept: Required Antenna Area Distributed over *N* Smaller Satellites, Increase of Performance by *N*". In: *IEEE Geoscience and Remote Sensing Symposium (IGARSS)*. Vol. 1. Toulouse, France, pp. 542–544.

Aguttes, N. P. (2005). "The SAR Train Concept: An Along-track Formation of SAR Satellites for Diluting the Antenna Area over *N* Smaller Satellites, While Increasing Performance by *N*". In: *Acta Astronautica* 57.2-8, pp. 197–204. ISSN: 2151-1535. DOI: 10.1109/JSTARS.2016.2630048.

Almeida, F. Queiroz de et al. (2018). "Multichannel Staggered SAR Azimuth Processing". In: *IEEE Transactions on Geoscience and Remote Sensing*, pp. 1–17. ISSN: 0196-2892. DOI: 10.1109/TGRS.2017.2783444.

ASI Cosmo-Skymed from 11 July 2020 [Online] (n.d.). URL: https://www.asi.it/en/earth-science/cosmo-skymed/.

Balanis, C. (1997). *Antenna Theory: Analysis and Design*. New York: John Wiley Sons Inc.

Bamler, R., F. Meyer, and W. Liebhart (2006). "No Math: Bistatic SAR Processing Using Numerically Computed Transfer Functions". In: *IEEE International Geoscience and Remote Sensing Symposium (IGARSS)*. Denver, Colorado, USA, pp. 1844–1847. DOI: 10.1109/IGARSS.2006.476.

— (2007). "Processing of Bistatic SAR Data From Quasi-Stationary Configurations". In: *IEEE Transactions on Geoscience and Remote Sensing* 45.11, pp. 3350–3358.

Bauck, J. L. and W. K. Jenkins (1989). "Convolution-backprojection Image Reconstruction for Bistatic Synthetic Aperture Radar". In: *IEEE International Symposium on Circuits and Systems*. Portland, USA, pp. 631–634.

Brown, J. (1981). "Multi-channel Sampling of Low-pass Signals". In: *IEEE Transactions on Circuits and Systems* 28.2, pp. 101–106. ISSN: 0098-4094. DOI: 10.1109/TCS.1981.1084954.

Brown, W. M. (1967). "Synthetic Aperture Radar". In: *IEEE Transactions on Aerospace and Electronic Systems* AES-3.2, pp. 217–229.

Callaghan, G. D. and I. D. Longstaff (1999). "Wide-swath Space-borne SAR Using a Quad-element Array". In: *IEE Proceedings - Radar, Sonar and Navigation* 146.3, pp. 159–165. ISSN: 1350-2395. DOI: 10.1049/ip-rsn:19990126.

Cantalloube, H. et al. (2004). "Challenges in SAR Processing for Airborne Bistatic Acquisitions". In: *Proceedings of European Conference on Synthetic Aperture Radar (EUSAR)*. Ulm, Germany, pp. 577–580.

Capella Space from 11 July 2020 [Online] (n.d.). URL: https://www.capellaspace.com/.

Carrara, W. G., R. S. Goodman, and R. M. Majewski (1995). *Spotlight Synthetic Aperture Radar: Signal Processing Algorithms*. Norwood, Massachusetts: Artech House.

Cerutti-Maori, D. et al. (2014a). "MIMO SAR Processing for Multichannel High-Resolution Wide-Swath Radars". In: *IEEE Transactions on Geoscience and Remote Sensing* 52.8, pp. 5034–5055.

Cerutti-Maori, D. et al. (2014b). "Signal Reconstruction with Range Migration Correction for High-Resolution Wide-Swath SAR Systems". In: *Proceedings of European Conference on Synthetic Aperture Radar (EUSAR)*. Berlin, Germany, pp. 1–4.

Cheng, P. et al. (2017). "An Improved Azimuth Reconstruction Method for Multichannel SAR Using Vandermonde Matrix". In: *IEEE Geoscience and Remote Sensing Letters* 14.1, pp. 67–71. ISSN: 1558-0571. DOI: 10.1109/LGRS.2016.2626309.

Cumming, I. G. and F. H. Wong (2005). *Digital Processing of Synthetic Aperture Radar Data: Algorithms and Implementation*. Boston, London: Artech House.

Curlander, J. C. and R. N. McDonough (1991). *Synthetic Aperture Radar: Systems and Signal Processing*. New York, USA: Wiley.

Currie, A. and M. A. Brown (1992). "Wide-swath SAR". In: *IEEE Proceedings F - Radar and Signal Processing* 139.2, pp. 122–135.

Cutrona, L. J. et al. (1961). "A High-Resolution Radar Combat Surveillance System". In: *IRE Transactions on Military Electronics* MIL-5.2, pp. 127–131.

D'Aria, D., A. M. Guarnieri, and F. Rocca (2004). "Focusing Bistatic Synthetic Aperture Radar Using Dip Move Out". In: *IEEE Transactions on Geoscience and Remote Sensing* 42.7, pp. 1362–1376. DOI: 10.1109/TGRS.2004.830166.

De Zan, F. and A. Monti Guarnieri (2006). "TOPSAR: Terrain Observation by Progressive Scans". In: *IEEE Transactions on Geoscience and Remote Sensing* 44.9, pp. 2352–2360. DOI: 10.1109/TGRS.2006.873853.

DLR Portal, TanDEM-X - (August, 2020)" Italy – Automatic speed control of moving objects using the Doppler effect " [Online] (n.d.). URL: https://www.dlr.de/content/en/images/2011/1/italy-automatic-speed-control-of-moving-objects-using-the-doppler-effect_334.jpg?__blob=normal&v=11__ifc1920w.

DLR Portal, TanDEM-X - (August, 2020) "Las Vegas, USA – First TerraSAR-X Digital Elevation Model" [Online] (n.d.). URL: https://www.dlr.de/content/en/images/2011/1/italy-automatic-speed-control-of-moving-objects-using-the-doppler-effect_334.jpg?__blob=normal&v=11__ifc1920w.

DLR Portal, TanDEM-X - (August, 2020) "Oil slick in the Gulf of Mexico" [Online] (n.d.). URL: https://www.dlr.de/content/en/images/2011/3/oil-slick-in-the-gulf-of-mexico_2523.jpg?__blob=normal&v=11__ifc1920w.

DLR Portal, TanDEM-X - (August, 2020)"The port of Sendai after the tsunami" [Online] (n.d.). URL: https://www.dlr.de/content/en/images/2011/2/the-port-of-sendai-after-the-tsunami_1539.jpg?__blob=normal&v=11__ifc1920w.

D'Amico, S. et al. (2013). "Non-Cooperative Rendezvous using Angles-only Optical Navigation: System Design and Flight Results". In: *Journal of Guidance, Control and Dynamics (JGCD)* 36.6, pp. 1573–1595.

Elachi, C. (1988). *Spaceborne Radar Remote Sensing: Applications and Techniques*. New York: IEEE press.

ESA Earth Observation Portal, (August, 2020) "Almaz-1 Mission" [Online] (n.d.). URL: https://directory.eoportal.org/web/eoportal/satellite-missions/a/almaz..

ESA Earth Observation Portal, (August, 2020) "European Remote Sensing Satellite" [Online] (n.d.). URL: https://earth.esa.int/web/guest/missions/esa-operational-eo-missions/ers..

Ferretti, A., C. Prati, and F. Rocca (2001). "Permanent Scatterers in SAR Interferometry". In: *IEEE Transactions on Geoscience and Remote Sensing* 39.1, pp. 8–20.

Fischer, C. et al. (2006). "A High Resolution Wide Swath SAR". In: *Proceedings of European Conference on Synthetic Aperture Radar (EUSAR)*. Dresden, Germany.

Fornaro, G. and F. Serafino (2006). "Imaging of Single and Double Scatterers in Urban Areas via SAR Tomography". In: *IEEE Transactions on Geoscience and Remote Sensing* 44.12, pp. 3497–3505. ISSN: 0196-2892.

Freeman, A. et al. (2009). "SweepSAR: Beam-forming on Receive Using a Reflector-phased Array Feed Combination for Spaceborne SAR". In: *IEEE Radar Conference*. Pasadena, USA, pp. 1–9.

Freeman, A. et al. (2019). "The Legacy of the SIR-C/X-SAR Radar System: 25Years on". In: *Remote Sensing of Environment* 231, p. 111255. DOI: https://doi.org/10.1016/j.rse.2019.111255.

Gebert, N., G. Krieger, and A. Moreira (2005a). "High Resolution Wide Swath SAR Imaging – System Performance and Influence of Perturbations". In: *Proceedings of International Radar Symposium (IRS)*. Berlin, Germany.

Gebert, N., G. Krieger, and A. Moreira (2005b). "SAR Signal Reconstruction from Non-uniform Displaced Phase Centre Sampling in the Presence of Perturbations". In: *IEEE International Geoscience and Remote Sensing Symposium (IGARSS)*. Vol. 2. Seoul, Korea, pp. 1034–1037.

— (2006). "Digital Beamforming for HRWS-SAR Imaging: System Design, Performance and Optimization Strategies". In: *IEEE International Geoscience and Remote Sensing Symposium (IGARSS)*. Denver, Colorado, USA, pp. 1836–1839.

Gebert, N., G. Krieger, and A. Moreira (2006). "High Resolution Wide Swath SAR Imaging with Digital Beamforming – Performance Analysis, Optimization and System Design". In: *Proceedings of European Conference on Synthetic Aperture Radar (EUSAR)*. Dresden, Germany, pp. 563–566.

Gebert, N., G. Krieger, and A. Moreira (2009). "Digital Beamforming on Receive: Techniques and Optimization Strategies for High-Resolution Wide-Swath SAR Imaging". In: *IEEE Transactions on Aerospace and Electronic Systems* 45.2, pp. 564–592. ISSN: 0018-9251.

Gebert, Nicolas (2009). "Multi-Channel Azimuth Processing for High-Resolution Wide-Swath SAR Imaging". Doctoral dissertation. Institute of Radio Frequency Engineering and Electronics (IHE), Karlsruhe Institute of Technology (KIT).

Gini, F., F. Lombardini, and M. Montanari (2002). "Layover Solution in Multibaseline SAR Interferometry". In: *IEEE Transactions on Aerospace and Electronic Systems* 38.4, pp. 1344–1356. ISSN: 0018-9251.

Goodman, N., D. Rajakrishna, and J. Stiles (1999). "Wide Swath High Resolution SAR Using Multiple Receive Apertures". In: *IEEE International Geoscience and Remote Sensing Symposium (IGARSS)*. Vol. 3. Hamburg, Germany, pp. 1767–1769. DOI: 10.1109/IGARSS.1999.772089.

Goodman, N. A. et al. (2002). "Processing of Multiple-Receiver Spaceborne Arrays for Wide-Area SAR". In: *IEEE Transactions on Geoscience and Remote Sensing* 40.4, pp. 841–852. ISSN: 1558-0644. DOI: 10.1109/TGRS.2002.1006362.

Grafmüller, B. and C. Schaefer (2005). "Hochauflösende Synthetik-Apertur Radarvorrichtung und Antenne". Pat. DE 10 2005 062 031.0.

Griffiths, H. D. and P. Mancini (1991). "Ambiguity Suppression In SARs Using Adaptive Array Techniques". In: *IEEE International Geoscience and Remote Sensing Symposium (IGARSS)*. Vol. 2. Espoo, Finland, pp. 1015–1018. DOI: 10.1109/IGARSS.1991.580292.

Harris, F. J. (1978). "On the Use of Windows for Harmonic Analysis with the Discrete Fourier Transform". In: *Proceedings of the IEEE* 66.1, pp. 51–83.

Heer, C. et al. (2003). "Investigations on a New High Resolution Wide Swath SAR Concept". In: *IEEE International Geoscience and Remote Sensing Symposium (IGARSS)*. Vol. 1. Toulouse, France, pp. 521–523.

Hülsmeyer, C. (1905). "Verfahren, um entfernte metallische Gegenstände mittels elektrischer Wellen einem Beobachter zu melden". Pat. DE 165546.

Iceye from 11 July 2020 [Online] (n.d.). URL: https://www.iceye.com/.

JAXA, (August, 2020), "Japanese Earth Resources Satellite "FUYO-1" (JERS-1)" [Online] (n.d.). URL: http://global.jaxa.jp/projects/sat/jers1/index.html..

Kare, J.T. (2001). "Moving Receive Beam Method And Apparatus For Synthetic Aperture Radar". Pat. U.S. 6,175,326 B1.

Kraus, T. et al. (2019). "Addressing the Terrain Topography in Distributed SAR Imaging." In: *IET International Conference on Radar Systems*. Toulon, France.

Krieger, G., N. Gebert, and A. Moreira (2004a). "Digital Beamforming and Non-Uniform Displaced Phase Centre Sampling in Bi- and Multistatic SAR". In: *Proceedings of European Conference on Synthetic Aperture Radar (EUSAR)*. Ulm, Germany, pp. 563–566. ISBN: 3-8007-2828-1.

— (2004b). "Unambiguous SAR Signal Reconstruction from Nonuniform Displaced Phase Center Sampling". In: *IEEE Geoscience and Remote Sensing Letters* 1.4, pp. 260–264. ISSN: 1545-598X.

Krieger, G. and A. Moreira (2003). "Potential of Digital Beamforming in Bi- and Multistatic SAR". In: *IEEE International Geoscience and Remote Sensing Symposium (IGARSS)*. Vol. 1. Toulouse, France, pp. 527–529.

Krieger, G. et al. (2003). "System Concepts for Bi- and Multistatic SAR Missions". In: *International Radar Symposium (IRS)*. Vol. 3. Dresden, Germany, pp. 331–339.

Krieger, G. et al. (2007). "TanDEM-X: A Satellite Formation for High-Resolution SAR Interferometry". In: *IEEE Transactions on Geoscience and Remote Sensing* 45.11, pp. 3317–3341. ISSN: 0196-2892. DOI: 10.1109/TGRS.2007.900693.

Krieger, G. et al. (2014). "Tropospheric and Ionospheric Effects in Spaceborne Single-Pass SAR Interferometry and Radargrammetry". In: *Proceedings of European Conference on Synthetic Aperture Radar (EUSAR)*. Berlin, Germany, pp. 1–4.

Krieger, G. et al. (2018). "MirrorSAR: A Fractionated Space Transponder Concept for the Implementation of Low-Cost Multistatic SAR Missions". In: *Proceedings of European Conference on Synthetic Aperture Radar (EUSAR)*. Aachen, Germany, pp. 1–6.

Larsson, E. G., P. Stoica, and Jian Li (2002). "Amplitude Spectrum Estimation for Two-dimensional Gapped Data". In: *IEEE Transactions on Signal Processing* 50.6, pp. 1343–1354. ISSN: 1053-587X. DOI: 10.1109/TSP.2002.1003059.

Li, Zhenfang et al. (2005). "Generation of Wide-swath and High-resolution SAR Images from Multichannel Small Spaceborne SAR Systems". In: *IEEE Geoscience and Remote Sensing Letters* 2.1, pp. 82–86. ISSN: 1545-598X. DOI: 10.1109/LGRS.2004.840610.

Liu, B. and Y. He (2016). "Improved DBF Algorithm for Multichannel High-Resolution Wide-Swath SAR". In: *IEEE Transactions on Geoscience and Remote Sensing* 54.2, pp. 1209–1225. ISSN: 1558-0644. DOI: 10.1109/TGRS.2015.2476496.

Liu, N. et al. (2017). "Modified Multichannel Reconstruction Method of SAR With Highly Nonuniform Spatial Sampling". In: *IEEE Journal of Selected Topics in Applied Earth Observations and Remote Sensing* 10.2, pp. 617–627. ISSN: 2151-1535. DOI: 10.1109/JSTARS.2016.2630048.

Lopez-Dekker, P. et al. (2008). "Phase Synchronization and Doppler Centroid Estimation in Fixed Receiver Bistatic SAR Systems". In: *IEEE Transactions on Geoscience and Remote Sensing* 46.11, pp. 3459–3471. DOI: 10.1109/TGRS.2008.923322.

Massonnet, D. and J. C. Souyris (2008). *Imaging with Synthetic Aperture Radar*. Lausanne, Switzerland: EFPL Press.

Maxwell, J. C. (1865). "A Dynamical Theory of the Electromagneetic Field". In: *Phlosophical Transactions of the Royal Society of London* 155, pp. 459–512.

Moore, R. K., J. P. Claassen, and Y. h. Lin (1981). "Scanning Spaceborne Synthetic Aperture Radar with Integrated Radiometer". In: *IEEE Transactions on Aerospace and Electronic Systems* AES-17.3, pp. 410–421. DOI: 10.1109/TAES.1981.309069.

Moreira, A., J. Mittermayer, and R. Scheiber (1996). "Extended Chirp Scaling Algorithm for Air- and Spaceborne SAR Data Processing in Atripmap and ScanSAR Imaging Modes". In: *IEEE Transactions on Geoscience and Remote Sensing* 34.5, pp. 1123–1136.

Moreira, A. et al. (2013). "A Tutorial on Synthetic Aperture Radar". In: *IEEE Geoscience and Remote Sensing Magazine* 1.1, pp. 6–43. DOI: 10.1109/MGRS.2013.2248301.

NASA Jet Propulsion Laboratory (August, 2020), "Seasat" [Online] (n.d.). URL: https://www2.jpl.nasa.gov/srtm/index.html.

NASA Jet Propulsion Laboratory (August, 2020) "Shuttle Imaging Radar-A" [Online] (n.d.). URL: https://www.jpl.nasa.gov/missions/shuttle-imaging-radar-a-sir-a/..

NASA Jet Propulsion Laboratory (August, 2020) "Shuttle Imaging Radar-B" [Online] (n.d.). URL: https://www.jpl.nasa.gov/missions/shuttle-imaging-radar-b-sir-b/..

NASA Jet Propulsion Laboratory, (August, 2020) "Shuttle Radar Topography Mission" [Online] (n.d.). URL: https://www2.jpl.nasa.gov/srtm/index.html..

Neo, Yew Lam, Frank Wong, and Ian G. Cumming (2007). "A Two-Dimensional Spectrum for Bistatic SAR Processing Using Series Reversion". In: *IEEE Geoscience and Remote Sensing Letters* 4.1, pp. 93–96.

Papathanassiou, K. P. and S. R. Cloude (2001). "Single-baseline Polarimetric SAR Interferometry". In: *IEEE Transactions on Geoscience and Remote Sensing* 39.11, pp. 2352–2363.

Papoulis, A. (1965). *Probability, Random Variables, and Stochastic Processes*. International student. Tokyo, Japan: McGraw-Hill Kogakusha, Ltd.

— (1977). "Generalized Sampling Expansion". In: *IEEE Transactions on Circuits and Systems* 24.11, pp. 652–654. ISSN: 0098-4094. DOI: 10.1109/TCS.1977.1084284.

Pinheiro, M. et al. (2015b). "Reconstruction of Coherent Pairs of Synthetic Aperture Radar Data Acquired in Interrupted Mode". In: *IEEE Transactions on Geoscience and Remote Sensing* 52.10, pp. 6095–6109. ISSN: 0196-2892.

Pinheiro, M. et al. (2015a). "Reconstruction of Coherent Pairs of Synthetic Aperture Radar Data Acquired in Interrupted Mode". In: *IEEE Transactions on Geoscience and Remote Sensing* 53.4, pp. 1876–1893. ISSN: 0196-2892.

Prati, C. and F. Rocca (1992). "Range Resolution Enhancement with Multiple SAR Surveys Combination". In: *IEEE Geoscience and Remote Sensing Symposium (IGARSS)*. Vol. 2. Seattle, WA, USA, pp. 1576–1578.

Prats, P. et al. (2011). "Distributed Imaging with TerraSAR-X and TanDEM-X". In: *IEEE International Geoscience and Remote Sensing Symposium (IGARSS)*. Vancouver, Canada, pp. 3963–3966.

Prats-Iraola, P. et al. (2014). "On the Processing of Very High Resolution Spaceborne SAR Data". In: *IEEE Transactions on Geoscience and Remote Sensing* 52.10, pp. 6003–6016.

Reigber, A. and A. Moreira (2000). "First Demonstration of Airborne SAR Tomography Using Multibaseline L-band Data". In: *IEEE Transactions on Geoscience and Remote Sensing* 38.5, pp. 2142–2152.

Rodriguez-Cassola, M. et al. (2011). "Efficient Time-Domain Image Formation with Precise Topography Accommodation for General Bistatic SAR Configurations". In: *IEEE Transactions on Aerospace and Electronic Systems* 47.4, pp. 2949–2966. ISSN: 0018-9251.

Rodriguez-Cassola, M. et al. (2013). "Cross-platform spaceborne SAR Imaging: Demonstration Using TanDEM-X". In: *IEEE International Geoscience and Remote Sensing Symposium (IGARSS)*. Melbourne, Australia, pp. 1844–1847. DOI: 10.1109/IGARSS.2006.476.

Rodriguez-Cassola, M. et al. (2014). "Geometrical Considerations of Spaceborne SAR Surveys". In: *Proceedings of European Conference on Synthetic Aperture Radar (EUSAR)*. Berlin, Germany, pp. 1–4.

Rodriguez-Cassola, M. et al. (2015a). "Doppler-Related Distortions in TOPS SAR Images". In: *IEEE Transactions on Geoscience and Remote Sensing* 53.1, pp. 25–35. ISSN: 0196-2892. DOI: 10.1109/TGRS.2014.2313068.

Rodriguez-Cassola, M. et al. (2015b). "Verfahren zur Rechnergestuetzen Verarbeitung von SAR-Daten". Pat. E.U. 102013213304.

Rodriguez-Cassola, Marc (2012). "Bistatic Synthetic Aperture Radar Processing". Doctoral dissertation. Institute of Radio Frequency Engineering and Electronics (IHE), Karlsruhe Institute of Technology (KIT).

Rosen, P. A. et al. (2000). "Synthetic Aperture Radar Interferometry". In: *Proceedings of the IEEE* 88.3, pp. 333–382.

Sakar, N. and M. Rodriguez-Cassola (2018). "Generalized Range Doppler Reconstruction Algorithm for Multistatic Along-track SAR Constellations". In: *Proceedings of European Conference on Synthetic Aperture Radar (EUSAR)*. Aachen, Germany, pp. 1–5.

Sakar, N. et al. (2018). "Analysis of Geometrical Approximations in Signal Reconstruction Methods for Multistatic SAR Constellations With Large Along-Track Baseline". In: *IEEE Geoscience and Remote Sensing Letters* 15.6, pp. 892–896.

Sakar, N. et al. (2019). "Doppler Based Azimuth Reconstruction Algorithm for Multistatic SAR Formations in High Resolution Wide Swath Mode". In: *IEEE International Geoscience and Remote Sensing Symposium (IGARSS)*. Yokohama, Japan, pp. 1124–1127.

— (2020a). "Azimuth Reconstruction Algorithm for Multistatic SAR Formations With Large Along-Track Baselines". In: *IEEE Transactions on Geoscience and Remote Sensing*, pp. 1931 –1940. ISSN: 1558-0644. DOI: 10.1109/TGRS.2019.2950963.

— (2020b). "Polychromatic Time Domain Reconstruction Approach for Along-track Multistatic SAR Constellations with Varying PRI". In: *European Radar Conference*. Florence, Italy, pp. 1–6.

Salzman, J. et al. (2002). "Interrupted Synthetic Aperture Radar (SAR)". In: *IEEE Aerospace and Electronic Systems Magazine* 17.5, pp. 33–39. ISSN: 0885-8985. DOI: 10.1109/62.1001990.

Seasat data 1978 (NASA). Processed by ASF DAAC 2013. Retrieved from ASF DAAC 11 July 2020.[Online] (n.d.). URL: https://asf.alaska.edu/data-sets/sar-data-sets/seasat/seasat-images-then-and-now/.

Sherwin, C. W., J. P. Ruina, and R. D. Rawcliffe (1962). "Some Early Developments in Synthetic Aperture Radar Systems". In: *IRE Transactions on Military Electronics* MIL-6.2, pp. 111–115.

Sikaneta, I., C. H. Gierull, and D. Cerutti-Maori (2014). "Optimum Signal Processing for Multichannel SAR: With Application to High-Resolution Wide-Swath Imaging". In: *IEEE Transactions on Geoscience and Remote Sensing* 52.10, pp. 6095–6109. ISSN: 0196-2892. DOI: 10.1109/TGRS.2013.2294940.

Skolnik, M. I. (1980). *Introduction to Radar Systems*. Singapore: McGraw-Hill.

Stiles, J., N. Goodman, and SiChung Lin (2000). "Performance and Processing of SAR Satellite Clusters". In: *IEEE International Geoscience and Remote Sensing Symposium (IGARSS)*. Vol. 2. Honolulu, HI, USA, pp. 883–885.

Stolt, R. (1978). "Migration by Fourier Transform Techniques". In: *Geophysics* 43.1, pp. 49–76.

Suess, M., B. Grafmueller, and R. Zahn (2001). "A Novel High Resolution, Wide Swath SAR System". In: *IEEE International Geoscience and Remote Sensing Symposium (IGARSS)*. Vol. 3. Sydney, NSW, Australia, pp. 1013–1015.

Suess, M. and W. Wiesbeck (2002a). "Side-looking Synthetic Aperture Radar System". Pat. E.U. 1 241 487.

— (2002b). "Side-Looking Synthetic Aperture Radar System". Pat. EP 1 24148.

Tello-Alonso, M., P. Lopez-Dekker, and J. J. Mallorqui (2010). "A Novel Strategy for Radar Imaging Based on Compressive Sensing". In: *IEEE Transactions on Geoscience and Remote Sensing* 48.12, pp. 4285–4295. ISSN: 0196-2892.

Ulander, L., H. Hellsten, and G. Stenström (2003). "Synthetic Aperture Radar Processing Using Fast Factorized Back-projection". In: *IEEE Transactions on Aerospace and Electronic Systems* 39.3, pp. 760–776.

Umbra Lab from 11 July 2020 [Online] (n.d.). URL: https://umbra.space/.

Villano, M., G. Krieger, and A. Moreira (2014). "Staggered SAR: High-Resolution Wide-Swath Imaging by Continuous PRI Variation". In: *IEEE Transactions on Geoscience and Remote Sensing* 52.7, pp. 4462–4479. ISSN: 0196-2892. DOI: 10.1109/TGRS.2013.2282192.

Wiesbeck, W. (2001). "SDRS: Software-defined Radar Sensors". In: *IEEE International Geoscience and Remote Sensing Symposium (IGARSS)*. Vol. 7. Sydney, NSW, Australia, pp. 3259–3261.

Wiley, C.A. (1965). *Pulsed Doppler Radar Methods and Apparatus*.

— (1985). "Synthetic Aperture Radars". In: *IEEE Transactions on Aerospace and Electronic Systems* 21.3, pp. 440–443.

Wong, F. H., Ngee Leng Tan, and Tat Soon Yeo (2000). "Effective Velocity Estimation for Space-borne SAR". In: *IEEE International Geoscience and Remote Sensing Symposium (IGARSS)*. Vol. 1. Honolulu, HI, USA, pp. 90–92.

Yegulalp, A. F. (1999). "Fast Backprojection Algorithm for Synthetic Aperture Radar". In: *Proc. IEEE Radar Conference*. Waltham, USA, pp. 60–65.

Younis, M., C. Fischer, and W. Wiesbeck (2003). "Digital Beamforming in SAR Systems". In: *IEEE Transactions on Geoscience and Remote Sensing* 41.7, pp. 1735–1739.

Younis, M., Y. Venot, and W. Wiesbeck (2003). "A Simulator for Digital Beam Forming SAR". In: *International Radar Symposium (IRS)*. Vol. 3. Dresden, Germany.

Younis, Marwan (2004). "Digital Beam-Forming for High Resolution Wide Swath Real and Synthetic Aperture Radar". Doctoral dissertation. Institute of Radio Frequency Engineering and Electronics (IHE), Karlsruhe Institute of Technology (KIT).

Zhu, X. X. and R. Bamler (2010). "Very High Resolution Spaceborne SAR Tomography in Urban Environment". In: *IEEE Transactions on Geoscience and Remote Sensing* 48.12, pp. 4296–4308. ISSN: 0196-2892. DOI: 10.1109/TGRS.2010.2050487.